UNIVERSITÀ DELLA CALABRIA

UNIVERSITÀ DELLA CALABRIA

Department DIATIC

Philosophical Doctorate in

Scienze ed Ingegneria dell'Ambiente delle Costruzioni e dell'Energia

CYCLE

XXIX

Improving General Relativity tests with innovative Lunar and Martian retroreflector payloads

Settore Scientifico Disciplinare FIS/01

Coordinator: Ch.mo Prof. Pietro Pantano

Signature:

Supervisor/Tutor: Dr. Simone Dell'Agnello

Signature:

PhD Candidate: Dr. Emanuele Ciocci

Signature:

Academic Year 2016/2017

Tranquillo Giordà,

non ti sei perso niente...

... sta ancora a pagina 11

Contents

List of Acronyms

AM0 Air Mass 0

APOLLO Apache Point Observatory Lunar Laser ranging Operation

ASI Agenzia Spaziale Italiana

CCD Charge Coupled Device

CCR Corner Cube Retroreflector

CERGA Centre d'Etudes et de Recherche en Géodynamique et Astronomie

CfA Center for Astrophysics

cFP compact Field Point

DAO Dihedral Angle Offset

EDM Entry descent and landing Demonstrator Module

ESA European Space Agency

ETRUSCO Extra Terrestrial Ranging to Unified Satellite COnstellations

FFDP Far Field Diffraction Pattern

FPGA Field Programmable Gate Array

GLONASS GLObal'naya Navigationnay Sputnikovaya Sistema

GNSS Global Navigation Satellite System

GPS Global Positioning System

GR General Relativity

ILN International Lunar Network

ILRS International Laser Ranging Service

INFN Istituto Nazionale di Fisica Nucleare

INRRI INstrument for landing-Roving laser ranging/altimetry Retroreflector Investigations

IR Infra-Red

ITRF International Terrestrial Reference Frame

LabVIEW Laboratory Virtual Instrumentation Engineering Workbench

LAGEOS LAser GEOdynamics Satellite

LEO Low Earth Orbit

LLR Lunar Laser Ranging

LLRRA21 Lunar Laser RetroReflector for the 21st Century

LN2 Liquid Nitrogen

LNF Laboratori Nazionali di Frascati

LRA Laser Retroreflector Array

MLI Multi-Layer Insulation

MLRO Matera Laser Ranging Observatory

MLRS McDonald Laser Ranging Station

MoonLIGHT Moon Laser Instrumentation for General relativity High accuracy Tests

MRO Mars Reconnaissance Orbiter

NI National Instrument

OCA Observatoire de Côte d'Azur

OCS Optical Cross Section

PEP Planetary Ephemeris Program

PFM Proto Flight Model

PPN Parametrized Post Newtonian

SCF Satellite/lunar/GNSS laser ranging/altimetry and Cube/microsat Characterization Facility

SCF-G Satellite/lunar/GNSS laser ranging/altimetry and Cube/microsat Characterization Facilities - Galileo optimized

SCF_Lab Satellite/lunar/GNSS laser ranging/altimetry and Cube/microsat Characterization Facilities Laboratory

SEP Strong Equivalence Principle

SERMS Study of Radiation Effects on Materials for Space Applications

SLR Satellite Laser Ranging

SS Solar Simulator

SW Software

TVT Thermo-Vacuum Test

VA Velocity Aberration

VI Virtual Instrument

VLBI Very Long Baseline Interferometry

Preface

Why this work at INFN-LNF

Lunar Laser Ranging (LLR) is a technique used since the 1969 to realize high-precision distance measurements between a laser ground station on Earth and a Corner Cube Retroreflector (CCR) on the lunar surface. Starting from CCRs deployment on lunar surface, LLR has benefited from several improvements in observing technology and data modeling. Nowadays these improvements provide an accuracy of postfit residuals to few centimeters.

Nowadays LLR is a primary tool used to study the dynamics of the Earth-Moon system and, most of all, the gravitational physics, geodesy, and studies of the lunar interior([Williams 2009a], [Williams 2009b], [Rambaux 2008], [Williams 2008] and [Nordtvedt 1995]). Regarding gravitational physics, LLR is used to obtain high-accuracy tests of General Relativity (GR) and to test predictions of various alternative theories of gravity in slow motion and weak field regime.
In addition LLR contributes to the realization of both the terrestrial and selenocentric reference frames (the selenocenter is the Moon center of mass) and finally, LLR also investigates the processes related to the Moon's interior dynamics. Finally LLR has also provided important data on the composition and the origin of the Moon by measuring its rotations and tides.Since the lunar CCR first deployment (starting in 1969 with the Apollo 11 mission), LLR to Apollo CCR arrays has supplied several significant tests of GR ([Murphy 2003] and [Nordtvedt 2003]): measured of the Geodetic Precession, probed the weak and strong equivalence principle, determined

the Parametrized Post Newtonian (PPN) parameters, addressed the time change of the gravitational constant ($\frac{\dot{G}}{G}$) and $1/r^2$ deviations in slow motion and weak field regime.

In the framework of this thesis I will show that a new experiment equipped with next-generation retroreflectors on the Moon (or Mars) will provide laser ranging data with a significantly improved accuracy, useful to increase the sensitivity of GR tests and of new gravitational theories beyond GR, like spacetime torsion ([Martini 2016], [Lops 2011] and [March 2013]). Initially in fact, the Apollo arrays contributed to a negligible portion of the LLR error budget but now the ranging accuracy of ground stations has improved by more than two orders of magnitude: for example the new Apache Point Observatory Lunar Laser ranging Operation (APOLLO) station at Apache Point, USA, is capable to make measurements with a level of accuracy to the mm ([Murphy 2012]); also Matera Laser Ranging Observatory (MLRO), at the Agenzia Spaziale Italiana (ASI) Space Geodesy Center of Matera in Italy, has restarted LLR operations after hardware improvement. Hence because of lunar librations, the old arrays dominate the LLR error budget, which is limited to a few cm (for the Apollo retroreflector) as said before.

The University of Maryland, Principal Investigator for the old Apollo arrays, and Istituto Nazionale di Fisica Nucleare (INFN) - Laboratori Nazionali di Frascati (LNF) are proposing an innovative CCR array design, in order to reduce significantly the error contribution of LLR payloads. This is the goal of the Moon Laser Instrumentation for General relativity High accuracy Tests (MoonLIGHT), a science experiment of INFN and of the Satellite/lunar/GNSS laser ranging/altimetry and Cube/microsat Characterization Facilities Laboratory (SCF_Lab), the CCR space test facility at LNF. Among the main challenges for this new array design we have the study of the thermal and the optical effects of the absorption of solar radiation within the CCR. The goal is to reduce the heat transfer from the hot housing and from the rapid temperature changes of the regolith to the CCR; in fact a thermal gradient on the CCR will decrease its optical performances and then the accuracy in the GR tests.

In addition the INFN-LNF, at the SCF_Lab, is working on a new type of retrore-

flector array: INstrument for landing-Roving laser ranging/altimetry Retroreflector Investigations (INRRI) ([Dell'Agnello 2017]). INRRI is a small compact CCR payload (54mm x 20mm with a mass of around 25g) designed for landing/rover on rocky solar system bodies. INRRI is designed to be interrogated by lasers equipped on orbiters around these bodies (not directly from laser stations on Earth). With INRRI will be possible to use new fixed points for laser ranging measurements in order to study with improved accuracy the geocenter of new physics bodies in the solar system, providing useful data for the improvement of gravitational field models as the Apollo arrays had done in the 1969 for the Moon. Finally INRRI, after the successful completion of the space qualification tests, was installed on the European Space Agency (ESA) mission ExoMars-Entry descent and landing Demonstrator Module (EDM)[1] to be deployed on Mars in October 2016. Unfortunately the EDM "Schiaparelli" crashed on Mars surface during the landing. More analysis will be done with Mars Reconnaissance Orbiter (MRO) data in order to check the instruments status (along with INRRI).

What my contribution was

My thesis activities at INFN-LNF (starting in November 2013) can be divided into the following parts:

- setup and management of the experimental tests;

- thermal analysis of the experimental tests;

- physics analysis and GR simulations;

Work in the setup and management of the experimental tests

SCF_Lab is an ISO 7 clean room equipped with different instruments for characterization and modeling the detailed thermal behavior and the optical performance

---

[1]reference to: http://exploration.esa.int/mars/46124-mission-overview/

(using the so called "SCF-Test") of CCRs. Basically the laboratory is equipped with two vacuum chambers and two solar simulators to reproduce the space conditions, two optical tables to reproduce the laser beam coming from the ground station and one Infra-Red (IR) camera to acquire infrared pictures. The key experimental innovation is the concurrent measurement and modeling of the Far Field Diffraction Pattern (FFDP) and the temperature distribution of the retroreflector payload under thermal conditions produced with a close-match solar simulator. These unique capabilities provide experimental validation ([Boni 2011]) of the space segment for Satellite Laser Ranging (SLR) and LLR. In this field my work was to plan the experimental tests, develop all the custom Software (SW) used for SCF_Lab subsystem control, as well as the solar simulator calibration.

Thermal analysis of the experimental data

We can acquire thermal data in two ways, with probes installed on payload key points or with an IR camera. However, a probe on the CCR will be a mayor noise source for the optical analysis. Therefore, one of the key element in the "Satellite/lunar/GNSS laser ranging/altimetry and Cube/microsat Characterization Facility (SCF)-Test" is the thermal measurements of the CCR front face in a non-invasive way with the IR thermo-camera. In this field, my work was to setup, acquire and analyze the IR picture in order to extract the CCR front face temperature and then study its thermal behavior, with a custom MatLAB codes, in realistic space conditions. The thermal behavior is critical point in the CCRs analysis because it drives its ultimate optical performance.

General Relativity sensitivity studies

Regarding the LLR physics measurements and simulation, I realized an offline physics analysis work of LLR data with the Planetary Ephemeris Program (PEP) software. This is a highly specialized analysis package initially developed at the Harvard-Smithsonian Center for Astrophysics (CfA), and part of my PhD thesis work is to run this software. After an initial training period, my work is focused

on estimation of the expected accuracy improvement on various GR tests using MoonLIGHT-2 on the Moon and INRRI on Mars. In this way we can quantify how we can improve the GR tests accuracy using these next-generation laser retroreflector payloads.

This thesis work is divided into 6 Chapters:

Chapter 1 is an introduction to SLR/LLR technology, here I will describe in particular how a laser ground station works and what is a CCR.

Chapter 2 describe the "classical tests" of GR.

Chapter 3 is dedicated to describe the MoonLIGHT-2 and INRRI experiments, showing the main simulations realized to define the retroreflectors properties and payload mechanical structure.

Chapter 4 is dedicated to the SCF_Lab infrastructure and the SW that I realized for the experimental tests setup, control and management.

Chapter 5 is focused on the experimental tests results obtained. In particular this Chapter is composed by the experimental tests of MoonLIGHT-2 (SCF-test) and INRRI (qualification flight tests).

Chapter 6, describe the results obtained with the study of sensitivity in GR tests in slow motion and weak field regime using the PEP software. I will also show the improvements that can be achieved with MoonLIGHT-2 on lunar surface and INRRI array on Mars surface.

Finally I will discuss the conclusions and future prospects of this thesis work.

Chapter 1

The Satellite and Lunar Laser Ranging

SLR and LLR technologies started both in the 1950's as new kind of measurements to study possible changes in the gravitational constant from variation in the orbit of artificial satellites. For these reasons the community scientific started to work on CCR (section 1.1) to be installed on satellites, firing light pulses from the ground to measure the angular motion of the satellite respect to the fixed stars ([Bender 1973] and [Dell'Agnello 2010]). The lasers development, started from late '60s, provided a major improvement in the accuracy achievable with this kind of measurement, along with a new and fundamental tool to improve the lunar and satellites orbits determination (trough CCR position) and most of all the study of lunar librations for the Moon.

Basically the SLR/LLR technique consists in a time-of-flight measurement (figure 1.1) of short laser pulses fired from ground stations of the International Laser Ranging Service (ILRS) towards payloads of CCRs on the Moon/Satellites, and then retroreflected back to the stations. Nowadays laser ranging technique provides precise, metrologically absolute positioning measurements in the Sun-Earth-Moon system with a space segment based on cost-effective, passive, maintenance-free payloads.
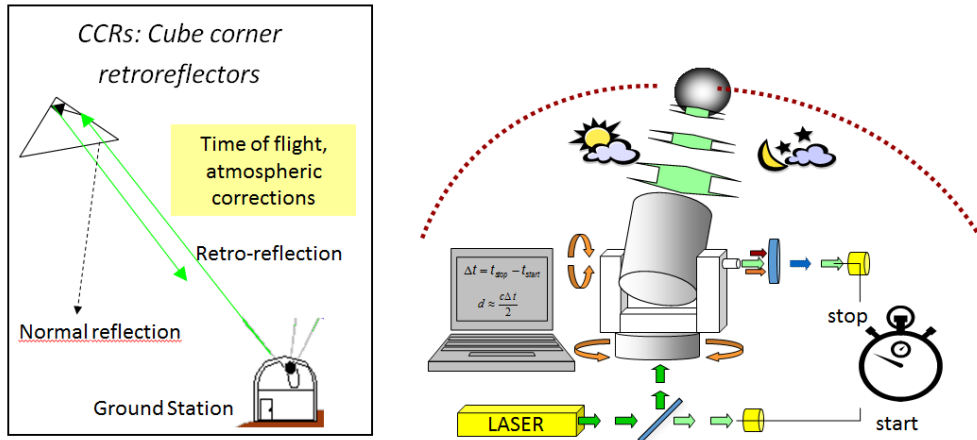
Figure 1.1: CCR time of flight measurement working concept

The ILRS was established in the 1998 and its purpose is to provide SLR/LLR data and related products to support geodetic and geophysical research activities, as well to the maintenance of an accurate International Terrestrial Reference Frame (ITRF). The ILRS also develops the necessary global standards and specifications to encourages international adherence to its conventions. The network stations, available to realize SLR/LLR and part of the ILRS network are listed in figure 1.2. However, only few a of these stations are able to reach the Moon.

The first ranging station, realized is 1970, is McDonald Observatory, Texas (USA). This station was fully dedicated to lunar ranging and was closed in 1985 after routine maintenance activities and remained non-operational for more than 15 years. The transition to the McDonald Laser Ranging Station (MLRS) occurred on two sites: MLRS1 (1983-1988) and MLRS2 (since 1988) which shared lunar and artificial satellite ranging facilities. During the 1980s, two other stations have carried out LLR. The Haleakala Observatory in Maui, (USA), produced high-quality data over a few years around 1990. Since 1982, Centre d'Etudes et de Recherche en Géodynamique et Astronomie (CERGA) station is active at the Observatoire de Côte d'Azur (OCA), (France). All the data used in this thesis work (see Chapter 6) come from the two old generation observatories that are still operating, McDonald and CERGA, plus the new ones APOLLO and ASI-MLRO in Italy, that has
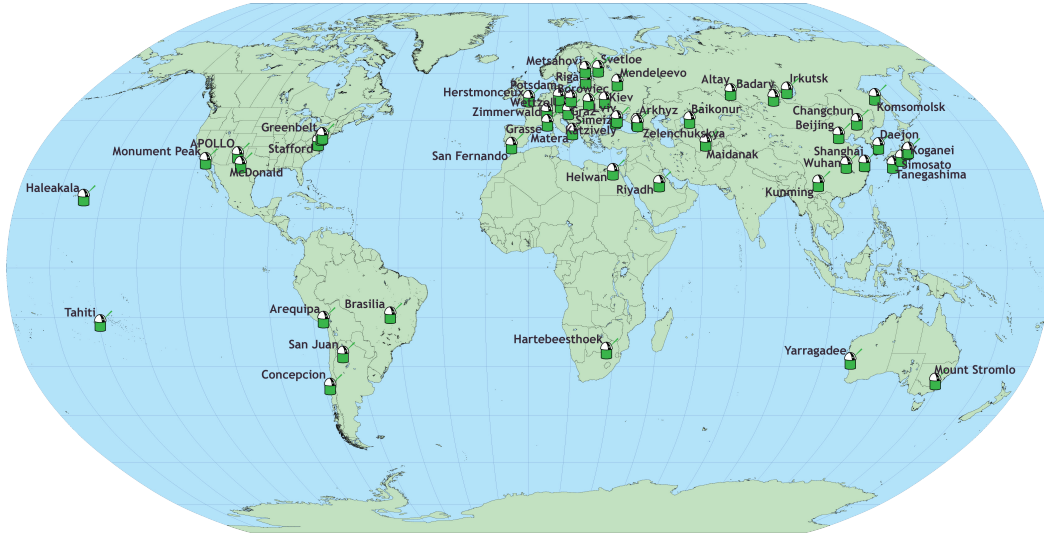
Figure 1.2: ILRS stations network

re-started LLR operations since 2010.

However since the beginning of laser ranging science, the ground station technology has greatly improved, enhancing LLR accuracy (figure 1.3). Historically the accuracy of LLR measurements decreased from more than 30 cm, to roughly 2 cm; this achievement was possible thanks to the improvement on the capability to record photons. In this way and together also with the increase in data analysis technique and statistics collected we can reach the actual accuracy is about some millimeters ([Murphy 2012]). But as shown in figure 1.3, an asymptote has been reached from 1995 to 2005 so it is necessary to accomplish the same improvements on the CCR side.
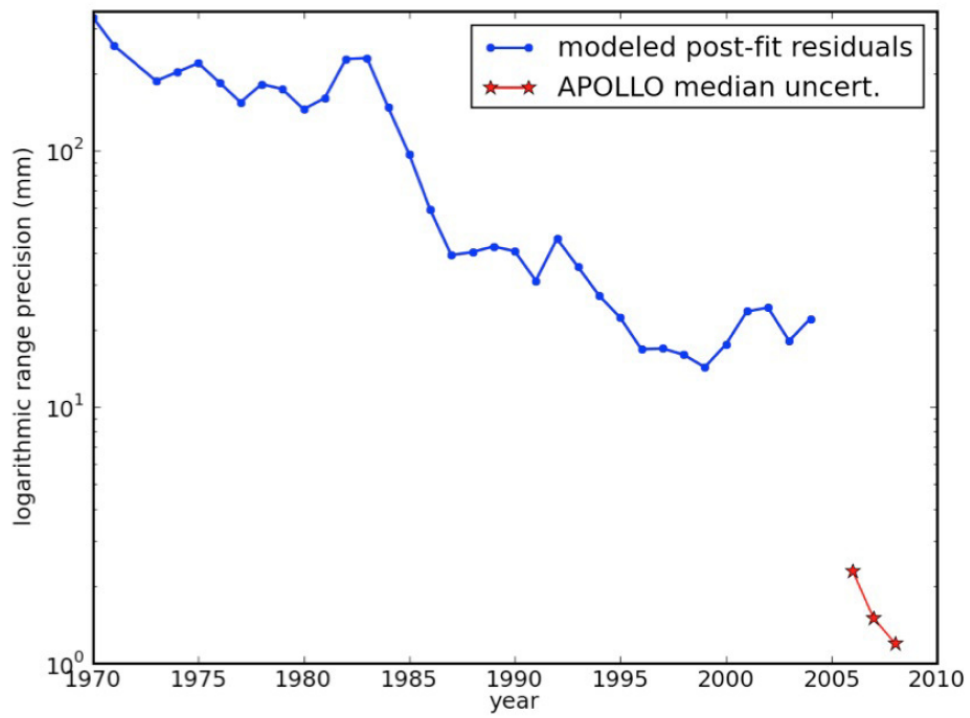
Figure 1.3: LLR accuracy improvements over the years and before the advent of APOLLO

1.1   Corner Cube Retroreflectors

A CCR is a solid cube corner retroreflector, realized cutting a fused silica glass (see figure 1.4). The CCRs are installed inside Laser Retroreflector Array (LRA) that are passive, lightweight and maintenance free. The CCRs have very good performances over decades thanks to proper thermal design and choice of materials like the Apollo ones (figure 1.4).
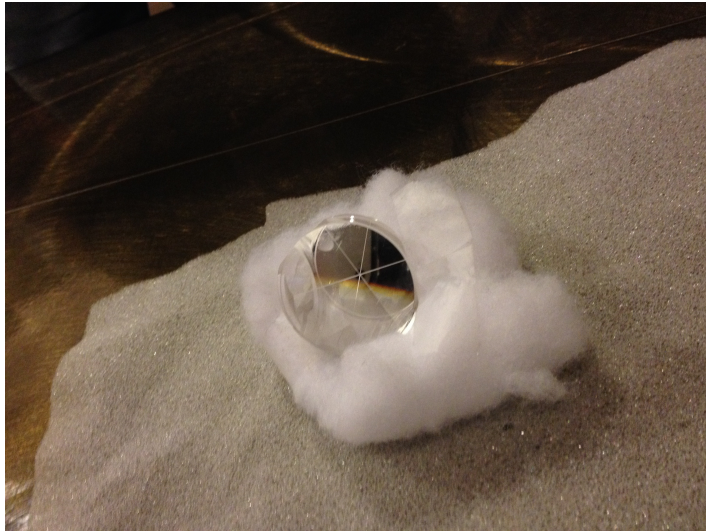

Figure 1.4: Apollo 14 CCR

The working principle of a CCR is very simple, it is a device that retroreflects the light back in the same direction from which it came. It consists of three perpendicular reflective surfaces forming a corner of a cube. There are two main families of CCR, the coated and the uncoated ones.
The uncoated ones performances were demonstrated with the Apollo missions (Apollo 11, 14 and 15 LRA). These three arrays contain hundreds CCRs with a front face diameter of about 38 millimeters installed inside some special cavities (see figure 1.5).

Uncoated cubes like the Apollo ones were also installed in some satellite missions like LAser GEOdynamics Satellite (LAGEOS) 1 and 2. The orbital precision on this
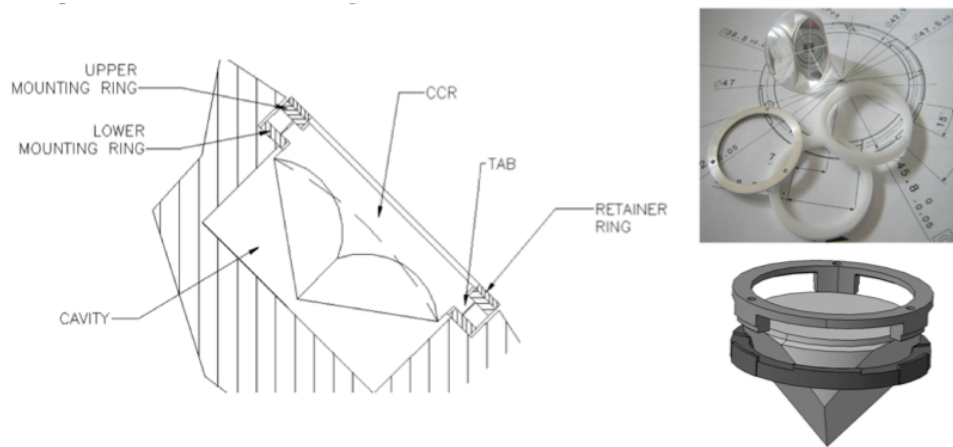
Figure 1.5: Apollo CCR mounting scheme

kind of satellites is about 1 cm. In Chapter 3 I will show the future of lunar CCR with the MoonLIGHT-2 project with the final goal to use a new bigger CCR with a 100 mm front face diameter unaffected by lunar librations (figure 1.6) in order to better estimate the Earth-Moon distance and to test GR with LLR. Starting
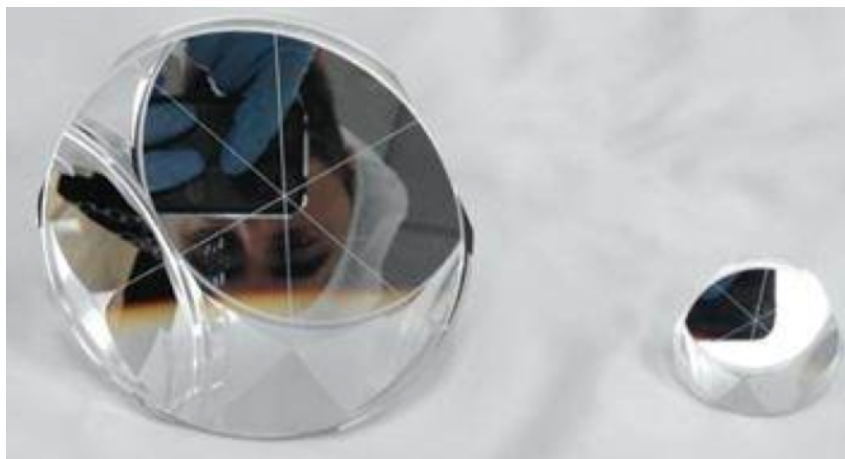

Figure 1.6: Comparison between Apollo and MoonLIGHT CCR

from late 1980s, aluminum coated CCRs with an active diameter of 28 mm were used for the first generation of Global Navigation Satellite System (GNSS) constella-

tions, GLObal'naya Navigationnay Sputnikovaya Sistema (GLONASS) and Global Positioning System (GPS). The mounting system of this kind of CCR was really different from the uncoated one; in particular they were placed inside a special aluminum mounts (see figure 1.7).
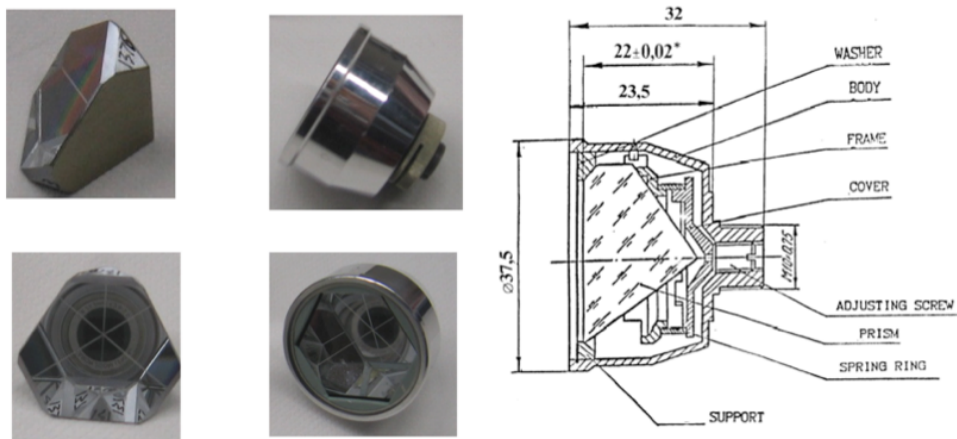

Figure 1.7: GLONASS CCR mounting scheme

Following the test results obtained by the group I work with (SCF_Lab) [1] , new generation of GNSS constellations and satellites started using uncoated CCR. These results show that, generally, the coated CCRs provide better optical performances and also a greater acceptance angle. In fact we have for the coated one an acceptance angle of $36°(left) - 54°(right)$, while for the uncoated is $36°(left) - 17°(right)$. However the coated retroreflectors suffer thermal cycle more than the uncoated ones. So the coated are the best solution when the payload works in conditions of reduced solar illuminations, the uncoated are preferred for other applications that suffers from greater thermal stress condition like the Moon. In Chapter 3 will be also described LRA INRRI designed for Mars, where for the retroreflector we chose the coated ones.

---

[1]SCF_Lab web site: http://www.lnf.infn.it/esperimenti/etrusco/index.html

1.1.1 Apollo & Lunokhod Array

Nowadays there are five different LRA on the lunar surface (see figure 1.8). Three of them were installed within USA missions Apollo 11, 14 and 15 and the other two arrays come from ex-URSS unmanned missions, Luna 17 and Luna 21.

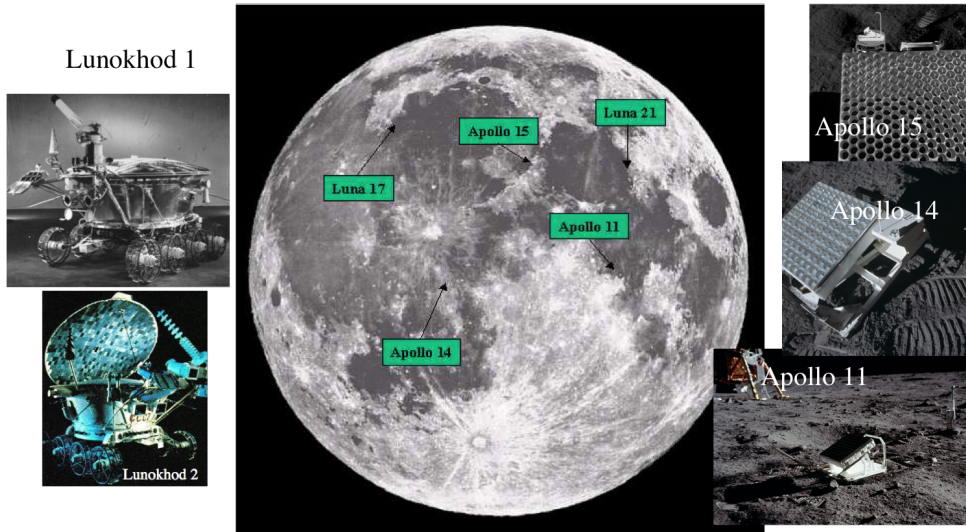Apollo 11 and Apollo 14 have arrays with one hundred of 38 mm front face diameter

Figure 1.8: GLONASS CCR mounting scheme

CCRs in a square pattern of 10×10. The Apollo 15 array is bigger than the other two, but in particular it has an hexagonal shape and has three hundred of 38 mm front face diameter CCRs. Due to its dimension, it is preferentially used for LLR measurements. At the present time $\sim 78\%$ of LLR data comes from measurements to Apollo 15 array.

The two arrays from unmanned missions are installed on two rovers (Lunokhod 1 and Lunokhod 2) equipped with small arrays containing 14 CCRs in triangular configuration.

1.2 SLR/LLR technique

The SLR/LLR technique is basically a time of flight measurement of a laser pulse from one station on Earth to the satellite/Moon and return. The main problem to take into account is the need of a very collimated laser pulse. The first issue to face on is that the turbulence of the atmosphere distorts the laser beam resulting in a divergence of about 1 arcsec. Concerning the Moon, this divergence translates into ∼ 2 kilometers.
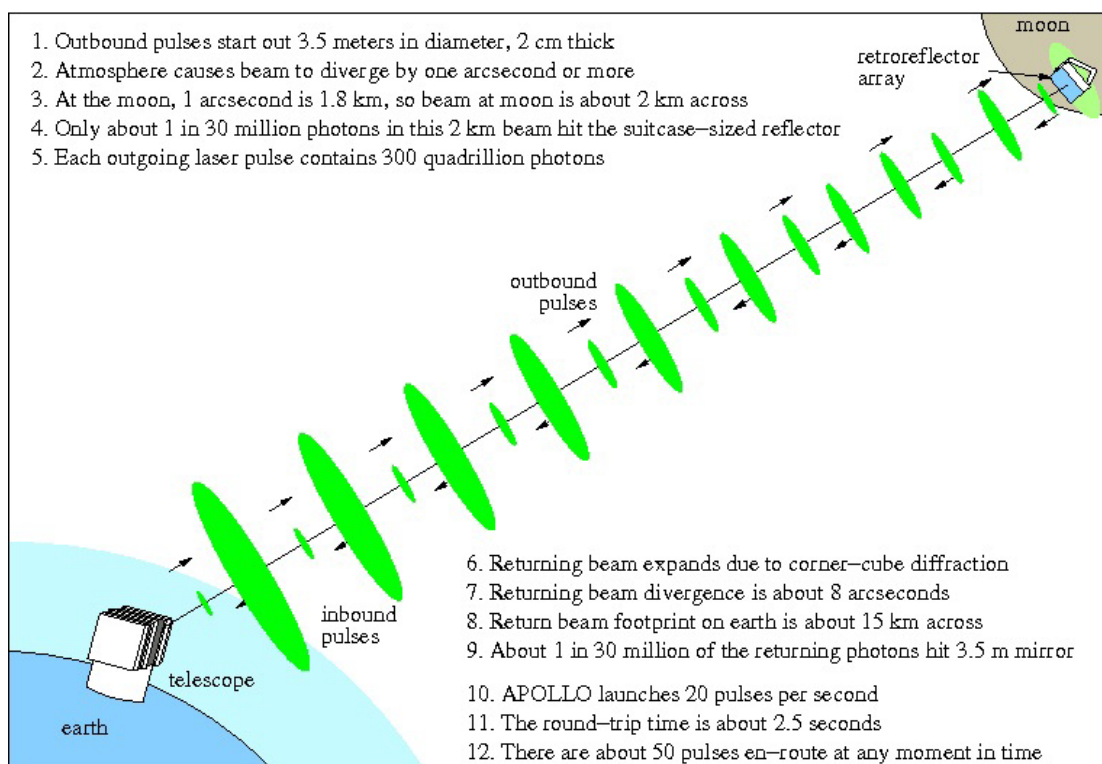

1. Outbound pulses start out 3.5 meters in diameter, 2 cm thick
2. Atmosphere causes beam to diverge by one arcsecond or more
3. At the moon, 1 arcsecond is 1.8 km, so beam at moon is about 2 km across
4. Only about 1 in 30 million photons in this 2 km beam hit the suitcase–sized reflector
5. Each outgoing laser pulse contains 300 quadrillion photons

moon
retroreflector array

outbound pulses

6. Returning beam expands due to corner–cube diffraction
7. Returning beam divergence is about 8 arcseconds
8. Return beam footprint on earth is about 15 km across
9. About 1 in 30 million of the returning photons hit 3.5 m mirror

10. APOLLO launches 20 pulses per second
11. The round–trip time is about 2.5 seconds
12. There are about 50 pulses en–route at any moment in time

inbound pulses

telescope
earth

Figure 1.9: Simple sketch of laser ranging technique[2]

Summarizing, as shown in figure 1.9 [2] , the station sends a laser pulse to the satellite/Moon, due to divergence approximately only one part in 30 million of the

---

[2]reference to: http://www.physics.ucsd.edu/∼tmurphy/apollo/basics.html

light reach the CCRs. The beam is retroreflected and has a divergence itself (for Apollo CCRs the divergence is ~ 8 arcsec). For these reasons, the dimension of the beam that reaches the station is roughly 15 kilometers.

Certainly, in order to achieve millimeter-range measurements, it is necessary to acquire thousands of photons. In fact, LLR stations send approximately 10^{17} photons every pulse; they record 5 photons in return reaching thousands of returns thanks to the very fast pulse of the laser (about 20 pulses per second).

Chapter 2

Historical General Relativity tests

This chapter will describe first the tests of GR originally proposed by Einstein focusing then on the modern tests. After discussing about the reasons for the study of new physics beyond the General Relativity, the last section will be a general description of the PPN formalism, giving particular attention to parameters β, γ and η, that will be further discussed in the Chapter 6 along with the GR test sensitivity studies.

2.1 Classical Einstein General Relativity tests

The Einstein's GR theory was developed between 1907 and 1915 and since then different tests have been conducted in order to validate the theory itself. Since now the theory has passed every test that it has ever been put to. In 1910 however Einstein began to calculate some observable effects of his GR theory, starting from Mercury perihelion precession, and then following with the deflection of light and the gravitational redshift.

In the next session I will briefly describe these observable effects together with the Shapiro Time delay (also known as the 4th test of GR), originally discovered by Shapiro in 1969 using a first version of PEP (the software package used for the GR sensitivity studies in this work).

Mercury's perihelion precession

During the years 1608-1619 Kepler, using only the astronomical observations, developed his three laws of motions. The laws show that the orbit of a planet around the Sun is an ellipse, with the Sun occupies one focus. So using the classical gravitational Newton's theory and assuming the gravitational force of the Sun as the one and only force subjected by the planet, we can obtain Kepler's result.

However this hypothesis was too simple, because also other bodies (planets, asteroids ecc.) exert a gravitational pull on the planet in question, even if at a lower order. Assuming also this contribution to the Kepler equation, it turns out that the attraction of all the other main solar system bodies on the planet induces a perihelion advance. Every planet is subjected to this effect. Mercury was the first one where an anomaly in the orbit was recognized (in 1859 by Urbain Le Verrier) until Einstein calculated the advance of perihelion in 1915.
Studying this anomaly, it was calculated in fact that the perihelion of Mercury moves slightly at the speed of 5600 arcseconds/century, in the same direction in which the planet revolves around the Sun. Removing the contribution of the Earth's precession (5025 arcsec) and of the other bodies, we still miss 43 arcse.
The solution to this problem was provided by Einstein and applied to the final version of his theory of gravity. The GR in fact, reproduces exactly the Mercury orbits recovering also the missing 43 arcsec.

In the following years many other solar system planets perihelion precessions were calculated with high accuracy, addition to that of Mercury, and all the results were in good agreement with GR theory. The expression of the perihelion advance predicted by Einstein is shown in eq.2.1.

$$\Delta \pi R = \frac{3n^3 a^2}{c^2 \left(1 - e^2\right)^2} t \tag{2.1}$$

Where n is the mean motion of the planet, a is the semiaxis, e is the eccentricity, t is the time and c is the speed of light.

Light deflection

Among the historical GR test there is the deflection produced by a massive body (like a star) on a massless particle, otherwise a photon. The deflection effect can be schematized as in figure 2.1 after defying the following parameters:

- r = radial coordinate of the photon in frame centered with the center of the massive body and the periastron is indicated as r_0

- b = distance between the direction of the photon and center of attraction, otherwise called impact parameter.

- δ = angle between the incoming photon direction and the outgoing direction, otherwise called deflection angle.
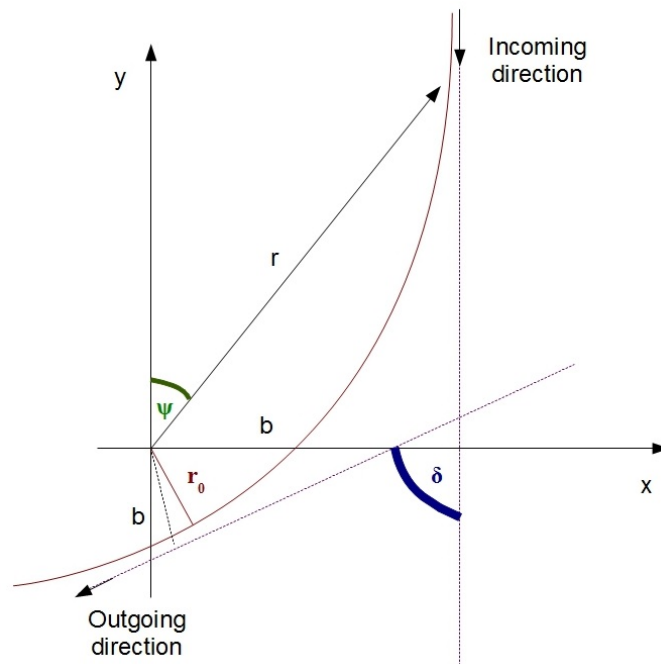
Figure 2.1: Schematic view of the deflection of a photon by a massive body. See text for details

In this way we can describe the light deflection angle by only the parameter δ.

According to GR a photon is deflected by a gravitational field if $E^2 < V_{max}$, knowing that the potential as only one maximum at r = 3m (see figure 2.2) and there $V_{max} = \frac{L^2}{27m^2}$ we obtain the condition:

$$E^2 < \frac{L^2}{27m^2} \tag{2.2}$$

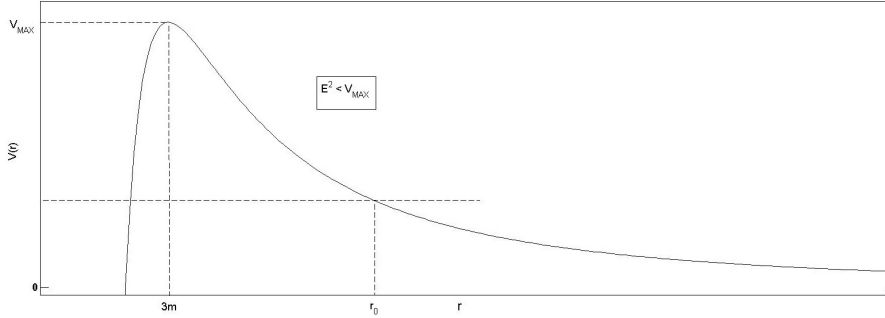Using these data and considering a photon traveling near the Sun we obtain finally

Figure 2.2: Potential behaviour for a massless particle in function of the distance r from the center of a massive body

the deflection of light produced by a mass like the Sun as:

$$\delta \simeq 1.75 arcsec \tag{2.3}$$

The first measurement of the bending of a optical starlight was produced in 1919 by Eddington, Dayson and Davidson during a solar eclipse. This was one of the first and the most significative success of the General Relativity theory (figure 2.3). Eddington, Dayson and Davidson measured the apparent position of a star behind the Sun during the eclipse (in this way the reduced Sun luminosity allowed the star radiation to be visible from the Earth). However the accuracy of the test was only 30% at that time, and increased over the years until reached final value of around 10% during 1980s.

The result predicted by Einstein was in a range of 1.5 and 2 times of the measured value, but a great improvement was provided by the long-baseline and Very Long
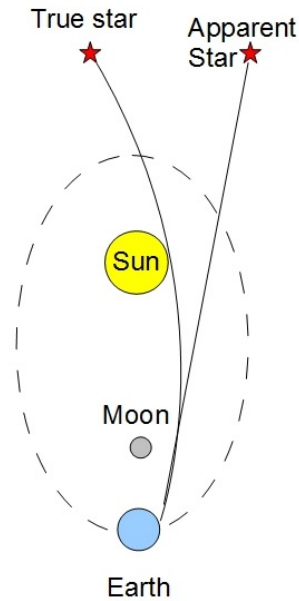
Figure 2.3: Schematic example of Eddington, Dayson and Dividson light deflection test

Baseline Interferometry (VLBI). Using these techniques (that measure the bending of radio waves produced by quasar) the deflection of light accuracy test reached the current value, about 1%.

Shapiro time delay

In 1964, I. Shapiro realized that according to GR, a light signal sent through the solar system should be delayed by the effect of the gravitational field of a massive body like Sun or planets, and the deflections will be proportional to the light bending factor $(\frac{1+\gamma}{2})$ ([Shapiro 1964]). In addition reflecting this signal to Earth is possible to measure this bending factor (usually the time delays are about hundreds of microseconds). Shapiro proposed to use the two Vikings Mars landers as a radar transmitter in order to confirm GR at 0.1% level (in 1976).

In the following years then, other measurements were realized using radar reflection from other probes (like Mariners and Voyager) but actually the best one was

obtained using Doppler tracking to Cassini spacecraft. With this measure today we can confirm GR at a level of 0.002%.

Cosmological constrain on General Relativity

Regardless the results described before, there are still some gravitational theories studying variation from the Einstein GR. The reasons beyond these studies can be summarized in the two following main points.

Firstly the GR presents singularities (space time regions where the curvature tends to infinite) like the super massive black holes at the center of almost all the galaxies discovered (and also the Milky Way). The Big Bang itself, during the Universe first phases, represents a singularity. So in these regions the Einstein equation cannot be used and this poses a serious issue in developing cosmological models and understanding our universe.

Secondly the actual cosmological models assume that our universe is homogeneous and isotropic at great scales. Combining these assumptions with the GR theory it has been possible to develop the actual Big Bang theory, that has predicted many different effects (then discovered by experimental tests) like the cosmic background microwave radiation. However in the last years, the observations of the matter of our universe do not match anymore with the theory. In fact in order to explain the actual structure of our universe with the theory we must assume the presence of a supplemented by much larger amounts of unseen dark matter (and so energy). This matter for now cannot be fully explained by any particle physics standard model. The experimental data show that this dark matter must have a density some five times that of standard-model matter with an energy three times greater still. Even without any direct observation (at this moment) many theories are looking into the dark matter; the study possible variation from the GR can be a great benchmark in order to put some experimental constrain on it and therefore, explain the universe expansion acceleration rate so well measured.

Summarizing, up to now, the GR is incompatible with the "standard model" of particle physics based on quantum field theory. Still there is no agreement if is the

GR that must be modified or the particle physics (or both). In order to allow this unification and solve the previous questions we need other experimental input with improved accuracy, and the LLR can provide useful data in slow motion and weak field regime.

2.2   Parametrized Post-Newtonian formalism

Most of GR tests are expressed using a formalism known as the PPN framework. Eddington described weak spherically symmetric gravitational fields with two different parameters: β describing the nonlinearity in time warping and γ describing space warping. In GR $\beta = \gamma = 1$ and most of the experimental tests effectively place upper limits on $|\beta - 1|$ and/or $|\gamma - 1|$.

The perihelion precession of Mercury is proportional to $\frac{(2+2\gamma-\beta)}{3}$, which is equal to one in GR. Only this test out of the other three classical tests probes the nonlinear nature of Einstein's theory. Initial measurements relied on optical telescopes, modern ones instead are based on radar data and constrain any departure from General Relativity to less than 0.3%. One of the most important sources of uncertainty came from the quadrupole moment of the Sun, but this has now been well constrained from helioseismology. As mentioned above, perihelion precession also affects other solar system bodies, but is far smaller. It has also been observed using radio telescopes in distant binary pulsar systems, where it is known as periastron shift.

Using the PPN formalism, we can approximate quite well most solar-system tests that can be performed nowadays and it is widely used in different GR test. Although the existence of a long-range gravitational fields in addition to the metric in different metric theories of gravity, postulation of those theories requests that matter and non-gravitational fields be completely unaware to them.
The complete PPN formalism takes into account not only β and γ, but ten different parameters as shown in table 2.1.

The expected improvements GR tests using the two new retroreflector payloads

Parameter	What it measures relative to GR	Value in GR	Value in PPN formalism
γ	How much space curvature produced by unit rest mass?	1	γ
β	How much "nonlinearity" in the superposition law for gravity?	1	β
ξ	Preferred-location effects?	0	ξ
α_1		0	α_1
α_2	Preferred-frame effects?	0	α_2
α_3		0	0
α_3	Violation of conservation of total momentum	0	0
ζ_1		0	0
ζ_2		0	0
ζ_3		0	0
ζ_4		0	0

Table 2.1: PPN parameters and their significance.

described in Chapter 6, will be focused on the PPN parameters γ and β. In fact they are the most important and the only nonzero parameters in GR for this thesis work.

Chapter 3

Lunar and Martian payloads: Design and Simulations

The aim of this section is to describe the two payloads objects of my thesis work: MoonLIGHT-2 and INRRI. For each one will be described the design, (showing for MoonLIGHT-2 a short discussion about evolution since the start of the project in 2006), and the structural solution used for CCRs and housing in order to obtain the expected performances.

In section (3.1) will be described the MoonLIGHT-2 payload, with the actual structural design, the same used for the first test campaign in Chapter 5. At the beginning of the section a brief introduction on the the first MoonLIGHT project (named MoonLIGHT-International Lunar Network (ILN), an INFN-LNF project during 2006-2010) will be explained. The general description in section 3.1 will be followed by the description of two subsections.

The first one (section 3.1.1) will describe the thermal simulation carried out by the SCF_Lab team in order to study the expected performances of MoonLIGHT-2 payload (big CCR and structure), and define Big CCR specifics, the key element of MoonLIGHT-2. The second subsection will describe one of the key elements on the structural part of the design, the Sunshade. Here, using a preliminary GR test study, in collaboration with the CfA, I studied the benefits of a design with or

without the Sunshade (subsection 3.1.2).

Section 3.2 will be dedicated to INRRI, a compact and light retroreflector payload used for altimetry and GR tests from rocky solar system bodies. The aim of this section is to describe the INRRI structure and specifics. In the subsection 3.2.1 will be described the scientific goals of the project globally and in relation to my PhD thesis.

In Appendix A and B the optical simulations on the payload under investigation will be reported.

3.1 MoonLIGHT-2

The goal of this section is to show the MoonLIGHT/Lunar Laser RetroReflector for the 21st Century (LLRRA21), starting with its origin in 2006 (as a collaboration between the University of Maryland) and focusing then on the final design used for the test campaign described in Chapter 5. The project MoonLIGHT/LLRRA21 goals were to improve gravity tests and lunar science measurements using a new generation lunar laser retroreflector on the Moon. In fact the actual retroreflectors payload installed on the Moon (Apollo 11-14-15 from USA and Lunokhod 1-2 from ex URSS) have a multi array-structure, and this design produces strong limitations in the payload accuracy due to lunar librations (about 8 degree during the 28 days lunar phase), that result from the eccentricity of the Moon's orbit around the Earth. Due to this phenomenon the old arrays are moved so that one corner of the array is more distant than the opposite corner by several centimeters. This libration tilt on the array shape increases the dimension of the pulse coming back to Earth (figure 3.1), producing a final pulse that will increase its dimension proportionally to the array physical dimensions and to the Moon-Earth distance (in the position in which the libration phenomena are at the peak).

For example the pulse dimensions are about 30 cm ($\pm$ 1 nanoseconds time of flight increase) for the Apollo 15 array, and about 15 cm ($\pm$ 0.5 nanoseconds time flight increase) for the smaller Apollo 11 and Apollo 14 arrays. Currently the lunar libration contributes the largest part of error budget, about 15-50 mm. Using pho-
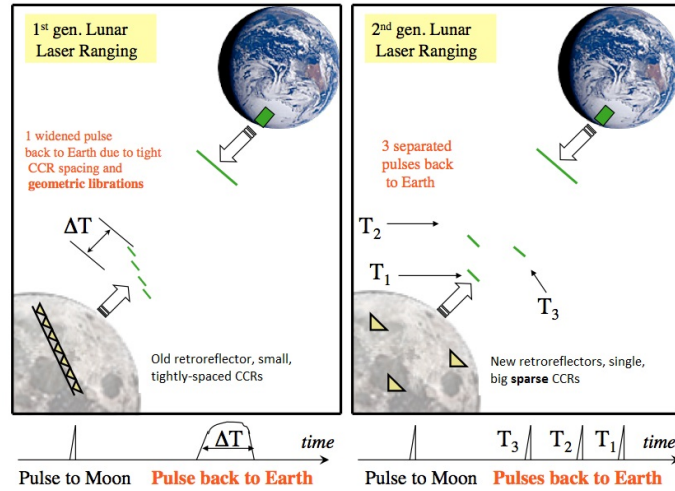
Figure 3.1: Comparison between 1st and 2nd generation Lunar Laser Retroreflectors. The librations tilt the old generation arrays on the left, but the single big CCRs are unaffected, on the right. So we have single short pulses coming back.

ton number, the ground station like APOLLO can reduce the uncertainty of $\sqrt{N}$ ([Murphy 2012]); the Apollo arrays provide a better return (of about one order of magnitude) with respect to Lunokhod ones, but in both cases the accuracy of the ranging measurements cannot go below few centimeters (for a single normal point).

Without hardware upgrades on the space segment (lunar retroreflectors), the only available improvement is on the timing of an extremely large number of single photoelectron returns to reduce the errors by the root mean square of the single photoelectron measurement. Figure 3.3 shows the trend of the accuracy over the years from different ground station leading to the actual situation, where without any new solutions in the space segment it is not possible to achieve major improvement in LLR data accuracy.

To solve the problem, MoonLIGHT-2 (also considered here as the 2nd generation LLR) proposes a new design of lunar CCR whose performance is unaffected by lunar librations, and also by regolith motion, due to its very large thermal cycle. The key idea is to substitute the arrays of multiple small CCRs (3.8 cm of front

face diameter for the Apollo arrays),with a series of single big CCRs in Suprasil 311, each with $100mm$ of front face diameter and an apex length of $72.4mm$, every one deployed separately on the lunar surface (figure 3.1). This arrangement creates single short reflected pulses with a final precision expected to be better than a few millimeters. Once this new kind of retroreflector will be deployed on the Moon, further improvements in the laser ground stations capabilities with shorter laser pulses will be more effective.
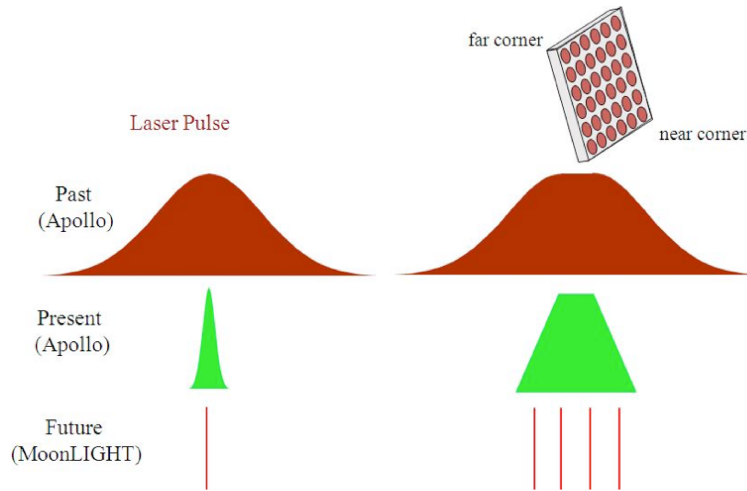
Figure 3.2: The figure shows the measurement uncertainty between laser pulse size fired and retroreflected; how the situation was in the past (on the top); how it is currently (in the middle) and the future possible situation with MoonLIGHT/LLRRA21 CCR (on the bottom).

In table 3.1, second column, we report one of the best GR test carried out by [Williams 2004], while in the third and fourth column the limits in term of test accuracy we want to achieve/surpass with the new MoonLIGHT-2 CCR network, for different accuracies in Moon-Earth ranging.

The CCR optical properties and the thermal relationship with its housing are the core element in the MoonLIGHT-2 project and the key points to gain the expected improvements in LLR described before. The CCR dimension, its material, the

Parameter	Accuracy (cm)	Accuracy (1mm)	Accuracy (0.1mm)
PPN, β	1.1×10^{-4}	10^{-5}	10^{-6}
WEP	1.4×10^{-13}	10^{-14}	10^{-15}
SEP	4.4×10^{-4}	3×10^{-5}	3×10^{-6}
$\dot{G}/G$	9×10^{-13}	5×10^{-4}	5×10^{-15}
$1/r^2$	3×10^{-11}	10^{-12}	10^{-13}
Geodetic Precession	6.5×10^{-3}	6.5×10^{-4}	6.5×10^{-5}

Table 3.1: GR science objectives and measurements. 2nd column shows current situation and measurements from [Williams 2004]. Column 3 and 4 show expectations in the ideal, best-case scenario.

housing structure itself must first of all guarantee the adequate light return from the Moon minimizing thermal effects that could affect its optical intensity level. Then the design with a single CCR will avoid any lunar libration issue increasing test accuracy. Basically the main design requirement is to obtain an optical response with one MoonLIGHT-2 payload at the same level of half of the Apollo 15 array, as it is nowadays. The degradation in signal strength due to lunar dust on CCR front face, referring to [Murphy 2010], now is about at least a factor 10, so we expect that in the first years the MoonLIGHT-2 performances will be 5 times the performances of AP11 and AP14 and around twice of AP15. In fact since the intensity of the return signal is proportional to the fourth power of diameter we can compare the returning signal intensity from MoonLIGHT-2 respect to the Apollo array. On AP15 array we have 300 retroreflector each one with 38mm while on AP11 we have 100 retroreflector. Now calling MoonLIGHT-2 as ML2, we can express these ratio as:

$$\frac{AP15}{ML2} = \frac{300 \cdot 38^4}{100^4} = 6.25 \tag{3.1}$$

$$\frac{AP11}{ML2} = \frac{100 \cdot 38^4}{100^4} = 2.08 \tag{3.2}$$

So we expect to have, from 1 MoonLIGHT-2, around half the performances of AP11 and AP14 (as general reference) and a sixth of AP15.

The subsection 3.1.1 (along with Appendix A) will describe the simulation carried

out by the SCF team in order to define the main thermal characteristics of this CCR, and some of the main performance under thermal stress. The subsection 3.1.2 will describe the details of the structural design of MoonLIGHT-2, in particular with the GR tests sensitivity studies carried out to choose a design without a sunshade. Finally, the subsection 3.1.3 will describe the actual payload design used for the characterization tests.
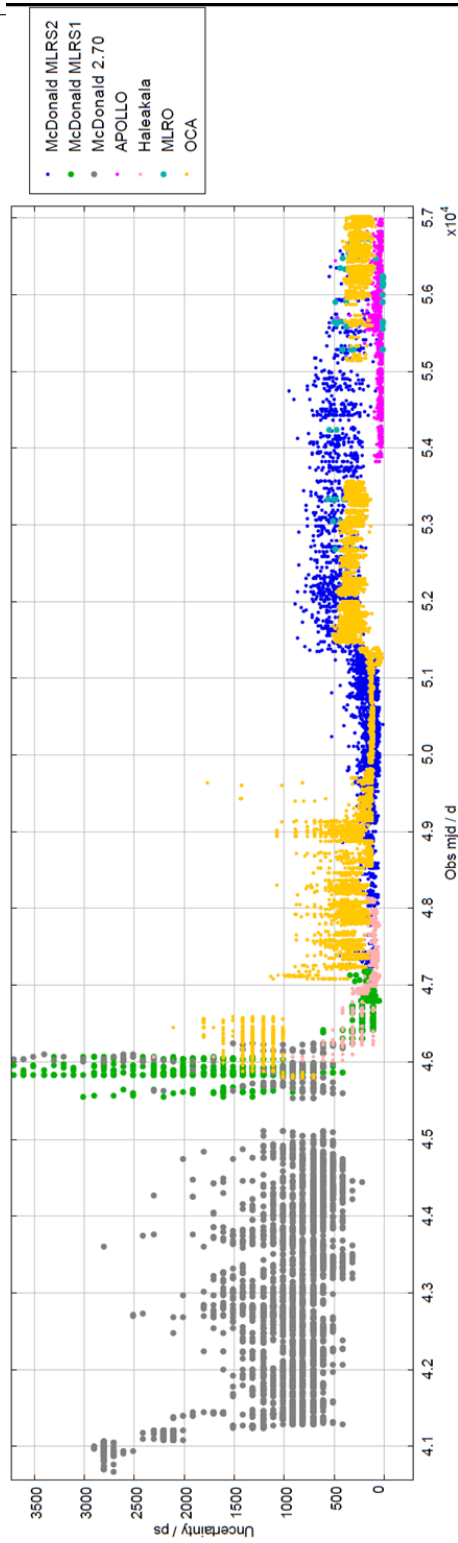
Figure 3.3: Uncertainties of LLR data from 1969 to 2015

3.1.1 Thermal simulations

The goal of this study (conducted by the SCF_Lab team) was to define the expected thermal properties of the MoonLIGHT-2 retroreflector and its housing using the commercial software "Thermal Desktop". These results will be used as reference for the experimental analysis that I carried out and described in sections 5.1.1, 5.1.2 and 5.1.3
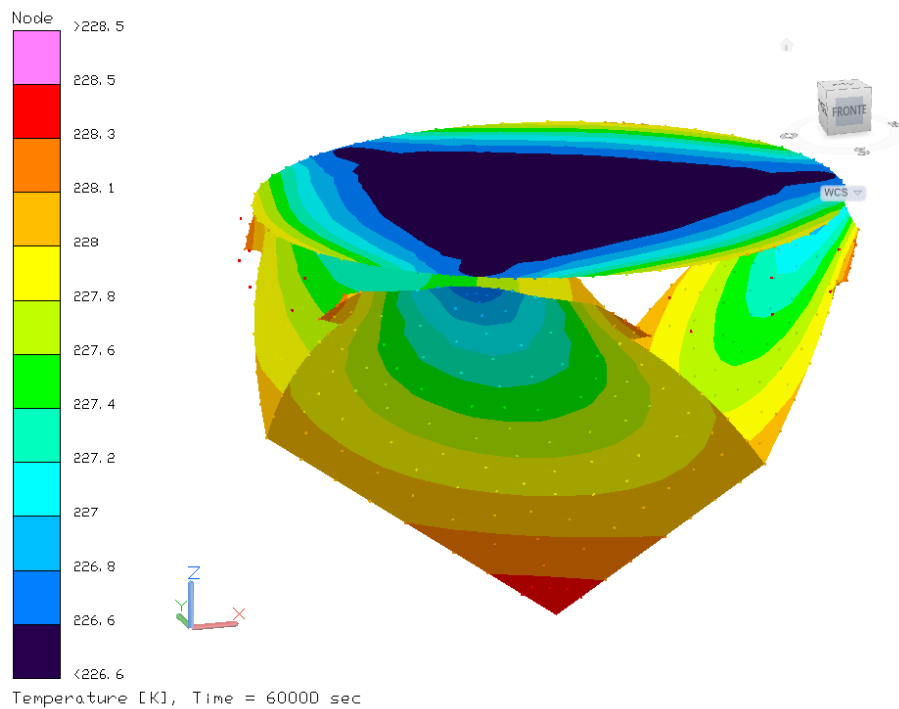
Figure 3.4: Example of a thermal desktop session simulating the retroreflector SUN-OFF phase after 16h

The simulations configuration uses: 2 KEL-F rings, a copper tape on CCR cylindrical surfaces and no can, during a standard SCF-Test at 300K. In particular this is the same experimental setup of the third test campaign in Chapter 5. The simulations reproduce the SCF-Test standard condition during the SUN-ON and SUN-OFF phases (see section 5.1 for test description): in the first one we have the payload

Table 3.2: Materials parameters used for the thermal simulations.

	Solar Absortvitiy	Infrared Emissivity	Conductivity [W/mm/K]	Specific Heat [J/kg/K]
Aluminum	0.44	0.11	0.2	900
Copper tape	0.32	0.02	-	-
Aeroglaze	0.95	0.95	-	-
KEL-F	1	0.93	0.0002022	900
Suprasil	0.1	0.82	0.0014	753
Kapton	0.25	0.34	-	-

Table 3.3: SUN-ON conduction coefficient for simulations

Conductivity	Conduction Coefficient [W/mm^2/K]
Between Cylindrical Al Housing and Al ring	0.15
Between Cylindrical Al Housing and 2 KEL-F rings	10^{-6}
Between 2 KEL-F rings	10^{-5}
Between Low KEL-F ring and CCR tabs	1.6×10^{-5}
Between Up KEL-F ring and CCR tabs	1.6×10^{-5}
Between Up KEL-F ring and Al ring	10^{-5}

inside a structure at 90K facing frontally a radiation of about $1.4 kW/m^2$ on all the retroreflector surface, in the second one we removed the solar radiation so the payload experiences only radiation from the shield at 90K. In table 3.2 are summarized the materials parameters used for the simulations, while in tables 3.3 and 3.4 are summarized respectively the condition coefficients for the SUN-ON and SUN-OFF.

The steady solutions results, compared with the experimental data acquired during the test are summarized in tables 3.5 and 3.6, respectively for the SUN-ON and SUN-OFF.

Looking at the results we can see the good agreement between the simulations and the experimental data. After validating the model with this information, it is possible to use the data to calculate the expected retroreflector thermal constant

Table 3.4: SUN-OFF conduction coefficient for simulations

Conductivity	Conduction Coefficient [W/mm^2/K]
Between Cylindrical Al Housing and Al ring	0.15
Between Cylindrical Al Housing and 2 KEL-F rings	10^{-5}
Between 2 KEL-F rings	10^{-5}
Between Low KEL-F ring and CCR tabs	1.6×10^{-6}
Between Up KEL-F ring and CCR tabs	1.6×10^{-6}
Between Up KEL-F ring and Al ring	10^{-5}

Table 3.5: Thermal simulations steady solutions SUN-ON phase results compared with PT100 data

ID location/name (from simulation)	Temperature from Simulation [K]	Temperature from the Test [K]
Node1 (on one CCR cylindrical face)	253.7	252.7 (PT100)
Node2 (on one CCR cylindrical face)	253.7	252.7 (PT100)
Node3 (on one CCR cylindrical face)	253.7	253 (PT100)
Node4 (on the center of CCR front face)	251.2	251.6 (IR Image)
Node5 (on CCR tip)	257.5	-
Node6 (on Low KEL-F ring, close to a tab)	281.2	281.6 (PT100)
Node6 - Node5 (maximum gradient on front face)	1.4	1.6 (IR Image)

Table 3.6: Thermal simulations steady solutions SUN-OFF phase results compared with PT100 data

ID location/name (from simulation)	Temperature from Simulation [K]	Temperature from the Test [K]
On one CCR cylindrical face	237.6	238.7 (PT100)
Node1 (on one CCR cylindrical face)	237.6	238.9 (PT100)
Node2 (on one CCR cylindrical face)	253.7237.6	239.2 (PT100)
Node3 (on the center of CCR front face)	235.7	241.4 (IR Image)
Node4 (on CCR tip)	241.7	-
Node6 (on Lower KEL-F ring, close to a tab)	265.3	265.5 (PT100)

and thermal gradient on the CCR front face. For the thermal constant refer to figure 3.5, where is it possible to see an expected τ_{CCR} of about 14×10^3 seconds. For the retroreflector front face thermal gradient, the simulations suggest a gradient of about 1.5-2 K. Both results are in agreement with the data analysis shown in Chapter 5.
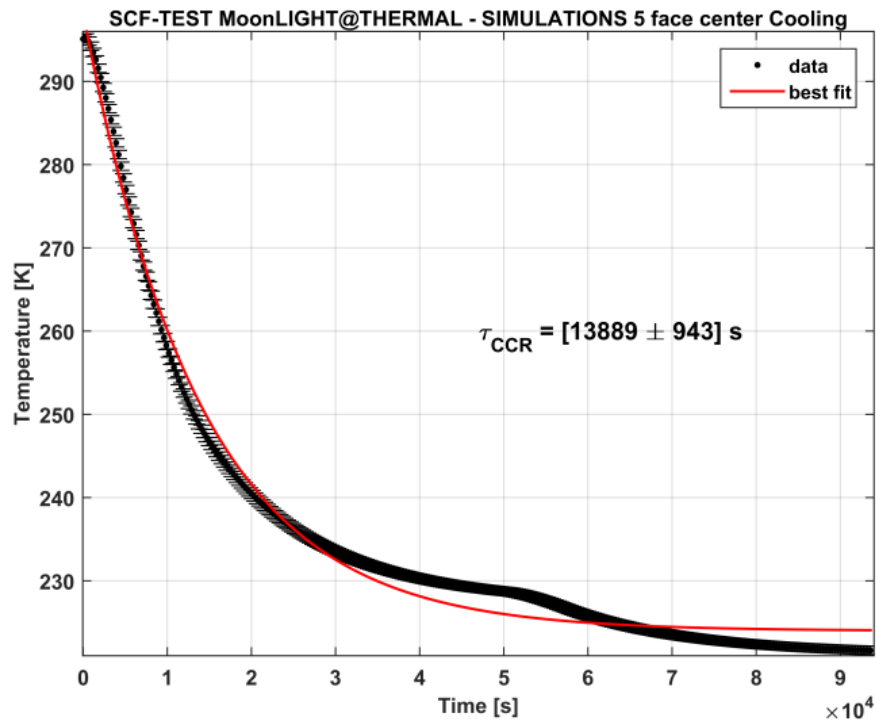
Figure 3.5: MoonLIGHT-2 thermal constant provided by simulation data.

3.1.2 Structural simulation

In the former MoonLIGHT-2 designs, the payload was equipped with a sunshade (visible in yellow in figure 3.6, left side), a cylindrical-like structure designed to shield the CCR front face from the direct solar radiation. Using this shade the payload is available for laser ranging also during daylight, providing more data and statistics. In this way the accuracy in GR tests is increased. However this shade, if from one hand improves GR tests accuracy, on the other hand increases the payload mass of around 1 Kg.

In order to study the differences in the payload accuracy using or removing the sunshade, I carried out a series of GR simulations with PEP in collaboration with the CfA in Boston. With the simulation we want to study the effective improvement in test accuracy with data collected also during the daylight with respect to data collected only at night (from the laser ground station), and compare the GR test expected accuracy using a design with or without the Sunshade. In the following, I will describe the simulation results, however for the details about the GR tests and the simulations with PEP refer to Chapter 6.

The simulation uses dummy data from the three Apollo and three MoonLIGHT-2 CCR for four different ground stations: APOLLO, CERGA, MLRS and MLRO. For the MoonLIGHT-2 location I chose 65°N 40°W; 50°S 35°E; 45°N 27.2°E (the expected landing site of different lunar missions). The dummy data goes from 2013 to 2030 with a time span of 2 years. The simulation is repeated for the two types of MoonLIGHT-2 designs, with and without sunshade.

In order to simulate the case with a sunshade, we assume that the MoonLIGHT-2 reflectors were shielded from the Sun and always available if conditions of the observation site were reached. In the case without sunshade, the MoonLIGHT-2 reflectors were unavailable during the daylight, reducing the amount of collectable data.

In both cases we toke data from the retroreflector only if the Moon's elevation 30° or more, while for the simulation without the sunshade we add the condition that the Sun must be at maximum 10° above the horizon.
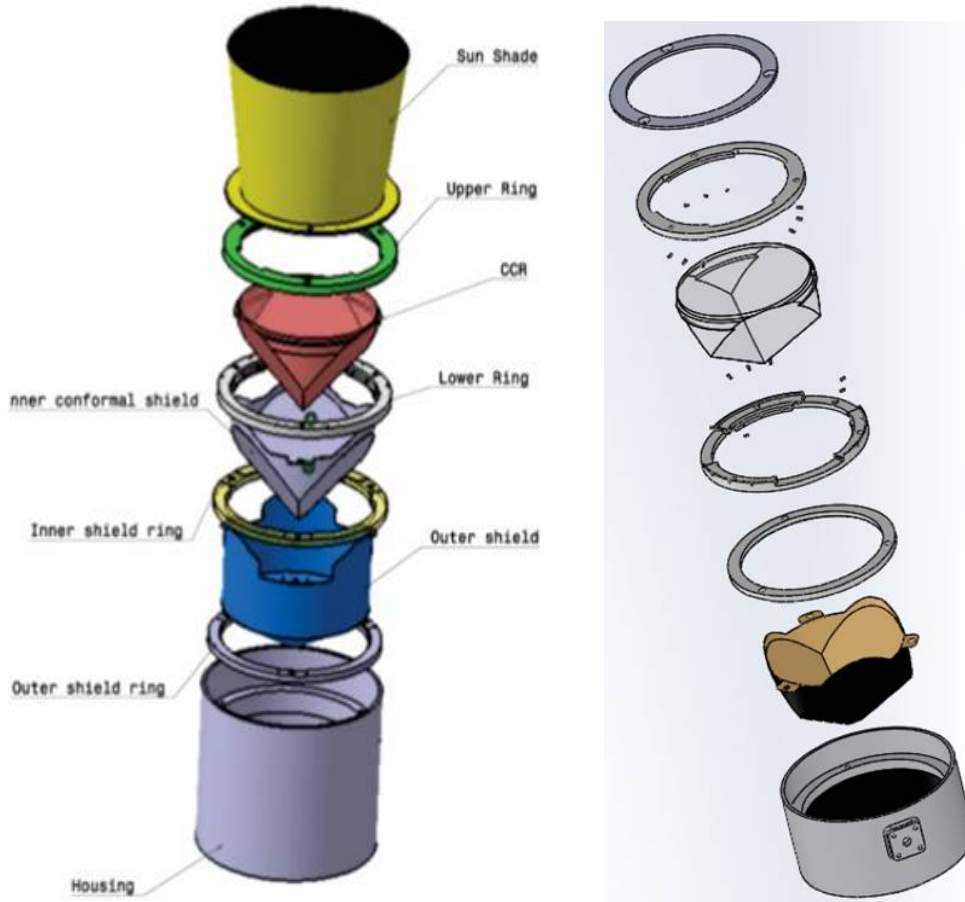
Figure 3.6: on the left: first MoonLIGHT-2 design with a sunshade. **on the right:** former MoonLIGHT-2 design without the sunshade (further optimized with the experimental tests.)

The GR tests carried out are: h (percentage variation of the geodetic precession from GR value), β and $\frac{\dot{G}}{G}$. In the following bullets I report the GR test accuracy for the cases with and without Sunshade and the differences between the two cases:

- h = from 2013 to 2030 there is an improvement of 84.4% with the Sunshade, and 81.5% without it. The relative variation between the two cases is: 2.9%.

- β = from 2013 to 2030 there is an improvement of 83.8% with the Sunshade, and 81.2% without it. The relative variation between the two cases is: 2.7%.

- $\frac{\dot{G}}{G}$ = from 2013 to 2030 there is an improvement of 93.8% with the Sunshade, and 93.1% without it. The relative variation between the two cases is: 0.6%.

As expected the GR tests with the sunshade show a slightly better accuracy compared to the case without the sunshade, obviously thanks to the longer data acquisition (therefore more normal points) available for the design with sunshade during the daylight. However also the data without the Sunshade benefit of a significant improvement with respect to the GR starting value either way and comparing the two cases the differences are minimal. In other words we assume that this small improvement for the sunshade design with respect to the one without the sunshade (around 3%) does not significantly affect the GR results over such a long time analysis.

Accepting this minor decrease in the instrument performance and removing the sunshade, we could greatly optimize the MoonLIGHT-2 weight for its deployment, saving 1kg form the payload mass. So we chose to remove the sunshade from the MoonLIGHT-2 designs as shown in figure 3.6 right side. Finally in the sensitivity studies in Chapter 6 we will consider the payload available only during night time.

3.1.3 Final Design for SCF-Test

At the present time the last optimization of the MoonLIGHT-2 mounting system is shown in figure 3.7. This is the configuration used for the first test described in Chapter 5. Using the second design we can adjust the zenith elevation of about ±30° and mount the CCR with its physical edge vertical or horizontal.
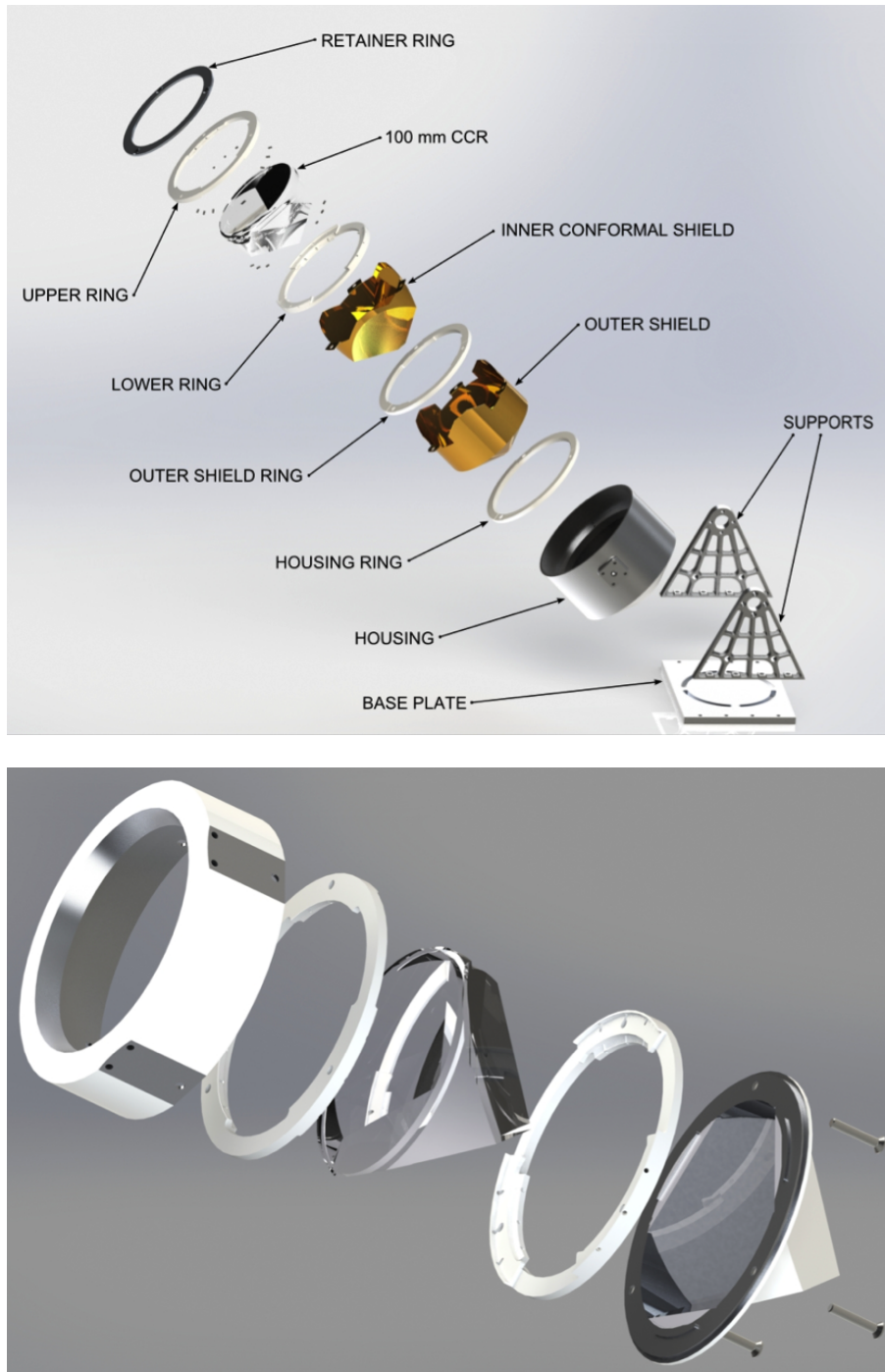
Figure 3.7: Top: Full bracket assembly exploded view of the old mounting system. **Bottom:** Exploded view full assembly of the back-mounting conformal housing of the new mounting system

3.2 INRRI

INRRI was totally designed and manufactured at the SCF_Lab starting from summer 2015 until October 2015, to be integrated on ExoMars EDM ([Dell'Agnello 2017]). However the first conceptual and preliminary studies were made in 2010 while the CCR design, procurement and optical acceptance were made in 2014. Design choices inherited from previous work, and aimed at integrating a functional array of retrore-flectors, with the lowest possible volume and mass. The assembly of the INRRI array consists of eight silver back-coated CCRs with a diameter of 12.7 mm (figure 3.8) glued to the aluminum alloy frame through the use of a space qualified silicon rubber. Every CCR is rotated with one physical edge pointing towards the central axis of the payload. The aluminium alloy frame is coated with Alodine 1200 anticorrosion treatment.

The overall weight is around 25g, with dimensions around 7 cm diameter for 3 cm height (see figure 3.9).

INRRI was qualified and then installed on ExoMars EDM, and was supposed to be the first retroreflector array on Mars surface but unfortunately the mission failed the soft landing. Right now we have no information about the current status of the payload. However INRRI is already accepted for the integration on NASA mission "Mars 2020" and InSight Lander 2018, and it is also proposed for other Martian missions.

3.2.1 Scientific goals

With INRRI installed on a lander/rover and an orbiter equipped with a laser around the solar system body it is possible to use the lander/rover like a long life spot for laser ranging measurements.

Using INRRI like experiments on Mars (or other rocky solar system bodies) surface it will be possible to obtain the following general measurement:

- Center of mass: obtain data for GR test.
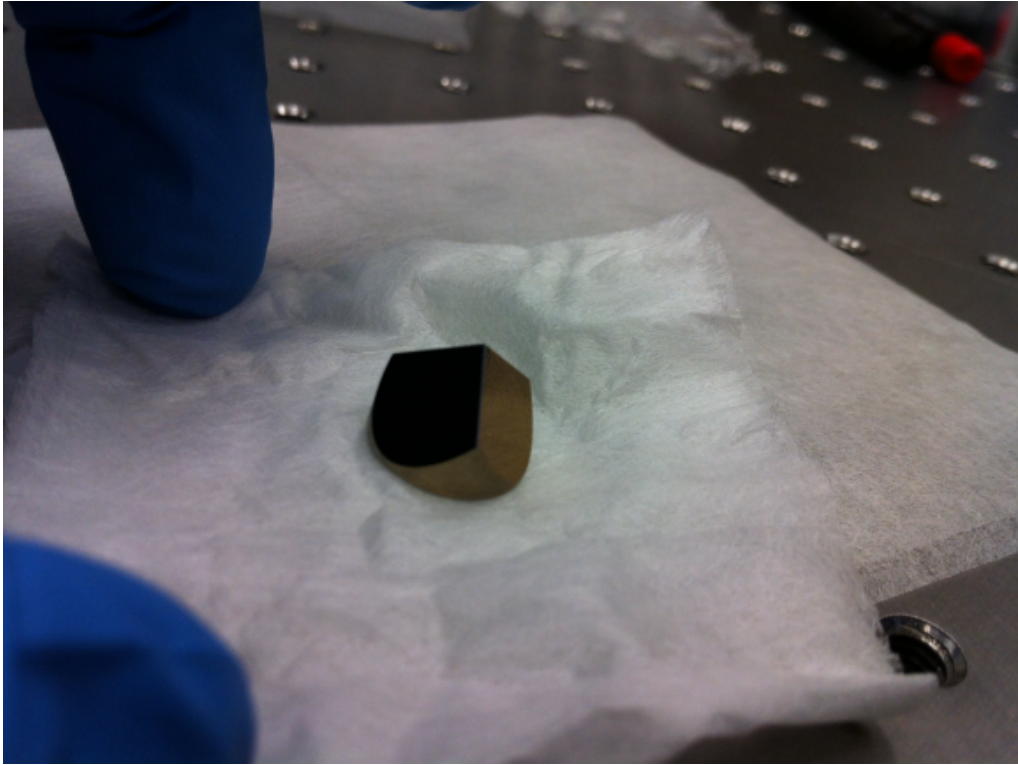
Figure 3.8: one of the 8 INRRI corner cube retroreflector.

- Laser Altimetry: obtain detail about the body surface and study possible deformation on the surface produced by tidal effect.

- Lidar atmospheric observations: study the atmosphere around the landing site.

- Laser communication: Realize a one-way SLR with lasercom hardware is a major achievement and innovation since 2005 where the first experiment of GGAO laser stations (Goddard Geodesy and Astronomical Observatory) of the ILRS have successfully performed interplanetary one-way laser ranging. In this way INRRI could be useful to start this technique also on Mars.

- Laser flash: an orbiter emitted a flash retroreflected by INRRI then acquired by digital cameras.

35
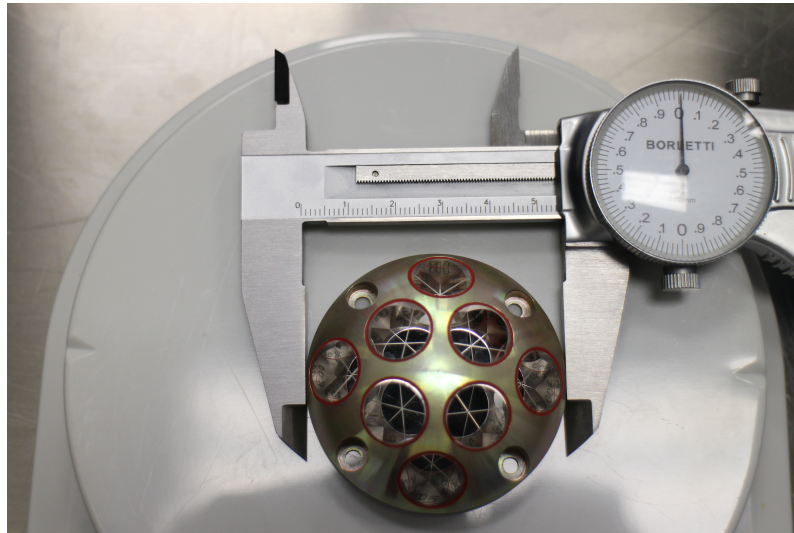
(a) *INRRI dimensions.*
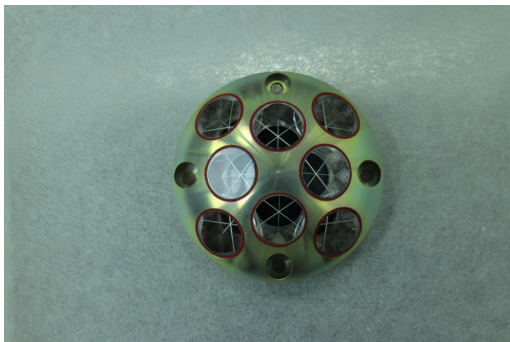
(b) *External view.*
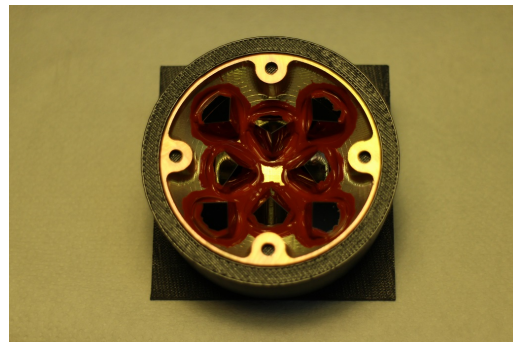
(c) *Internal view.*

Figure 3.9: INRRI retroreflectors glues to the Aluminum chassis
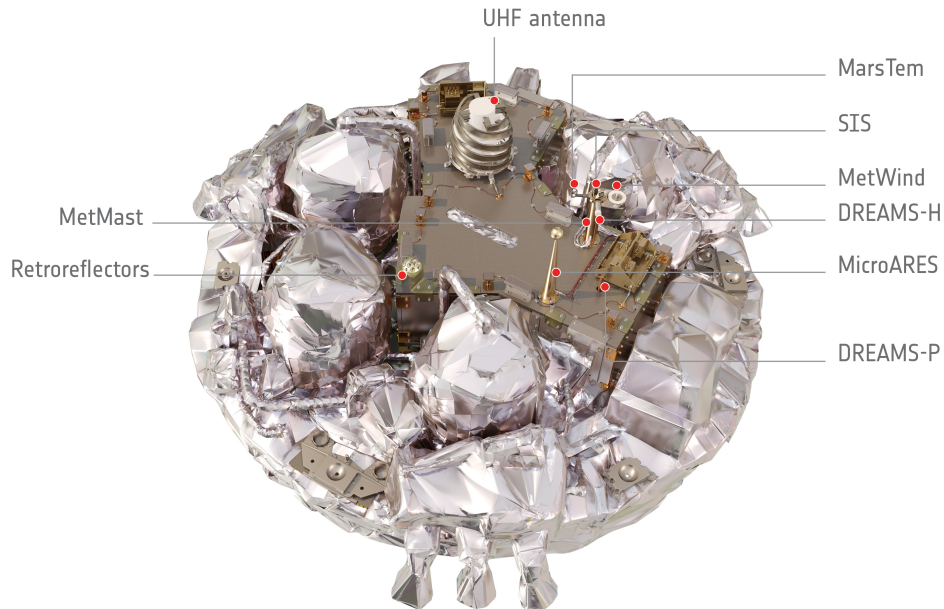
Figure 3.10: ExoMars EDM with the scientific instruments. INRRI is tagged as
"Retroreflectors"

See figure 3.11 for a cartoon showing possible INRRI employment.
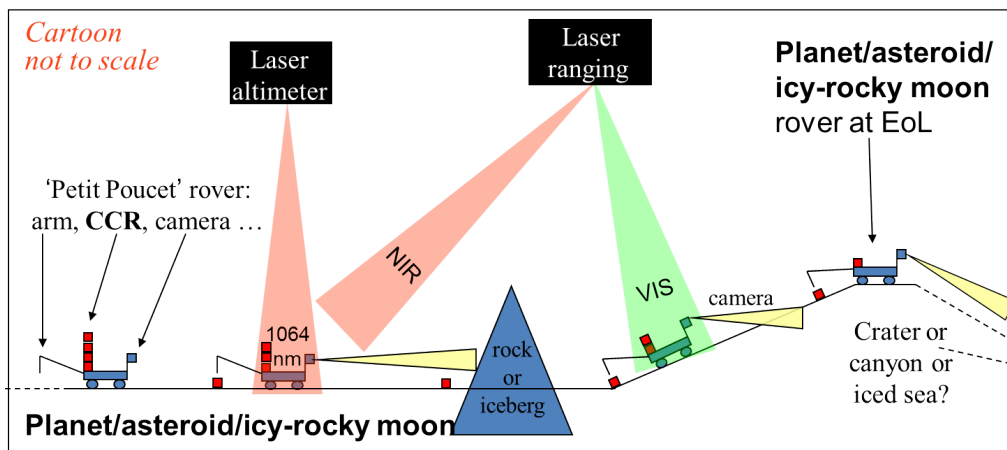
Figure 3.11: INRRI concept cartoon

The INRRI part of my PhD thesis project is focused on the first scientific goal described before (in addition to the flight qualification tests described in Chapter 5): use the payload as a long term instrument for optical detection (by future experiments) for GR tests, as was for the retroreflectors placed on the Moon by the Apollo astronauts and Lunokhod rovers since 1969 and still in use. In this way Mars will become a laser ranging test body for GR tests like today is the Moon. Most of all, Mars can provide GR tests complementary to the LLR ones thanks to the greater distance from the mass generating the main gravitational field: for the Moon is the Earth with an average distance of 385×10^3 km, while for Mars is the Sun with a average distance of 228×10^6 km. For example with Mars it is possible to increase the accuracy in the PPN parameter β and the variation of the gravitational constant respect to the Moon. Most of all the LLR with the Martian Laser Ranging together with Mercury, Cassini at Saturn, can provide redundant and independent experimental measurements of the same physics observable(s) or of coherent sets of physics parameters within a given, consistent gravity model (like GR).

For the details about the INRRI GR simulations carried out and its results please refer to Chapter 6.

Chapter 4

The SCF_Lab: Hardware and Software

The goal of this Chapter is to describe the SCF_Lab infrastructure, with particular emphasis in the subsystems used for the MoonLIGHT-2 and INRRI experimental tests described in Chapter 5

The SCF_Lab is an ISO 7 Clean Room (class 10.000) with an area of 85 m^2, built by INFN-LNF over the years starting from the Extra Terrestrial Ranging to Unified Satellite COnstellations (ETRUSCO)-2 and MoonLIGHT research project (respectively [Dell'Agnello 2011] and [Martini 2012]) in 2010-2011. The clean room in fact can provide optimal conditions during the setup of the CCRs for the tests, avoiding any dust particle on the retroreflectors that could decrease the test integrity. The core instruments of the laboratory are the two climatic chambers, the SCF and the Satellite/lunar/GNSS laser ranging/altimetry and Cube/microsat Characterization Facilities - Galileo optimized (SCF-G) cryostats, both of them equipped with the fundamental hardware to run the facilities and characterize the thermal and optical properties of CCR for LLR (and SLR). The two facilities are climatic chambers that reproduces the space conditions in terms of pressure and temperature, reaching in the operative phase a pressure less then $10^{-6} mbar$ and a temperature T_{shroud} around 90 K. For each facility there is a dedicated Solar Simulator (SS) (outside

the chamber) that reproduce the solar radiation Air Mass 0 (AM0) spectrum, illuminating the CCR inside the chamber through a solar quartz window installed on the chamber frontal cap. In addition the chambers are equipped with two other windows, one IR Germanium window and one optical window, both placed on the side of the cryostat for the thermal and optical tests apparatus respectively. The payload is placed inside the chamber on a specific support and can be rotated by an external movement system coupled with a dedicated software in order to change its orientation with respect to the solar window, IR window or the optical window (depending on the test phases).
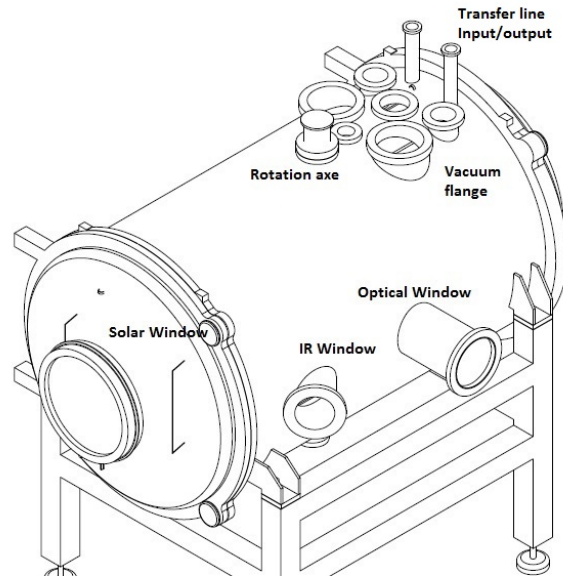
Figure 4.1: Schematic view of SCF-G facility with in evidence the main elements.

The SCF-G is the chamber designed for the MoonLIGHT-2 and INRRI characterization tests (refer to figure 4.1 for a schematic view of the SCF-G), so in the following sections, it will be described the key subsystem needed for the characterization test and data acquisition. These subsystems can be summarized in:

- *SCF-G Cryostat and Cryogenic system*: the facility itself used to reproduce

the space environment in terms of pressure and vacuum (see section 4.1).

- *Data Acquisition, SS and thermal control*: the subsystem dedicated to the data acquisition of invasive thermometry (PT100 probes), chamber pressure reading, remote movement system control, payload temperature control and the monitoring of SS AM0 solar spectrum (see section 4.2).

- *IR thermometry subsystem*: the subsystem composed by the hardware used for IR pictures acquisition and the software package used for payload surface temperature data analysis (see section 4.3).

- *Optical subsystem*: the subsystem composed by the hardware to the FFDP acquisition, along with the software package for data analysis (see section 4.4).

4.1 SCF-G Cryostat and Cryogenic system

The SCF-G Cryostat and Cryogenic subsystem consist of:

- The SCF-G cryostat (composed by an external steel envelope and an internal copper shroud).

- The SCF-G vacuum system.

- The SCF-G cryogenic Liquid Nitrogen (LN2) system.

The cryostat

The SCF-G cryostat is composed by a cylindrical steel structure, closed in its two terminal parts by two steel spherical caps. The cylinder dimensions are 1236 mm diameter for 2140 mm length (figure 4.2a).

Inside the cryostat there is a cylindrical copper shroud painted with black Aeroglaze Z306. On the shroud a cooling coil for the LN2 is soldered, used during the SCF-G
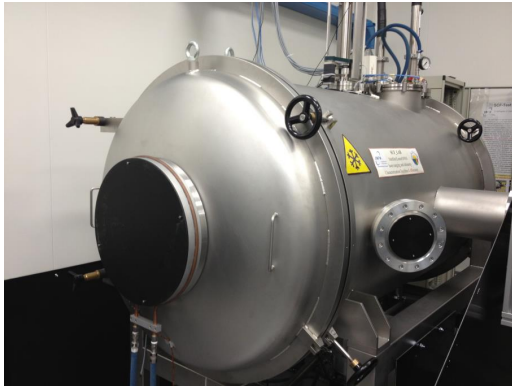
(a) *The SCF-G cryostat with the front spherical cap.*
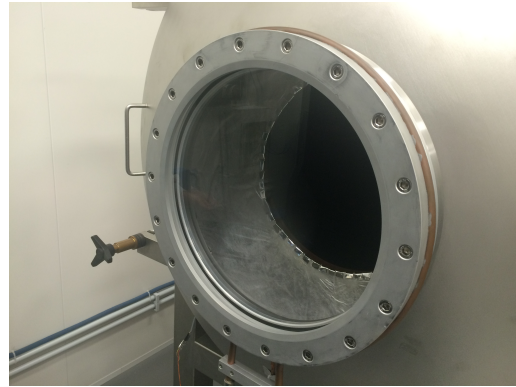
(b) *Solar window.*
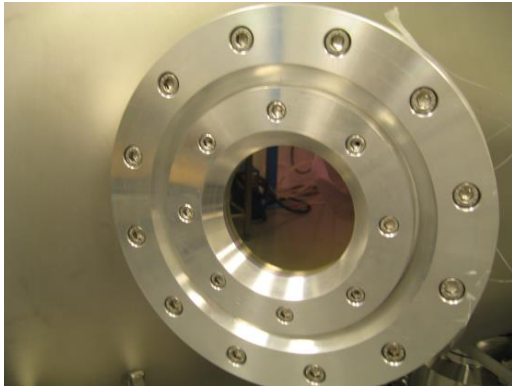
(c) *IR window.*
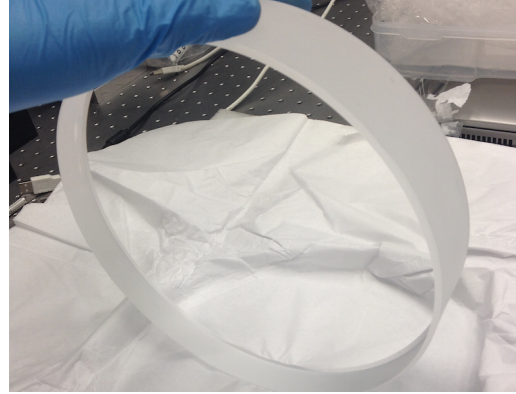
(d) *Optical window.*

Figure 4.2: The external view (front) of the SCF-G , with the three windows in details

operative phases. In these phases, when the LN2 fully fill the cooling coil, the SCF-G shroud reaches temperature of 90±10 K degree (depending on probes position). On the shroud and on the steel cryostat there are 3 different holes for the three windows: On the front spherical cap take place the quartz solar window (4.2b) with 370mm diameter. A PT100 probe on its flange is installed dedicated to monitor the flange temperature when the SS is turned on. Through this window the SS can illuminate the payload inside the chamber.

On the side of the cryostat, with 45° respect to the vertical axis passing through

the solar window (longitudinal axis) is installed a Germanium window (figure 4.2c) with 80mm diameter. Germanium is transparent to the IR and the window is used for the acquisition of the IR pictures with the IR camera.

With an inclination of 90° respect to the longitudinal axis takes place the optical window in fused silica with 230mm diameter (figure 4.2d). This one is used for the CCR optical interrogation.

The shroud (both cylindrical structure and caps) is shielded with 10 layer of COOLCAT 2 NW Multi-Layer Insulation (MLI), in order to ensures the thermal isolation from the external environment and reduce the LN2 consumption. Along all the shroud surface are installed 48 PT100 probes for temperature control, divided in two different circuits each one with 24 probes, in addition with a series composed by 11 Resistive Kapton Heaters. These are installed and remotely controlled by a dedicated software, in order to thermally control the shroud temperature when needed (section 4.2).

On the upper part of the cryostat are placed different vacuum flanges (see figure 4.1) dedicated to: cables for the payload thermal control inside the chamber, reading of PT100 on shroud and movement system control (section 4.2). In addition the rotation axis of movement system is directly connected to a vertical bar through a hole in the upper part on the shroud; this bar goes inside the cryostat directly connected to the payload holding structure where the payload is hooked. Externally the vacuum chamber on the rotation axis is installed a potentiometer (section 4.2) in order to read the payload orientation without using the encoder of the movement system and verify the position of the payload during the tests.

Vacuum System

The SCF-G vacuum system is composed by two different pumps:

The oil rotative pump used during the pre-vacuum phase and as backing pumping mode for the turbomolecular pump. The pump, placed outside the clean room is connected to the cryostat by two valves: "rough" and "fine". The "rough valve" connects directly the chamber and pump during the pre-vacuum phase, in this phase

the camera reaches a pressure around $10^{-1} mbar$. The "fine valve" connect the rotative pump in backing pump with the turbomolecular pump (the "rough" valve must be closed in order to switch safely in this state) during the operative conditions. Between the rotative pump and the cryostat, outside the clean room, is placed a cold vacuum trap cooled with LN2, in order to avoid that any oil particles go inside the chamber.

The turbo molecular pump is used when the camera must reach the operative conditions (high vacuum, with a pressure at least $10^{-6} mbar$). The pump take place inside the clean room directly below the SCF-G and is connected to the chamber between the "Gate" valve.

"Gate", "Fine" and Rough" are electronic valves type and are manually controlled with knobs placed on the control box (figure 4.3), placed in front of the SCF-G . In addition on the control box is placed a vacuum sensor reader that reports the pressure inside the chamber acquired by the sensor. This pressure value is also acquired by the data acquisition system and digitally stored, see section 4.2 for details.

Cryogenic System

The LN2 cryogenic system is designed to cool down the climatic chamber at 90 K, right after the pressure operative conditions of $10^{-6} mbar$ are reached. The LN2 flows from a tank placed outside the laboratory, then through a transfer line it goes inside the shroud. There the LN2 cools the shroud and, once completed the path in the cooling coil, goes out from the cryostat across the second line of transfer line, and finally trough this line goes outside the SCF_Lab. On this second line there is an heating pipe to heat up the LN2 and transform it in gaseous form and then an exchanger to free it safely in the environment outside the laboratory.

On the first transfer line is installed a fluxmeter in order to remotely control the flow with a specific Laboratory Virtual Instrumentation Engineering Workbench (LabVIEW) SW, therefore called Virtual Instrument (VI). The fluxmeter works in
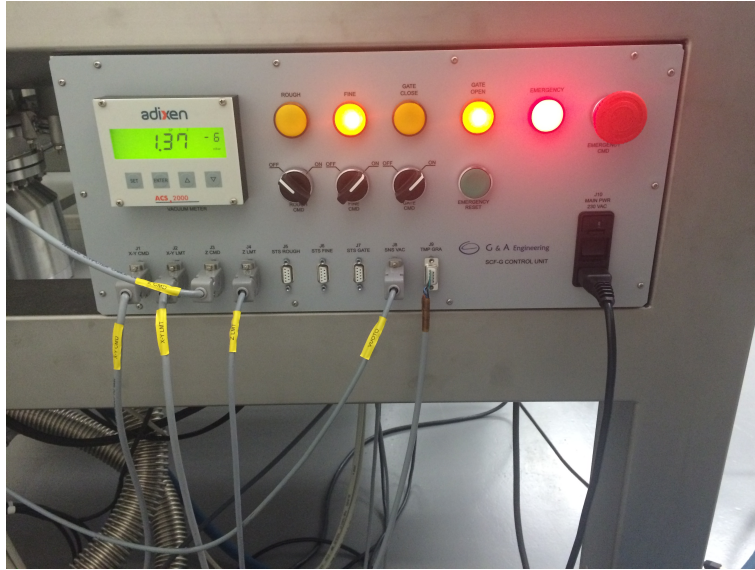
Figure 4.3: The SCF-G control box for vacuum subsystem control with the vacuum sensor reader in the upper left

two modes:

"analog mode" where the user must set a LN2 flux setpoint, between 0 and 400 l/min, with the specific LabVIEW SW (see section 4.2) and "digital mode" where the user must chooses between the "valve open" configuration, where the fluxmeter control is turned off and all the LN2 goes inside the SCF-G , and "valve closed" where the fluxmeter deflect all the LN2 on the heater exchanger.

The fluxmeter temperature is controlled with a PT100 placed in input at the device acquired by the National Instrument (NI) compact Field Point (cFP) (section 4.2). In this way the user can check the fluxmeter temperature and avoid any freeze at the device.

To reach the operative conditions from "air conditions" ($pressure = 10^3 mbar$ and $T_{shroud} = 300K$) the system takes about 2 h: 1 h for the vacuum system to realize the hight vacuum inside the chamber and another 1h to the cryogenic system to cool the shroud at 90 K.

4.2 Acquisition, Control and Solar Simulator subsystems

The Data Acquisition/thermal and SS control subsystem consist of:

- The Hardware for monitoring and thermal control the SCF-G (PT100 probes, vacuum reader, fluxmeter, movement system) and the payloads (PT100 probes and thermal heaters).

- All the SW (developed with LabVIEW during my PhD activities) used to monitor and control the hardware described above during the test phases.

- The SS Hardware.

The first two points are related to the Data Acquisition/thermal control subsystem and will be described in the following subsection, then I will describe separately the SS.

Data Acquisition/thermal control

The Data Acquisition/thermal control system is dedicated to the control of the movement system, payload temperature and monitoring of all the vacuum chamber subsystems during the test phases in the SCF_Lab. The various VI used to accomplish this task could be summarized in: Temperature data acquisition system and fluxmeter control, Payload and shroud heaters remote control, Movement system control. All these SWs were developed during my PhD thesis for the MoonLIGHT-2 and INRRI experimental tests at SCF_Lab (Chapter 5).

 - *Temperature data acquisition system:* This system acquires/monitors all the PT100 probes [1] described before along with the vacuum reader and the fluxmeter. The probes (trough dedicated modules), the vacuum reader (trough a serial connection) and the fluxmeter (trough a custom board connected to a Digital Analog

---

[1]for reference: http://www.lakeshore.com/products/cryogenic-temperature-sensors/platinum-rtds/models/pages/Specifications.aspx

Input/Output module) are all acquired with the NI cFP 2220. The cFP 2220, controlled by a dedicated PC, runs then two different dedicated LabVIEW VI: the acquisition and the fluxmeter program. These VI works both in "real time" conditions, in other words the cFP provides the maximum priority to the codes, in order to guarantee always the right timing of the acquisition. The acquisition VI acquire, plot then save all the temperature/pressure data automatically in the cFP internal memory. Refer to figure 4.4 for the acquisitionVI showing as all the temperature probes along with the pressure value acquired, plotted and saved.

- Payload and shroud heaters remote control: As previously explained in section 4.1, the SCF-G shroud is equipped with a series of 11 resistive Kapton Heaters tape, in order to increase the shroud temperature from 90 K to 300 K and break the vacuum in a short time or, if needed, control the shroud at a fixed temperature. The control system is composed by a heater power supply in series with a controllable relay. The relay can split the current provided by the power supply on the shroud or on a dissipator. The relay and the power supply are connected to the PC respectively with a serial RS232 and Can-ethernet connection. With a dedicated VI is possible to control the relay to take the shroud at a fixed temperature.

In addition, during the test we must control the payload at a fixed temperature. For MoonLIGHT-2 two resistive heater tapes (with four wires configuration) are installed on its housing in order to ensure the payload thermal control, while for INRRI only one tape (with one wire configuration) is installed. In both cases each heater is powered by a dedicated power supply, that is remotely controlled with a dedicated LabVIEW VI using the Digital Analog Input/Output module module on the cFP (figure 4.6). The VI ensure the thermal control searching the best current/voltage supply for the heater in order to set the payload at a fixed temperature. In other words the codes checks the equilibrium condition between the power dissipated by the heaters on the payload (left term of the equation 4.1) and the power dissipated by the payload with the environment trough radiative exchange(right term equation 4.1).

$$Ri^2 = \sigma A \epsilon \cdot (T_{payload}^4 - T_{shroud}^4) \tag{4.1}$$

where:

- R is the Resistance (Ohm) of the heaters

- i = Current (Ampere) trough the heaters

- σ is the Stefan Boltzmann constant ($\sigma = 5.67 \cdot 10^{-8}$ W/m^2 K^4)

- A is the effective Area (m^2) of radiative exchange

- ϵ is the payload emissivity

- $T_{payload}$ is the payload temperature

- T_{shroud} is the shroud temperature

With the VI it is possible to work in "manual" mode, where for each power supply (and so each heater tape) the user can sets manually the desired current, or work in "automatic" mode, where the user set only to the desiderated "setpoint" temperature and then program automatically controls the heaters in order to reach and hold it. In this last mode the VI must acquire the housing average temperature along with the shroud average temperature (via global variable from the acquisition.vi) and put these in feedback with the setpoint value. Then using a specific PID (Proportional-Integral-Derivative) control with the equation 4.1, the code chooses the right current for the heater tape. The "automatic" mode is used during the tests, to provide an accurate control of the housing temperature within an error of $\pm 1K$ with respect to the setpoint (the probes accuracy is about $\pm 0.2 - 0.5K$, depending on the working range temperature). Such accuracy is mandatory during all the tests phases.

- *Movement system control:* With the movement system the user can rotate the payload in order to face it at desiderated position. The rotation axis can rotate of around 280°: starting from payload facing the cool shield (corresponding to $-90°$ with respect to the payload facing the solar window) and ending to the payload facing the optical window ($+90°$ with respect to the payload facing the solar window) with a resolution of 0.1°. The rotation motor is a step-step motor (installed above the SCF-G vacuum chamber) with the Pollux-NT as motor controller (located inside

the SCF-G control box) connected to the PC with a serial-ethernet connection. In addition a rotational potentiometer is installed on the external rotation axis (figure 4.5) in order to read the absolute position of the payload regardless the control Pollux reading (for example if the electrical supply of the Pollux controller is cut off). The potentiometer reading is acquired by an "Arduino UNO R3" logic board, connected to the PC with an ethernet switch.

The movement system VI (figure 4.5) works with the Pollux controller and Arduino UNO allowing the full control of the movement system with manual rotations (the user can rotate the payload manually) choosing between a relative movement from the last position or an absolute rotation from the "zero" value, or also using a set pre-defined position.

Finally a set of indicators reports the status of the movement system (if it is moving or not), the actual position acquired by the controller along with the position acquired by the potentiometer, and if necessary the limit status that defines the "zero" value for the absolute movement.
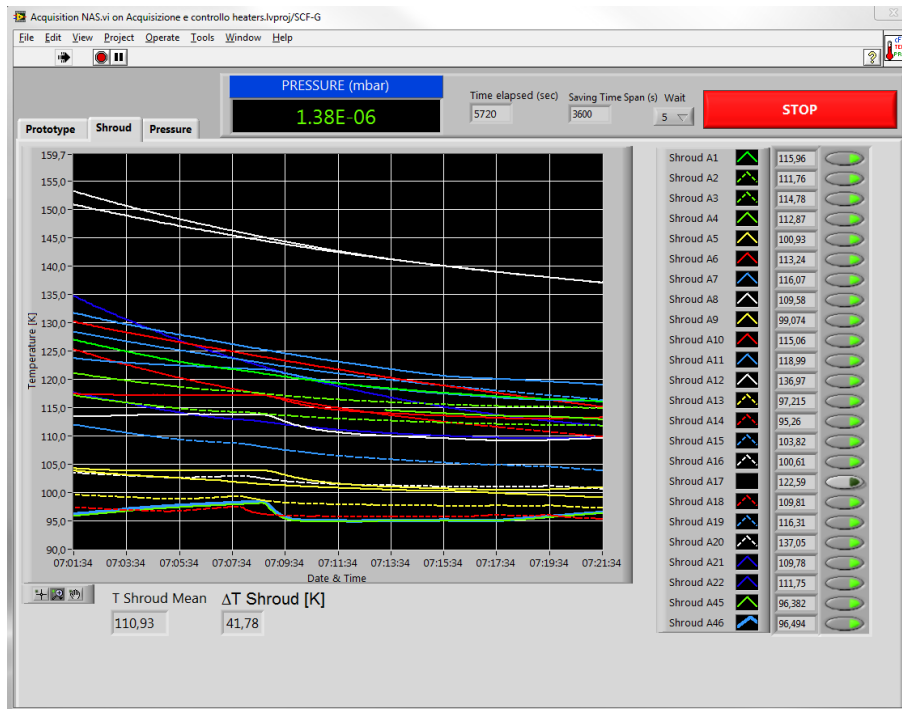
Figure 4.4: VI for SCF-G "real-time" monitoring: temperature probes (PT100) and pressure reading
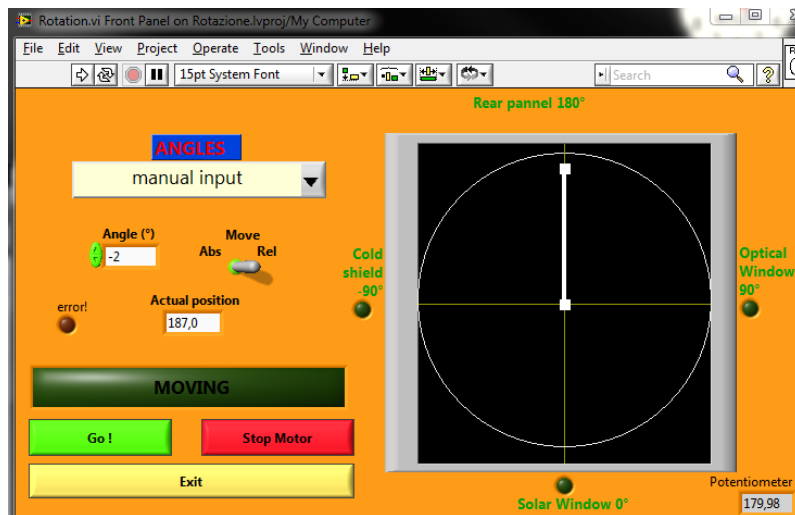
Figure 4.5: VI for rotation system movement remote control
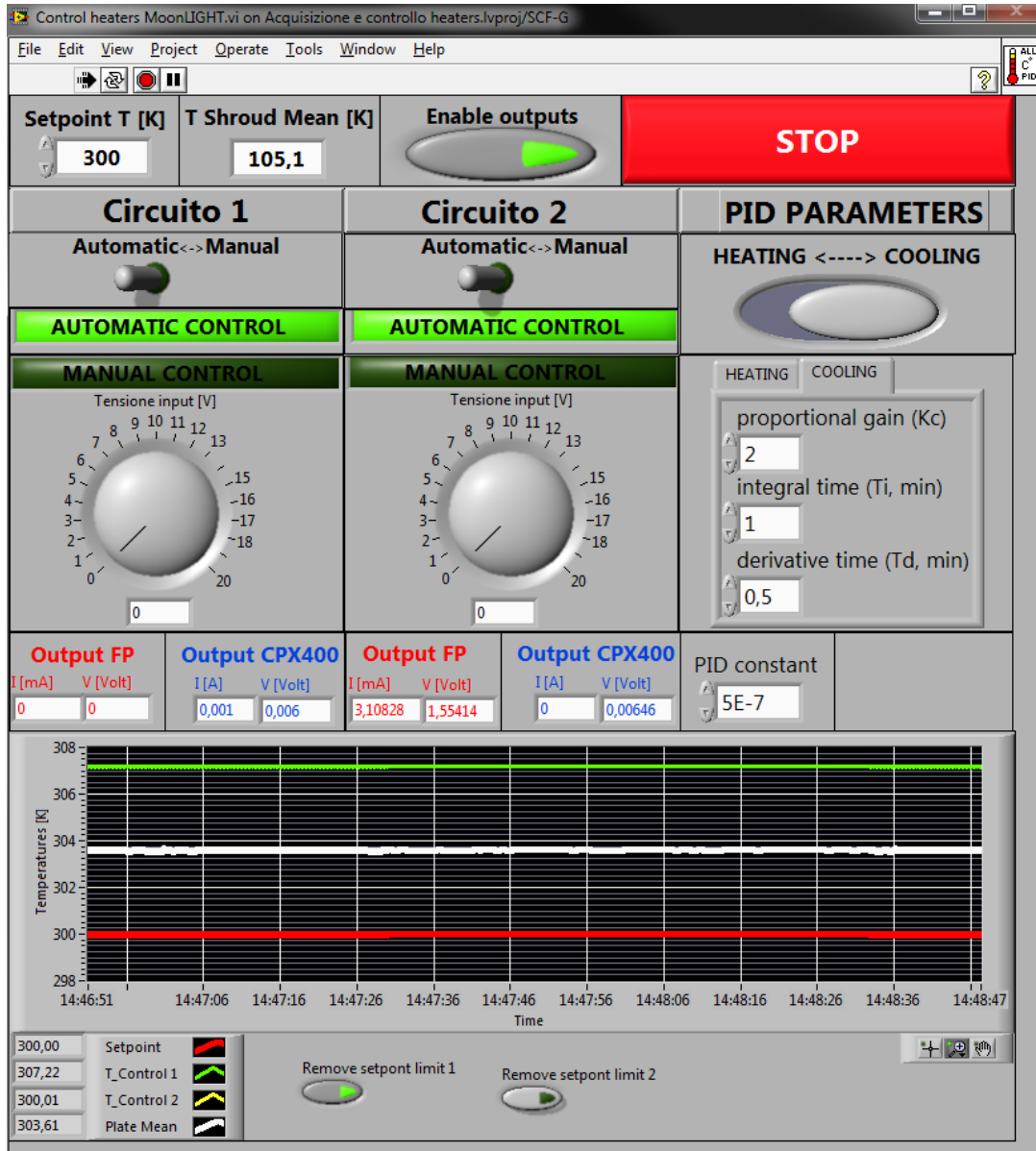
Figure 4.6: VI for "real-time" paylolad temperature remote control

Solar Simulator subsystem

The SCF-G SS (figure 4.7a) is a class A SS manufactured by TS Space Systems LTD [2] . The SS is composed by a metal halides lamp with a nominal power of 6kW capable to emit a radiation of $\sim 1.4kW/m^2$ (the solar constant). Right after the lamp there is a mask of optical filters to shape the radiation spectrum from the lamp and match it with the real solar spectrum (without changing its intensity). This mask is composed by 5 shaded and 44 unshaded filters, for 49 filters in total each one with dimensions around $[5x5]cm^2$, placed in a holder with the scheme reported in figure 4.7b. Finally there is a shutter, cooled with a coil where flows cold water, manually controlled by an air compressed system to block the beam during the tests without turning off the simulator.

The SS is controlled by a custom control box that automatically puts the lamp in the operative conditions (50V and 115A, equal to roughly 95% of its maximum power) also controlling the internal temperature of the Simulator with a PT100 (shutting down the system if the internal temperature exceeds 80° C). To complete the start up procedure, it takes around 30 minutes.

The SS is designed in terms of distance between lamp and opening, lamp power dimensions and filters, specifically to obtain three key features at the payload distance (1.1 m from the shutter):

- The beam divergence allows the illumination of 420 mm diameter surface (for reference MoonLIGHT-2 is 100mm diameter).

- The output beam uniformity is $\pm 5\%$ inside a circle surface with 350 mm diameter. The measured uniformity during the calibration phase before the MoonLIGHT-2 test is $\pm 3.12\%$ with a central beam intensity of $1474.65W/m^2$, respect to the solar constant value.

- A close match with the AM0 spectrum. The AM0 is defined as the Solar Spectrum, outside the Earth atmosphere in the interval 400-3000 nm within

---

[2]for reference: http://www.ts-space.co.uk/
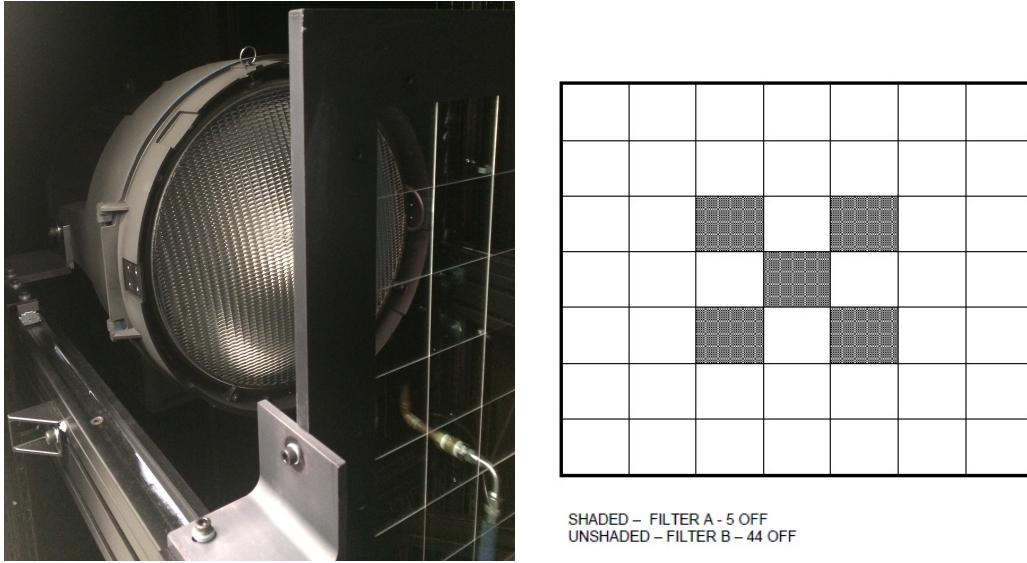
(a) *Internal view of the SCF-G SS. On the left side there is the Osram lamp, on the right side the filters.*

(b) *The SS filters scheme.*

Figure 4.7: The SCF-G SS, internal hardware and filters scheme

the standard IEC 60904-9. Figure 4.8 shows the SCF-G SS spectrum with respect to the AM0 standard spectrum, along with the values for each band (recorded during the validation test that I carried out) compared it to the nominal IEC 60904-9 spectrum range. This standard compares the integral of the SS spectrum within specific spectral bands to the nominal distribution of the AM1.5 spectrum. Computing the percentage of this integral within the band respect to the integral of all spectrum we can verify if it is inside the nominal limits. In the lower part of figure 4.8 we have for each spectral band from left ro right: the nominal AM1.5 distribution, the integral within the band and the percentage respect to the total spectrum, and the limit for a class A SS. The data demonstrate that the SS is a class A.

All of these features allow the SS to closely reproduce the real Sun illumination present on the Moon, in terms of uniformity and spectrum. During my PhD activity
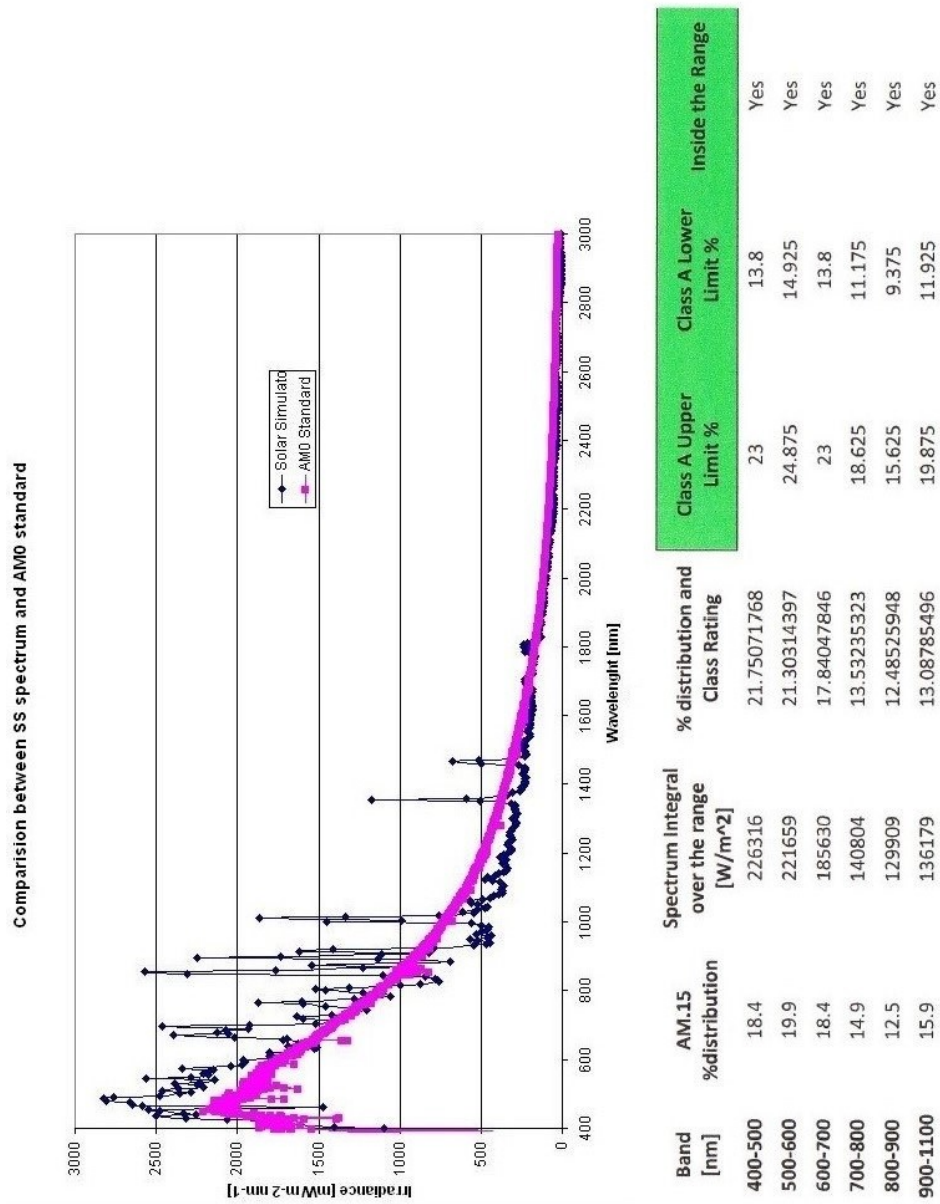
Figure 4.8: The SCF-G SS spectrum w.r.t. the AM0 spectrum.

I carried out the qualification test campaign of the SS, along with the spectrum and uniformity analysis and check before each test campaign.

4.3   IR thermometry subsystem

The IR Thermacam subsystem is dedicated to acquisition and analysis of CCR front face temperature (trough IR pictures) and it is composed by the FLIR Thermacam (figure 4.9), the FLIR Researcher SW and some Matlab custom codes. This section and the section 4.2 describe the Hardware and SW that I used for the experimental part of this work.

The Thermcam, is a digital camera with a Charge Coupled Device (CCD) provided with automatic electronic zoom, and works in the spectrum range 7.5-10 μm, corresponding to the far infrared radiation spectrum. The temperature accuracy measurement is ± 2 K for single spot, or $\pm 2\%$ reading with a thermal sensitivity ≤ 0.02°C at 30°C. The camera resolution is 640x480 pixels and in figure 4.11 it is possible to see an example of MoonLIGHT-2 IR picture taken during one of the experimental tests (the picture is not calibrated so the temperature showed does not represent the real payload temperature). In figure 4.10 are summarized the main specifications of the camera.

Figure 4.9: The SCF-G Thermacam.

Imaging performance	Accuracy	± 2.0°C (± 3.6°F) or ± 2% of reading
	Thermal sensitivity	< 0.06°C (< 0.11°F) @ +30°C (+86°F)
	Spatial resolution	▪ 40 mm lens: 0.66 mrad ▪ 19 mm: 1.3 mrad ▪ 76 mm: 0.33 mrad ▪ Close-up lens (P/N: 1196683): 50 μm
	Electronic zoom	Continuous interpolating zooming on images
	Panning	Panning over zoomed-in images
	Digital image enhance-ment	Adaptive digital noise reduction
Detector	Detector type	Focal Plane Array (FPA), uncooled microbolometer 640 × 480 pixels
	Spectral range	7.5–13 μm
Image presentation	Display	5.6 in., 1000 × 600 pixels
	Viewfinder	800 × 600 pixels
	Frame rate	30/25 Hz (PAL/NTSC)

Figure 4.10: IR camera SC-640 by FLIR

The pictures acquired with the camera are then analyzed with the dedicated FLIR Researcher SW provided by the camera producer. The FLIR researcher SW calculates the temperature of a specific spot with known emissivity once defined:

- environment temperature and humidity.

- distance between spot on the object and camera.

- reflected apparent temperature.

- optical transmissivity.

The thermacam is placed, during the tests, on a tripod in front of the Germanium IR window with a transmissivity of 0.97, and the SCF-G is in vacuum condition so we can assume humidity to 0%. In this way the distance parameter is useless because there is no absorption/emissivity in IR range from the air O_2 molecule. The reflected apparent temperature, is the key element used to calibrate the camera along with the body emissivity.

The object temperature is given by the equilibrium condition between the radiation

emitted by the object (interested signal) and the environment radiation reflected by the object to the camera (the noise background signal). So we can write this general equation as:

$$W_{tot} = W_{obj} + W_{ref} \tag{4.2}$$

We are in vacuum condition and the payload decoupled from the movement system so we can remove the convective/conductive exchange and assume that the only possible thermal exchange is radiative. In this way we can express the equation 4.2 with:

$$W_{tot} = A_{obj} \cdot \sigma \cdot \epsilon_{obj} \cdot (T_{obj}^4 - T_{env}^4) + A_{obj} \cdot \sigma \cdot (1 - \epsilon_{obj}) \cdot (T_{ref}^4 - T_{env}^4) \tag{4.3}$$

where:

- W_{tot} is total IR radiation acquired by the IR camera

- W_{obj} is the total IR radiation emitted by the object at temperature T_{obj} with emissivity ϵ_{obj}

- W_{ref} is the IR radiation emitted by the environment and reflected by the object to the camera. In order to simplify the problem the environment radiation is approximated as a black body radiation with temperature T_{env}

- σ is the Stefan-Boltzmann constant

- A_{obj} is the object surface, in the approximation that for the IR camera point of view, the object emissive area is equal to the retroreflector optical reflective area.

- T_{env} is the environment temperature, or the SCF-G shroud temperature, with 90 K as average value.

In other words, to obtain the object temperature we must measure the reflected temperature and remove it from the total radiation collected. With the background

radiation, described by T_{ref}, we can obtain W_{obj} and hence T_{obj} solving equation 4.3 in:

$$T_{obj} = \sqrt[4]{\frac{1}{\epsilon_{obj}} \cdot \left[\frac{W_{tot}}{A_{obj} \cdot \sigma} - (1 - \epsilon_{obj}) \cdot (T_{ref}^4 - T_{env}^4)\right] + T_{env}^4} \qquad (4.4)$$

All these steps are automatically carried out by the FLIR Researcher SW once the user sets manually the reflected apparent temperature or T_{ref} that is extrapolated from the following calibration procedure:

1. set a spot on the IR picture in a place with known temperature and emissivity (usually a small piece of Kapton tape near a PT100 probe acquired by Acquisition.vi).

2. find the right reflected apparent temperature which give a T_{obj} equal to the temperature read by the PT100 (using equation 4.3).

3. set the obtained reflected apparent temperature as reflected temperature for all the other points in the IR picture.

In this way the FLIR SW will provide the temperature of any object in the IR picture with known emissivity, and also the MoonLIGHT-2/INRRI front face CCR temperature.

It is important to underline that with the FLIR SW it is also possible to obtain the average temperature of an area (and so the average temperature of all payloads front face), see Chapter 5 for payloads detailed thermal analysis. Finally with the IR camera we can be take IR pictures programmatically with a user defined time span.

Regardless all the calibration process described it is right to remember that the Thermacam is designed mainly as an instrument for differential measurement temperature and the main goal during the test is to obtain the CCR thermal constant that depends on the CCR temperature variation during time (see Chapter 5 for test
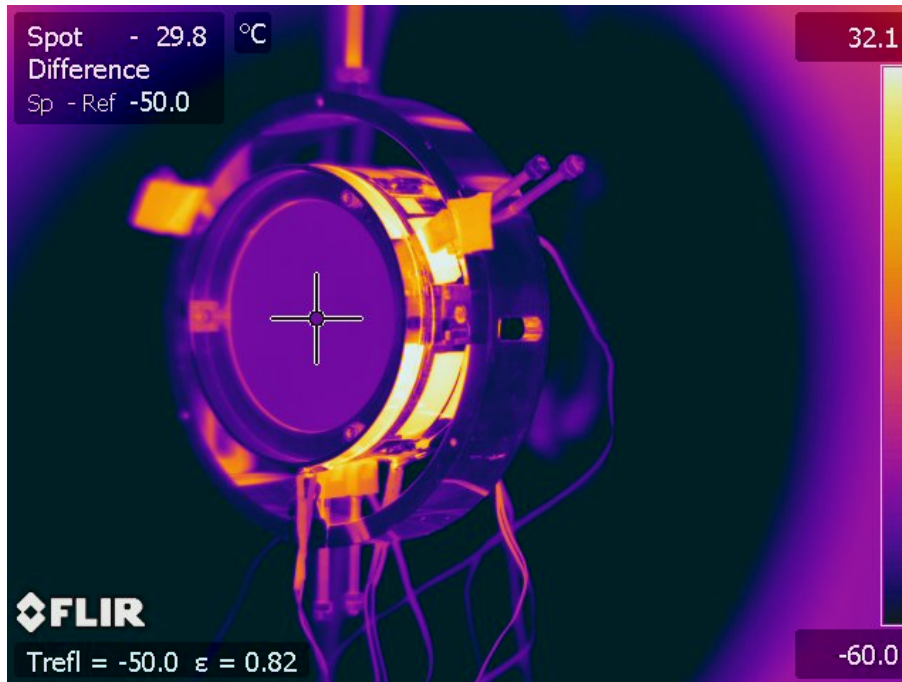
Figure 4.11: A sample of an IR picture of MoonLIGHT-2 with FLIR SC 640 Therma-
cam, **the picture is not calibrated**.

details). The main test results are independent from the calibration that provides
only an indication about the CCR front face absolute temperature.

4.4 Optical subsystem

In this section the characteristics and the key components of the optical bench will be described (see figure 4.12) along with procedure to simulate the laser ranging beam. The key point of the CCR optical test basic industrial acceptance test at
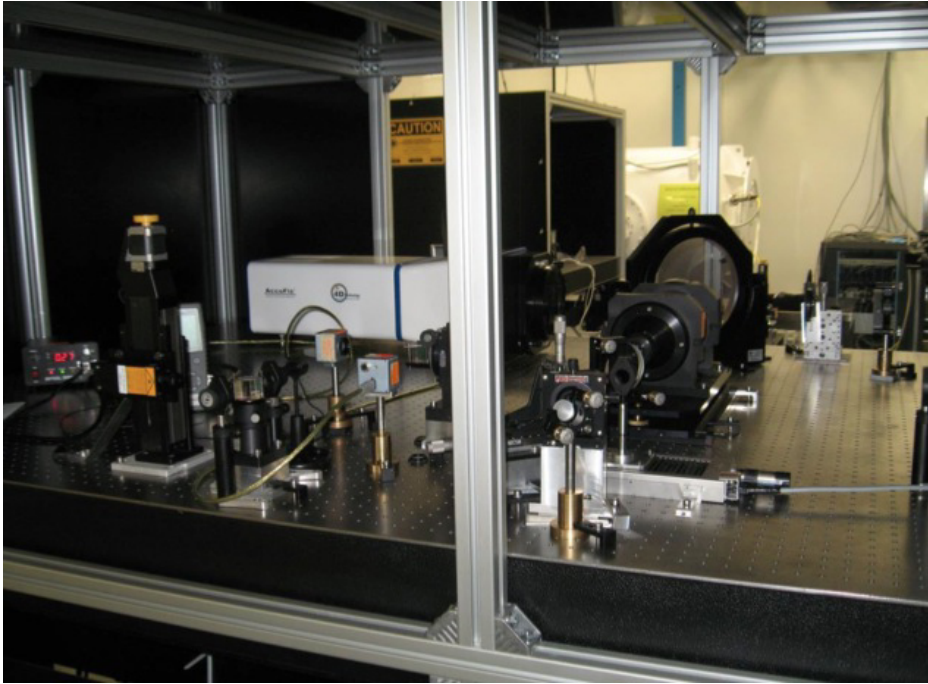
Figure 4.12: Picture of the optical bench

SCF_Lab is the measurement of the absolute angular size, shape and optical cross section of single CCR - FFDP (the intensity distribution on the image plane) with linearly polarized continuous wave lasers.

The test bench is designed to separate the horizontal and vertical components of polarization of each FFDP. While no dependency is expected for coated CCR like INRRI, for uncoated CCR like MoonLIGHT-2 the FFDP has a strong dependency on the orientation of the input linear polarization, so recording the two polarization components at the same time is mandatory.

The laser beam profilers consist on two 12-bit CCD cameras read-out through Firewire or USB with a PC. FFDPs are acquired with the CCR in Air and Isothermal Conditions. To calibrate the absolute angular scale of the optical circuit we use the Young method (or double slit experiment) to test the consistency of each CCR FFDP with its nominal Dihedral Angle Offset (DAO) expressed in arcsec. The DAO ([Degnan 1993]) is related to the satellite velocity aberration, which is function of the orbital altitude as explained in figure 4.13. To calculate the optical response and obtain a realistic model of the optical FFDP and its variations due to thermal effects it is necessary an exact knowledge of the DAO specifications.
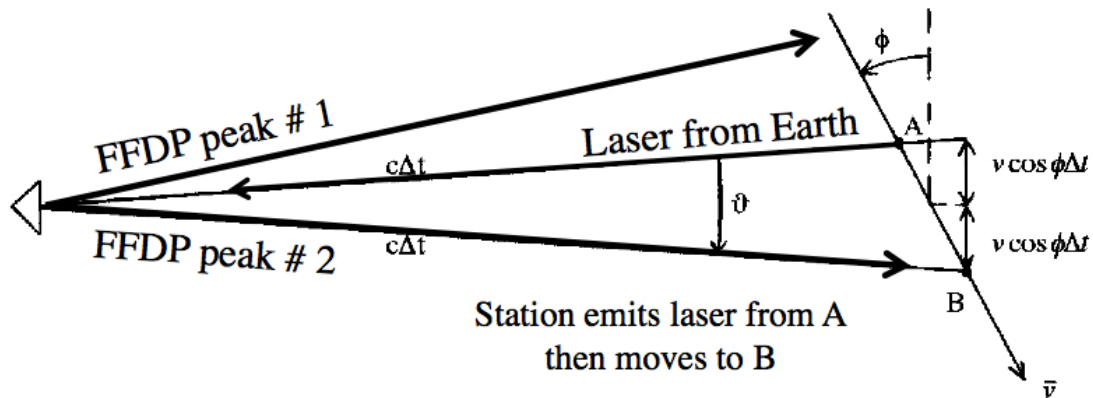
Figure 4.13: Velocity aberration

The velocity aberration is produced by the relative movement of the CCR on the Moon respect to the Earth during the laser pulse time of flight. During the study of the FFDP it is necessary to understand in which place the laser pulse retroreflected by the CCR will reach the starting station, and where the CCD is able to catch the incoming photons.

For the Moon the velocity aberration is about 4 μrad (the velocity aberration for the altitudes of GNSS constellations is 20-25 μrad), so in this case the best choice is a 0,0", 0.0", 0.0" (in arcsec) DAO. In fact the FFDP measurements modelled with CodeV (see appendinx A), suggest that the FFDP intensity is located in the central peak.

Finally it is important to underline that, in order to calibrate the bench during the test we measure the FFDP intensity relative to the Airy Peak, using reference flat mirrors of known reflectivity and good optical quality.

The optical bench layout is reported in figure 4.14, following the figure we have:

- a = Laser: the optical bench is equipped with a continuous wave laser. It has a beam diameter of 0.3 mm, a wavelength of 532 nm and a power of 90 mW

- b = Pre-expansion lens

- c and g = Cube polarizers: split the polarization of the beam coming out of the laser in two different components (horizontal and vertical respectively P and S). These two components of polarization are recorded separately because the FFDP has a strong dependency on the polarization

- d = Beam splitters: two beam splitters, one of 3 inches and one of 9 inches used to bend the laser beam

- e = Beam expander: a custom 20X beam expander to enlarge the laser beam to tested payload dimensions

- f = Circular Mask

- n = Double slit custom

- h and i = CCDs to record the FFDP components of polarization

- k and o = Mirrors: it is 4 inches flat broadband metallic mirror used for angular and intensity calibration for MoonLIGHT-2 tests

- l = Interferometer: Using a wavefront interferometer we can also test the optical quality of every component of the circuit and most important, we can make very precise measurements of DAO of our CCRs during every phase of the SCF-Test

- m = Power meter: The sensor of the power meter is able to measure power from 1 nW to 300 nW with an accuracy of 1%. The main scope of this component is to monitor every possible variation of the laser power during the measurement. We also use the power meter in order to measure the waist of the expanded laser beam.

- p+q = beam dump with custom slit
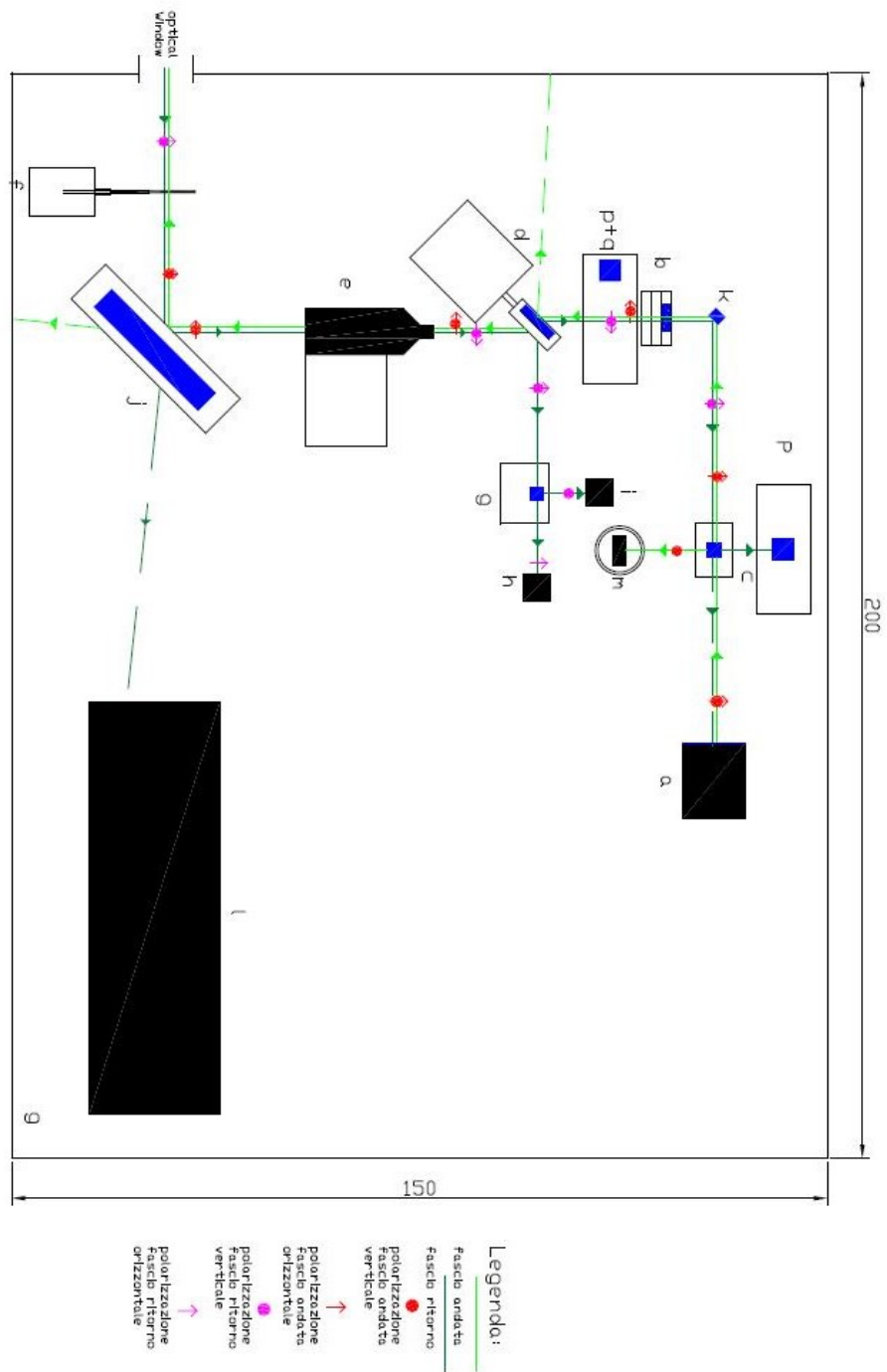
Figure 4.14: Optical bench layout during the test phase

Chapter 5

Experimental tests and analysis

This Chapter describes all the experimental tests and analysis carried out at the SCF_Lab in order to characterize the two payloads. The activity goal are:

- MoonLIGHT-2: study the thermal and optical behaviour before the first launch (out of four) scheduled for 2018, with the Moon Express missions.

- INRRI: qualify the payload for the flight acceptance test with the "Proton" launcher of Roscosmos, the Russian space agency (the same rocket used for both ExoMars-EDM and the next ExoMars Rover 2020 missions of ESA and Roscosmos).

In section 5.1 a general description of the MoonLIGHT-2 SCF-Test will be provided in order to describe in detail the three test campaigns in 5.1.1, 5.1.2 and 5.1.3. Each subsection will describe, respectively, the optical/thermal test procedures and results for each test carried out. Finally, the subsection 5.1.4 will discuss the test conclusions. Since the main focus on this section is on the IR and FFDP analysis, the temperature probes analysis that I carried out will be reported in Appendix C. Section 5.2 will be dedicated to the INRRI flight acceptance tests, with in subsection 5.2.1 the Thermo-Vacuum Test (TVT) carried out at the SCF_Lab and in subsection the vibration tests carried out at Study of Radiation Effects on Materials for Space Applications (SERMS). Except where indicated differently and explicitly I was

involved as member of the SCF Lab team both in the conception and in the execution of the test/qualification activities described in this Chapter, in particular I carried out the MoonLIGHT-2 thermal analysis and the INRRI TVT and analysis.

5.1 MoonLIGHT-2 SCF-Tests

The SCF-Test main task is to provide a concurrent measurement and modeling of the FFDP and the temperature distribution of the SLR/LLR retroreflector payload under space conditions produced with a close-match SS. The tests apparatus is described in Chapter 4, and can be summarized in an infrared cameras for non-invasive thermometry, PT100 probes for invasive thermometry, thermal control electronics and systems for real-time movement of the payload. In particular during the test MoonLIGHT-2 can be rotated in order to face the three SCF-G windows; the condition in which the payload faces the solar window is defined as "0° condition", instead with "90° degree condition" we have the payload facing the optical window. Refer to figure 5.1 for a graphic view of convention used to define the angle value w.r.t. payload orientation.

The SCF-Test goals are to study the CCR FFDPs under simulated space conditions (section 4.4), along with the CCR thermal constant (τ_{CCR}) and with the temperature on the other payload key structural component using PT100 contact probes. First of all, during the test MoonLIGHT-2 is mounted inside the SCF-G cryostat thermally decoupled from the shroud (see figure 5.2), then the test can be summarized in the following steps:

- reach the operative vacuum and cryogenic conditions with the SCF-G: internal chamber pressure about $\times 10^{-6} mbar$ and a T_{shroud} about 90K.

- control the MoonLIGHT-2 mechanical support structure temperature at a fixed value for the whole test. To ensure the payload thermal control I use two resistive wires heater types on the housing remotely controlled in order to fix the housing temperature ($T_{housing}$), to the expected test average value. Then
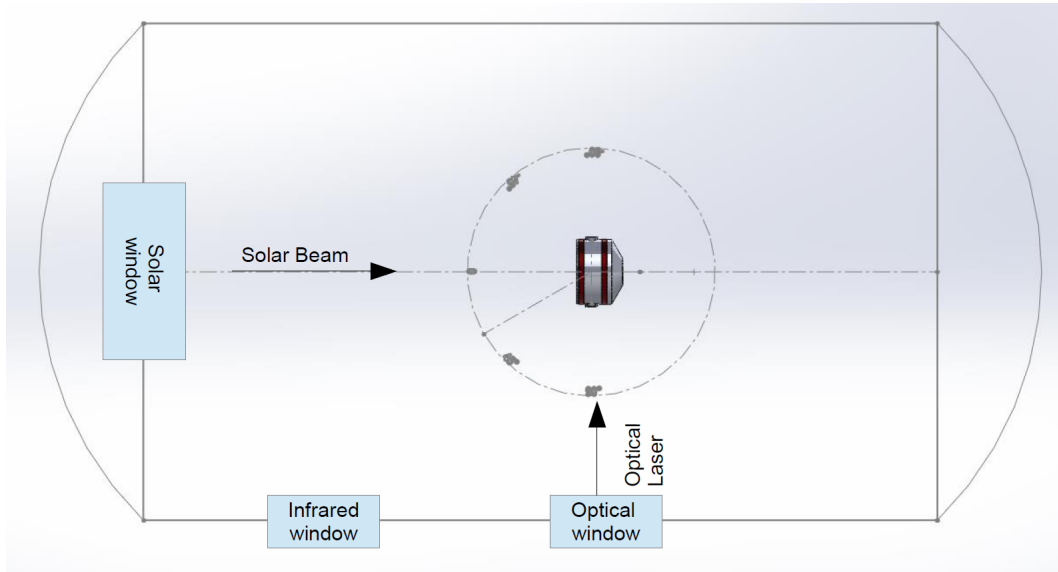
Figure 5.1: CAD sketch from an above viewpoint of the position of MoonLIGHT inside the cryostat, with respect to the solar window (left) and the laser window (down).

we wait plateau condition for MoonLIGHT-2 and SCF-G shroud temperature (front face CCR temperature and shroud PT100 probes are constant). In this phase MoonLIGHT-2 faces the optical window for at least 18h.

- After reaching the steady condition (we must kept plateau conditions for at least 30 minutes with temperatures at $\pm 1K$ respect to the setpoint) the test starts. The whole test can be schematized in the following steps:

  1. **Steady state conditioning**: we take 1 FFDP and 1 IR picture simultaneously in order to acquire the payload initial conditions before the test starts.

  2. **SUN ON heating phase**: MoonLIGHT-2 faces the solar window with a fixed angle (0° or 30°). Here we take only IR pictures with a fixed cadence. This phase lasts a defined time called t_{ON}.

  3. **SUN OFF cooling phase**: the solar illumination is shut off and the

payload faces the optical window. Here we take IR pictures with a fixed cadence and simultaneously FFDP with a different fixed cadence. This phase lasts a defined time called t_{OFF}.

The test can be repeated for different $T_{housing}$ and different inclinations between CCR and solar radiation during the SUN ON phase, in order to study the thermal and optical behaviour changes in different experimental conditions. Most of all, the conditions with 30° of inclination respect to the Sun represent the breakthrough condition, where the Sun radiation cannot be retroreflected and remains inside the CCR increasing the temperature and reducing the payload performances. These conditions represent the worst operative condition on the Moon.

In order to characterize the MoonLIGHT-2 performances we carried out three different test campaigns with three different payload configurations. In the following subsection will be described the procedure used for thermal and optical analysis, while starting from 5.1.1 will be described first the configuration used and the test carried out and then will be reported separately the thermal and optical tests results.
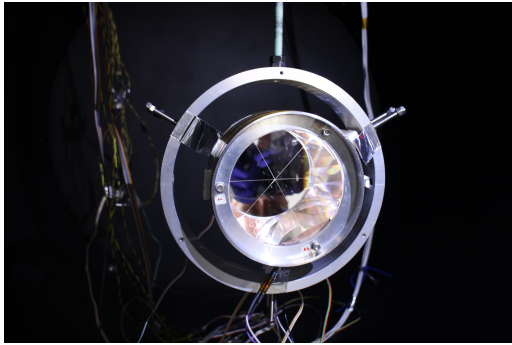
(a) *Front view.*
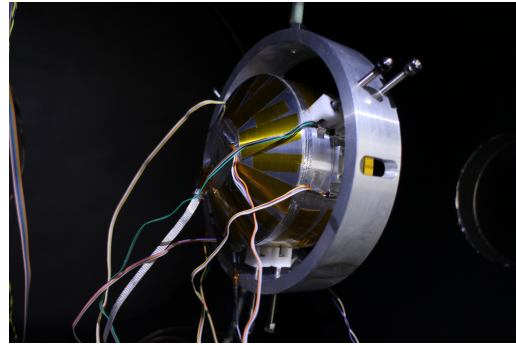
(b) *Rear view.*

(c) *Upper view.*
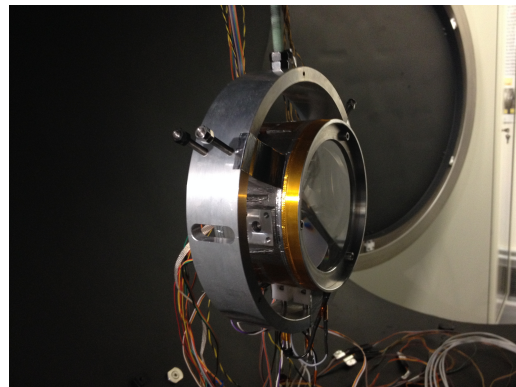
(d) *Side view.*

Figure 5.2: MoonLIGHT-2 inside the SCF-G chamber ready for the tests

Thermal test and analysis procedure

During the first SCF-Test campaign for both SUN ON and SUN OFF, we acquired 1 IR picture every minute for the first 30 minutes and 1 IR picture every 5 minutes for the remaining minutes. For the second and third campaign, for each phase, we acquired 1 IR picture every 2 minutes in order to increase the data used for the analysis. The IR analysis is achieved with FLIR Thermacam Researcher SW and a specific Matlab code (for hardware description see section 4.3).

The first step for the thermal analysis is to acquire the temperature distributions of the entire visible MoonLIGHT-2 front face (after the IR image calibration). This part of work is carried out using the FLIR Thermacam Researcher SW and in figure 5.3a it is possible to see a screenshot of the program. In this way I can extract the average temperature within this area w.r.t. test time. After obtaining the data I used a custom Matlab code, that I developed during this PhD thesis, to analyze the data and compute the best fit parameters searching the minimum of the χ^2 function on degrees of freedom, where:

- the experimental data are the observed values.

- the pure exponential function described in equation 5.1 is the expected function.

$$T(t) = T_0 \pm \Delta T(1 - e^{\frac{-t}{\tau_{ccr}}}) \tag{5.1}$$

with:
- T(t) is the temperature at time t.
- T_0 is the temperature at t=0.
- ΔT is the difference between the final temperature and T_0.
- τ_{CCR} is the CCR thermal constant, or the time spent by reflector to reach 2/3 of its plateau temperature, that means the thermal equilibrium with the environment. It is a function of temperature and other environmental conditions experienced by LRA on the spacecraft.

- The χ^2 function is defined with three degrees of freedom: T_0, ΔT and τ_{CCR}.

The Matlab code searches the τ_{CCR} that minimizes the χ^2 function setting as initial values for T_0, ΔT the experimental data. Then the code repeats the computation 250 times with a bootstrap cycle ([Efron 1982] and [Johnson 2001]) and the average τ_{CCR} with its standard deviation are respectively the τ_{CCR} computed by fit with its error (both values will be printed on the plots).

To investigate in detail the temperature gradient on the CCR front face I carried out a different analysis. I placed eight small areas (3x3 pixels) on the CCR surface picture:

- three located near the tabs (AR01 near the left tab, AR02 near the upper tab, AR03 near the lower tab),

- one in the center (AR04),

- three located near the edges of the CCR face between the tabs (AR05 near the upper edge, AR06 near the right edge, AR07 near the lower edge)

- the last one, AR08, positioned close to the upper tabs, near the AR02. The AR08 has been chosen because the comparison with AR02 could tell us how sensitive the data is slightly offset positions.

All these areas are shown in figure 5.3b.
After the extraction of these raw data, I computed and plotted the difference between the average temperatures of each area and the central area AR04.

The camera systematic error is ±2.0K, however in order to obtain a more realistic statistical error I conducted a specific study: I waited the plateau condition with MoonLIGHT-2 inside the chamber and then I acquired the mean value of the CCR front face for 2 h computing then the standard deviation from the mean; the value obtained is ±0.5K. Assuming that in plateau condition the payload front face temperature is constant (and so independent from the calibration), I can consider this value as a pure statistical error. Following this study for each point in every thermal plots I consider ±0.5K as error bar. However this error bar will not be
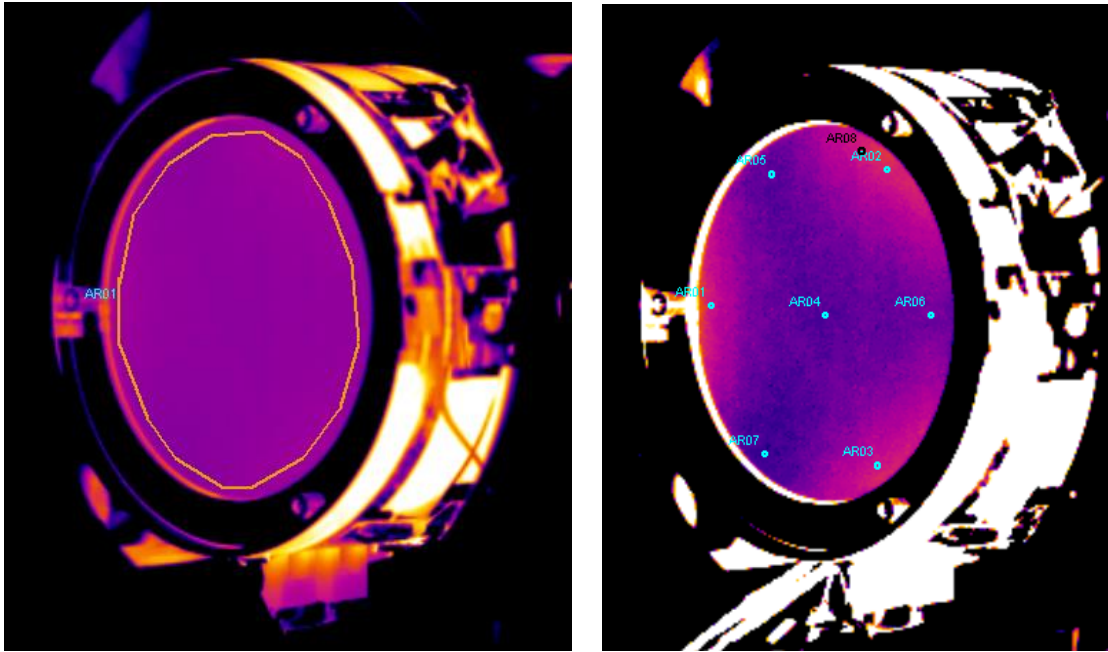
(a) *Sample of MoonLIGHT IR picture with in evidence the area used for the analysis .*

(b) *IR image of MoonLIGHT for the analysis with eight areas.*

Figure 5.3: MoonLIGHT-2 IR analysis example for front face average temperature value and front face temperature gradient

displayed in the gradients plots in order to simplify the plot reading.

The main plots tests results (τ_{CCR}, χ^2_{FIT} and ΔT analysis) will be reported in the following section, while the overall thermal results will be discussed in section 5.1.4. This activity is the experimental part of my thesis since I carried out personally all the analysis.

Optical tests and analysis procedure

While the focus of my thesis experimental part was the thermal analysis, this part of the work was realized by the SCF_Lab members and here will be reported to provide a more complete analysis of the payload, since the thermal and optical payload behaviour are strongly correlated (expecially in the SCF-Test).

Before starting the SUN ON phase, with vacuum pulling and LN2 flowing inside the cryostat, first FFDP, named 000, is acquired; it will serve as a baseline steady-state optical condition. For the rest of the Sun ON phase, no optical interrogation is performed, in order not to affect the thermal stimulation of the assembly. In fact we can not take FFDP during the SUN ON because it would be necessary to rotate the payload in front of the optical window shutting off the solar simulator shutter. This will affect all the SUN ON heating phase that will not be homogeneous anymore, nullifying also the thermal analysis described before.

During the Sun OFF phase, FFDPs are sampled at well-defined cadency. In particular we had four sessions of FFDP acquisition. The first two sessions were 1 hour long each, the remaining two sessions were 120 minutes for the third one and the last until the end of the test. The frequency of FFDP acquisition was 1 FFDP every 2 minutes and 1 FFDP every 4 minutes for the first two sessions respectively, 1 FFDP every 10 minutes for the third session and finally 1 FFDP every 30 minutes until the end of the measurement. This procedure is the same for every SCF-Test campaign.

The final output of the analysis is the average Optical Cross Section (OCS) intensity at velocity aberration of MoonLIGHT-2 CCR FFDP. The maximum error for all the OCS's presented in this document is 15% and it is a measure of the systematic error introduced by all optical components used during test.

5.1.1 1st SCF-Test campaign: Setup and Results

The assembly used for this tests campaign is visible in figure 5.4; from left to right, is composed of:

- Aluminum ring with 3 screws, tightened at 0.5 Nm

- Upper ring (KEL-F).

- MoonLIGHT-2 CCR.

- Lower ring (KEL-F).

- Can Ring (KEL-F, with 3 probes near screw holes).

- Conformal Can (in thermal contact with the housing, using 3 thermal pads, pressed between the can tabs and the housing).

- External Housing with the two resistive heating tapes (four wires) for thermal control installed. The housing is covered with a set of Kapton tapes in order to increase the thermal exchange with the environment (SCF-G shroud). The resistive tape and the Kapton were installed in the same way for all the three test campaigns.
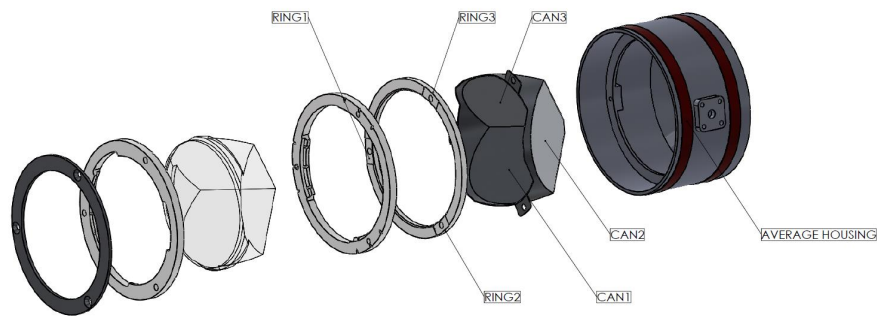
Figure 5.4: MoonLIGHT-2 assembly for the first test campaign with probes position

For this test campaign a total of eleven PT100 probes were installed in the following configuration (see figures 5.4 and 5.5 for the scheme positioning):

- 3 probes on the lower ring (see figure 5.6a and 5.6b).

- 3 probes on the Conformal Can (see figure 5.6c).
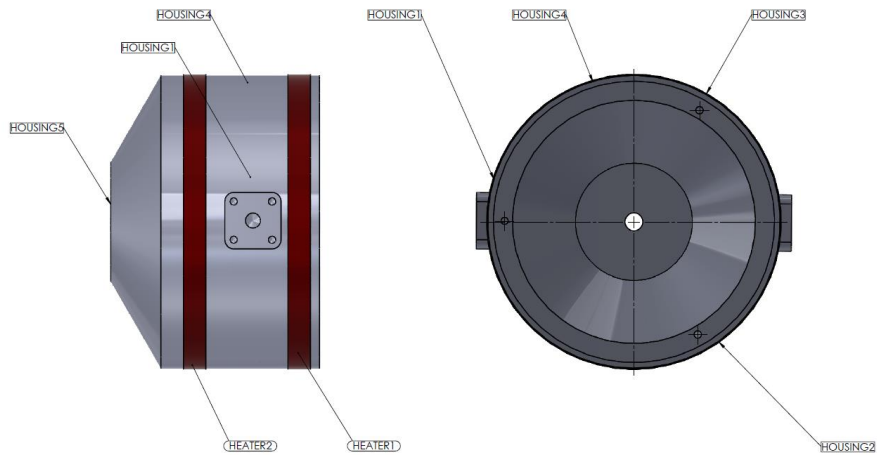
Figure 5.5: MoonLIGHT-2 Housing probes positioning

- 5 probes on the housing (see figure 5.6d) (in thermal plots only the average temperature among them has been shown).

With this configuration we performed 2 different SCF-TEST, both with $t_{ON}=t_{OFF}=$12h:

1. Housing temperature at 300K, sun incidence on front face CCR during SUN ON equal to 0°

2. Housing temperature at 300K, sun incidence on front face CCR during SUN ON equal to 30° (breakthrough condition)

(a) *Installing of 3 probes on the lower ring.*
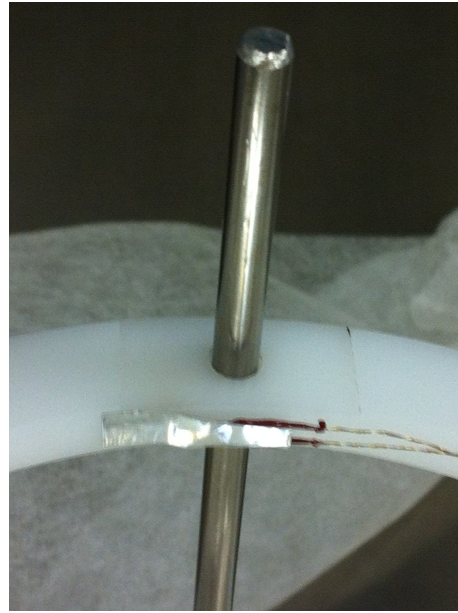
(b) *Installing of 3 probes on the lower ring (side view).*
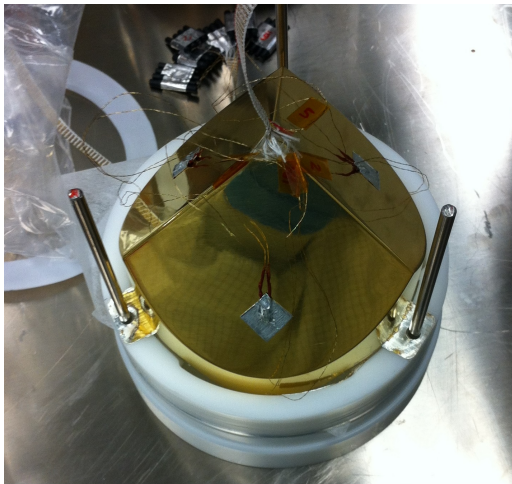
(c) *Installing of 3 probes on the conformal Can.*
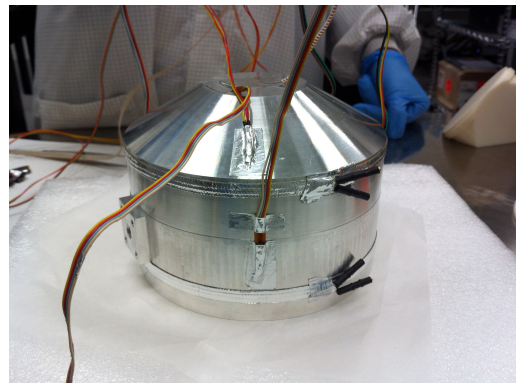
(d) *Installing of 5 probes on the housing.*

Figure 5.6: MoonLIGHT-2 PT100 probes positioning for the first test campaign

Thermal test results

SCF-TEST 300K, sun incidence 0°
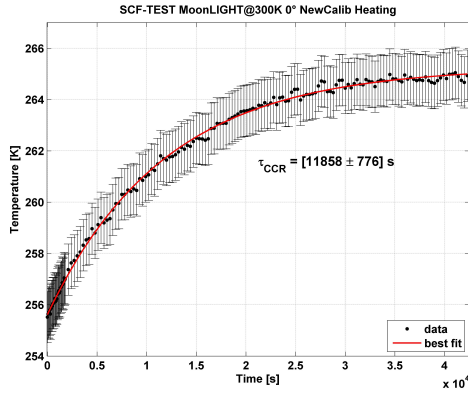
(a) τ_{CCR} *heating phase,*
$\chi^2_{FIT} = 0.02$.
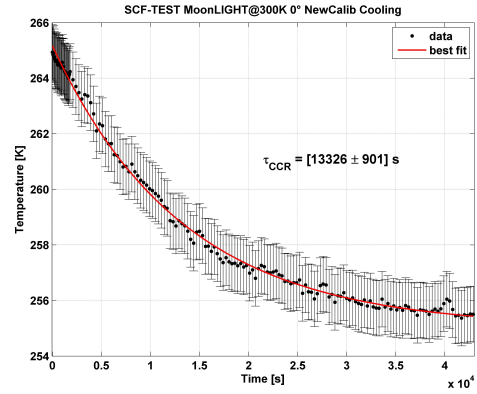
(b) τ_{CCR} *cooling phase*
$\chi^2_{FIT} = 0.04$.
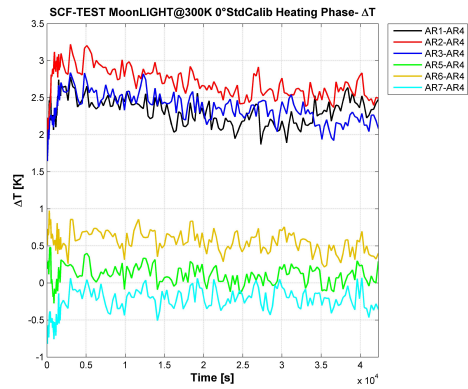
(c) *Front face gradient heating phase.*
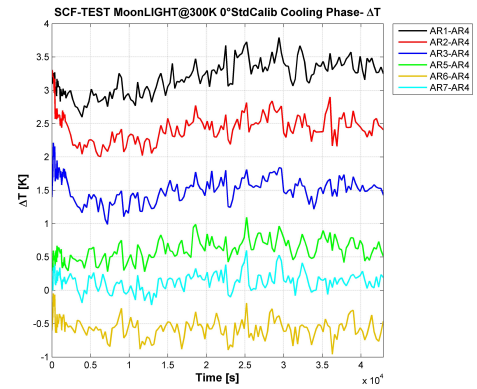
(d) *Front face gradient cooling phase.*

Figure 5.7: MoonLIGHT-2 SCF-Test at 300K, sun incidence 0°, IR analysis result. First test campaign.

SCF-TEST 300K, sun incidence 30°
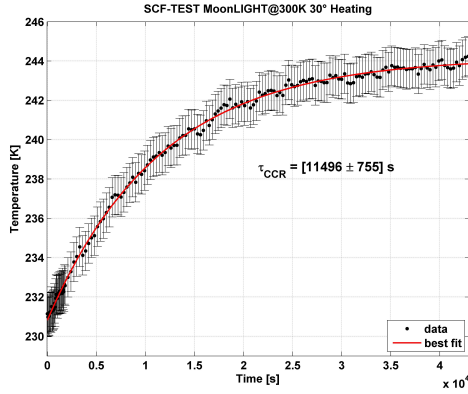
(a) τ_{CCR} *heating phase,*
$\chi^2_{FIT} = 0.08$.
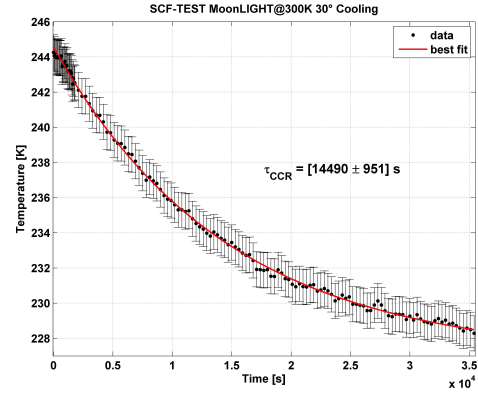
(b) τ_{CCR} *cooling phase,*
$\chi^2_{FIT} = 0.12$.
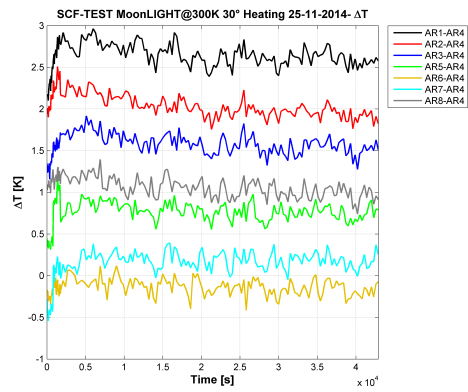
(c) *Front face gradient heating phase.*
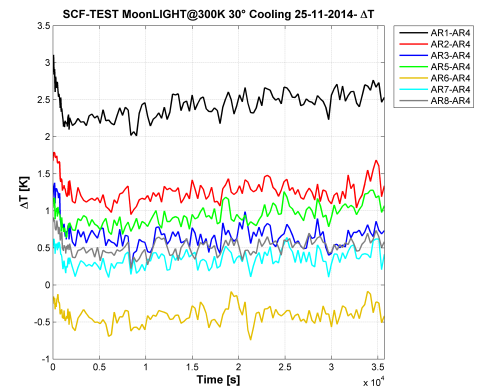
(d) *Front face gradient cooling phase.*

Figure 5.8: MoonLIGHT-2 SCF-Test at 300K, sun incidence 30°, IR analysis result. First test campaign.

Optical test results
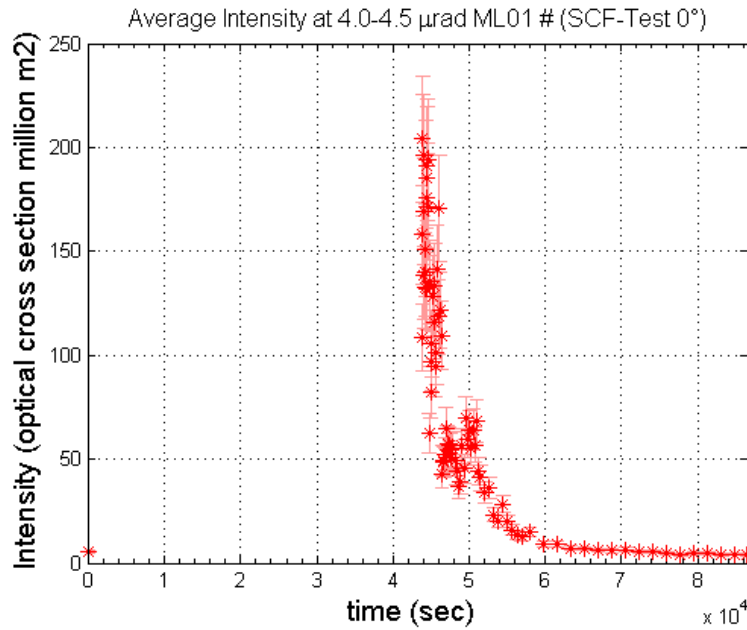
SCF-TEST 300K, sun incidence 0°

(a) Average intensity vs time at range 4.0-4.5 μrad during the SCF-Test.
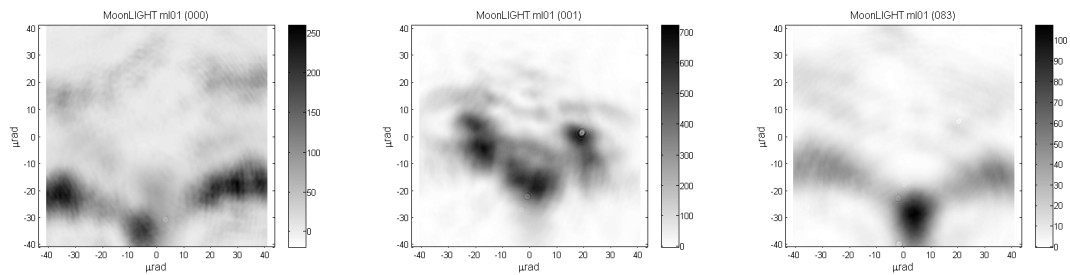
(b) *First FFDP, beginning of test.* **(c)** *Second FFDP, beginning of SUN OFF.* **(d)** *Last FFDP, end of test.*

Figure 5.9: MoonLIGHT-2 SCF-Test at 300K, sun incidence 0°, Optical analysis result. First test campaign.

SCF-TEST 300K, sun incidence 30°
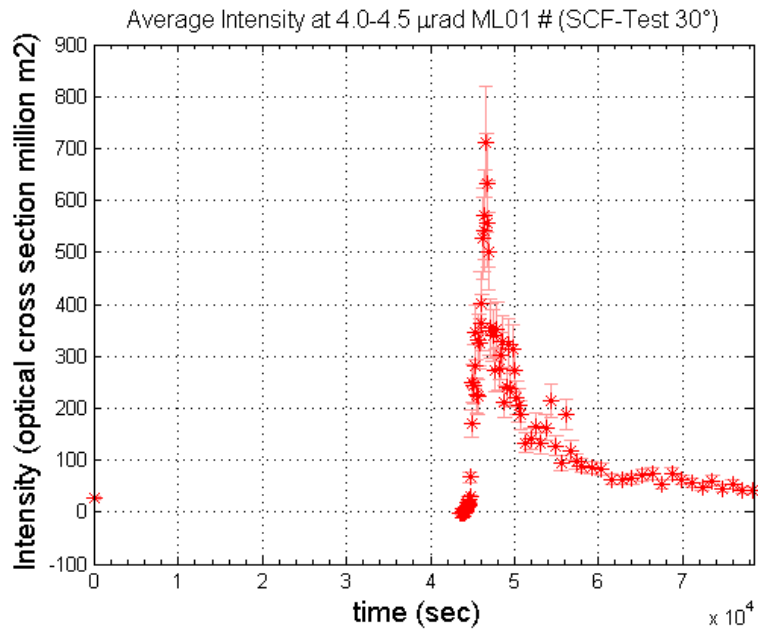
(a) Average intensity vs time at range 4.0-4.5 μrad during the SCF-Test.
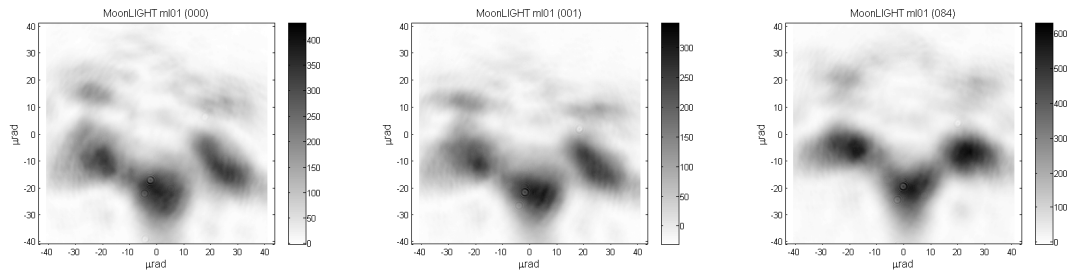
(b) *First FFDP, beginning of test.*   **(c)** *Second FFDP, beginning of SUN OFF.*   **(d)** *Last FFDP, end of test.*

Figure 5.10: MoonLIGHT-2 SCF-Test at 300K, sun incidence 30°, Optical analysis result. First test campaign.

80

5.1.2 2nd SCF-Test campaign: Setup and Results

With respect to the first test campaign, we added copper tape on the three triangular areas below the tabs and on the cylindrical surface of the tabs (figure 5.12) in order to reduce the thermal conductivity between the CCR and its assembly. The remaining assembly structure is the same but we modified the probes position using the scheme in figure 5.11 (refer always to figure 5.5 for housing probe positioning that does not change for the tests of this campaign). In this second configuration we have always eleven probes but now distributed in this way:

- 5 probes on the conformal Can (figure 5.13a)

- 1 probe on the lower KEL-F ring (figure 5.13b)

- 5 probes on the housing (just as in first test campaign, figure 5.6d)

With this configuration we performed 3 different SCF-TESTs, all with t_{ON}=14 h = t_{OFF}=14 h (now we have increased the test time in order to reach a better steady condition after the SUN ON/OFF):

1. Housing temperature at 250K, sun incidence on front face CCR during SUN ON equal to 0°;

2. Housing temperature at 300K, sun incidence on front face CCR during SUN ON equal to 0°;

3. Housing temperature at 330K, sun incidence on front face CCR during SUN ON equal to 0°;
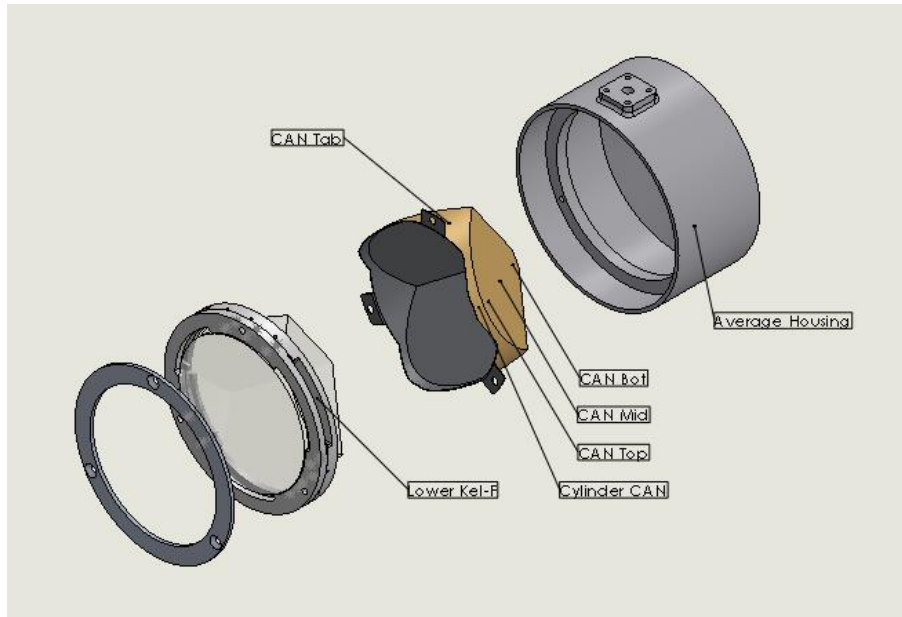
Figure 5.11: MoonLIGHT-2 assembly for the second test campaign with probes position
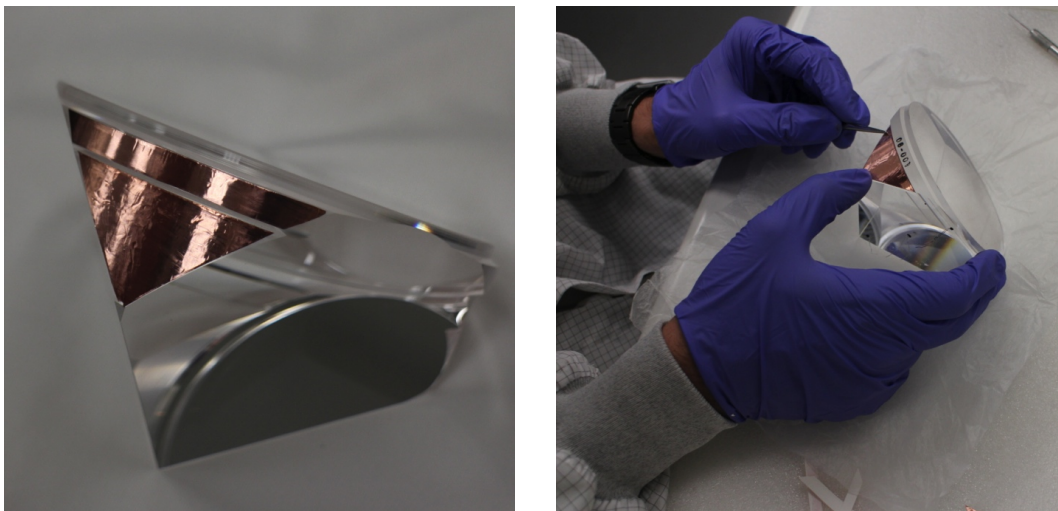
Figure 5.12: MoonLIGHT-2 copper tape placement for the second test campaign
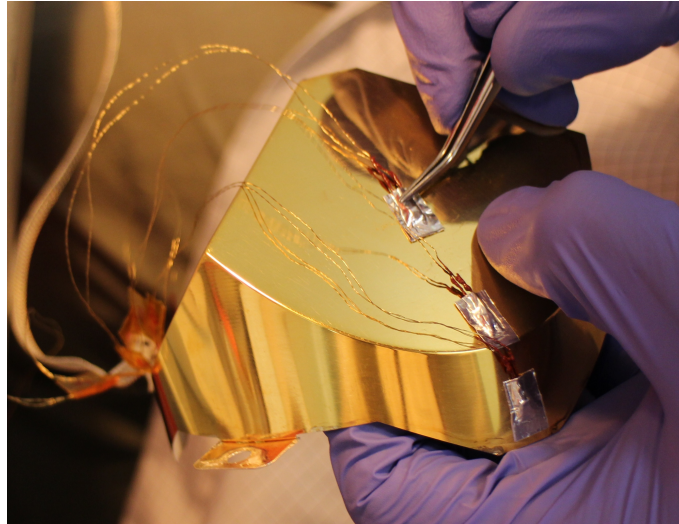
(a) *Installing of 5 probes on the conformal can.*
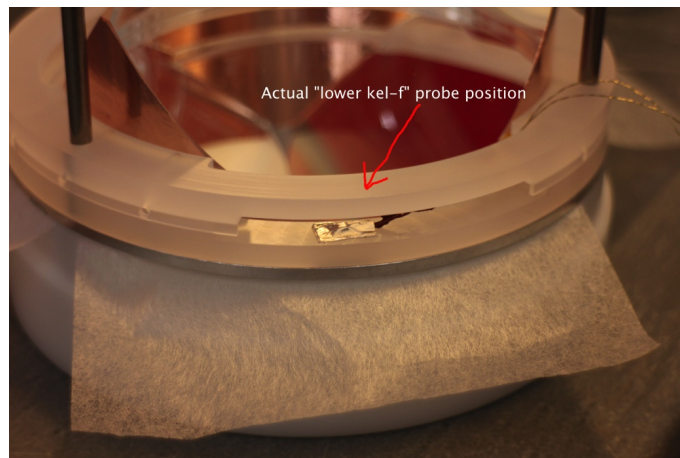
(b) *Installing of 1 probe on the kel-f ring.*

Figure 5.13: MoonLIGHT-2 PT100 probes positioning for the second test campaign

Thermal test results

SCF-TEST 250K, sun incidence 0°

(a) τ_{CCR} *heating phase,* $\chi^2_{FIT} = 0.04$.
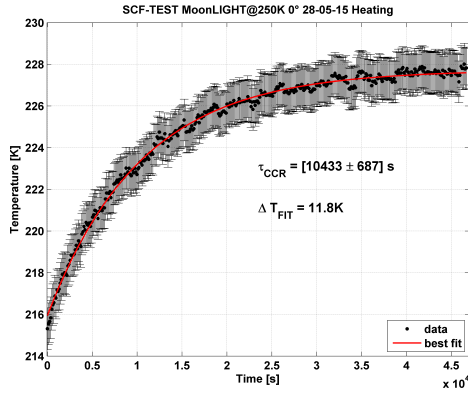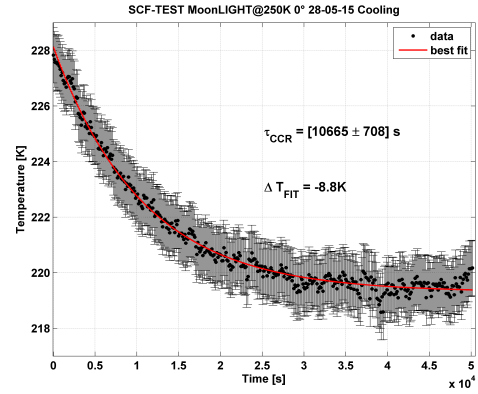
(b) τ_{CCR} *cooling phase,* $\chi^2_{FIT} = 0.06$.
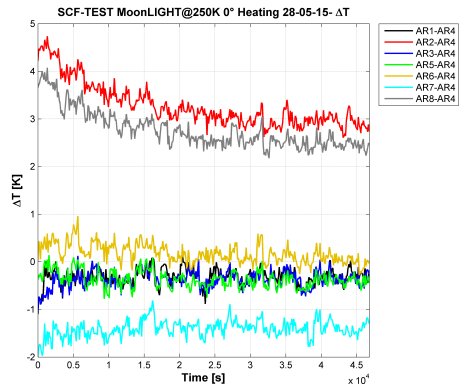
(c) *Front face gradient heating phase.*
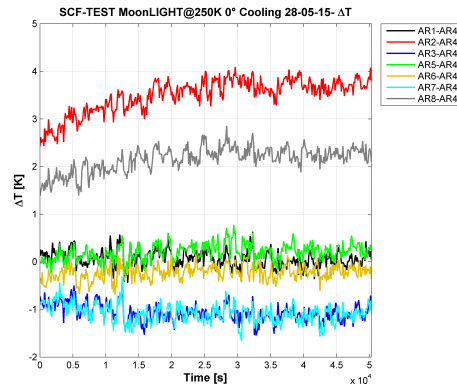
(d) *Front face gradient cooling phase.*

Figure 5.14: MoonLIGHT-2 SCF-Test at 250K, sun incidence 0°, IR analysis result. Second test campaign.

SCF-TEST 300K, sun incidence 0°

(a) τ_{CCR} *heating phase,* $\chi^2_{FIT} = 0.03.$
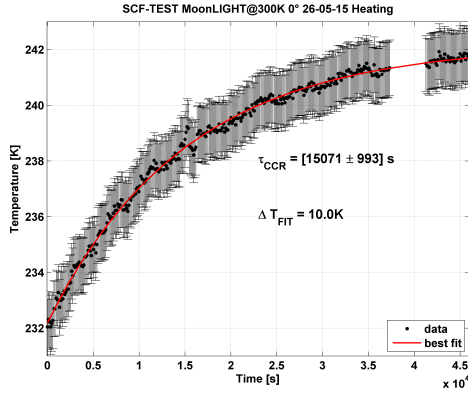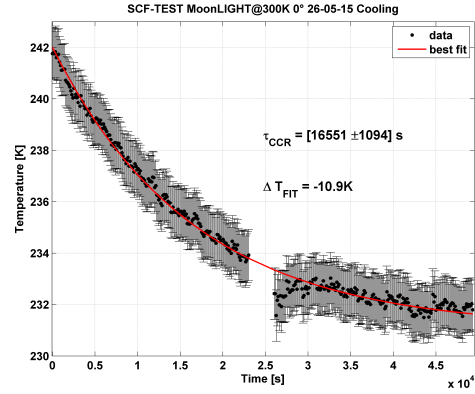
(b) τ_{CCR} *cooling phase,* $\chi^2_{FIT} = 0.08.$
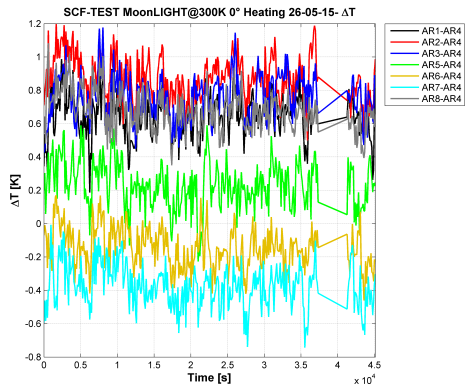
(c) *Front face gradient heating phase.*
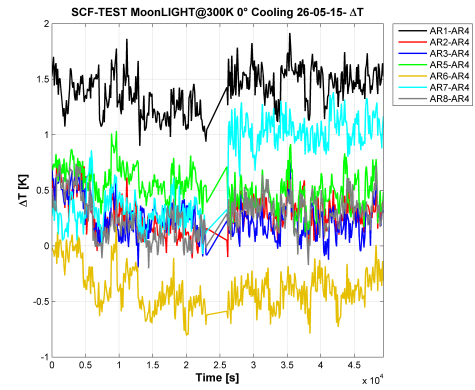
(d) *Front face gradient cooling phase.*

Figure 5.15: MoonLIGHT-2 SCF-Test at 300K, sun incidence 0°, IR analysis result. Second test campaign. Due to a technical issue at the IR camera we lost some data at the end of the SUN ON phase and at the middle of the SUN OFF phase. However goodness of the analysis is not affected by this loss thanks to the significative number of data collected.

SCF-TEST 330K, sun incidence 0°
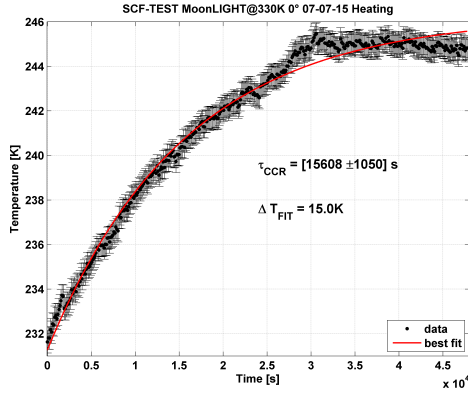
(a) τ_{CCR} *heating phase,*
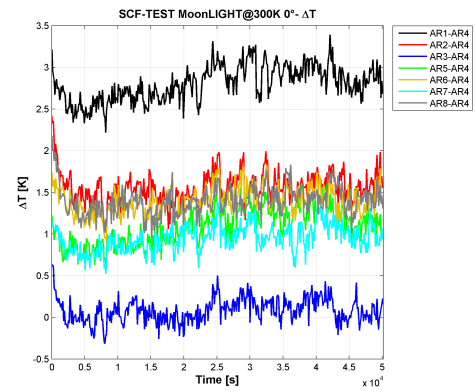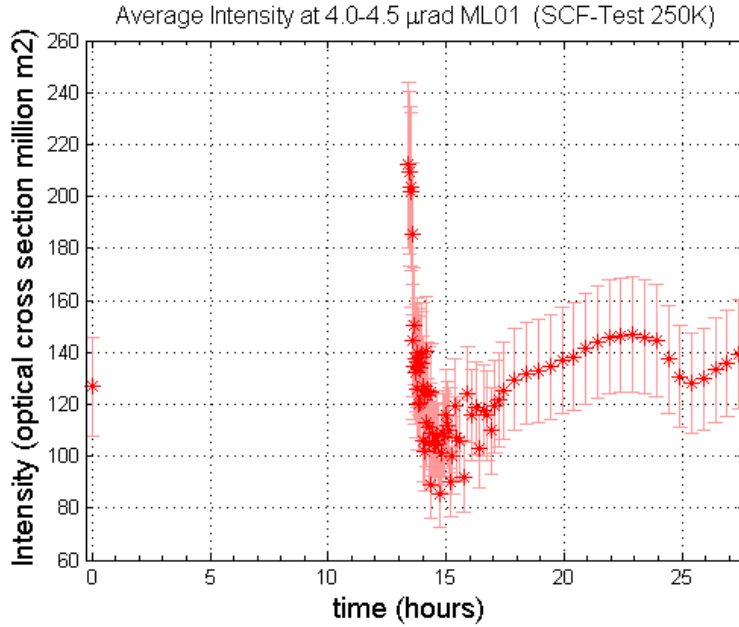$\chi^2_{FIT} = 0.70.$
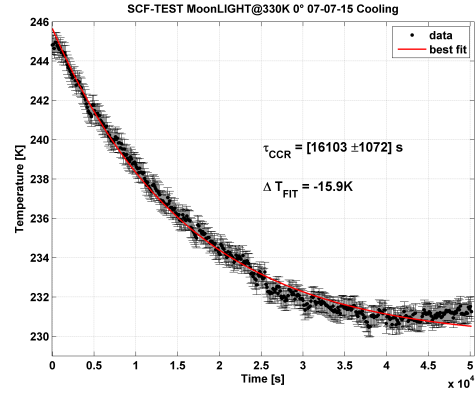
(b) τ_{CCR} *cooling phase,*
$\chi^2_{FIT} = 0.51.$
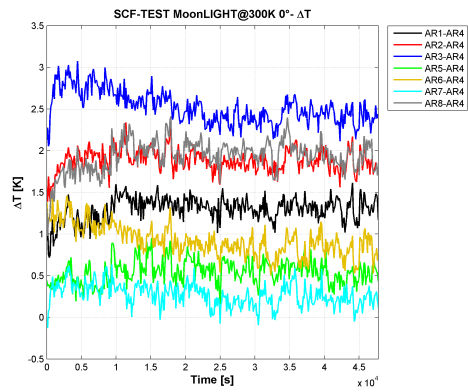
(c) *Front face gradient heating phase.*

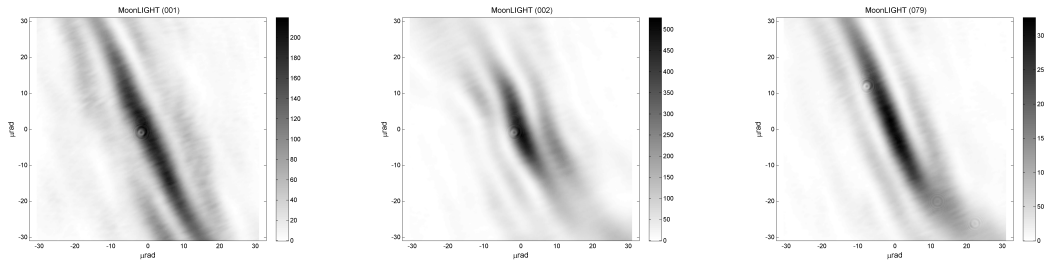**(d)** *Front face gradient cooling phase.*

Figure 5.16: MoonLIGHT-2 SCF-Test at 330K, sun incidence 0°, IR analysis result. Second test campaign.

Optical test results

SCF-TEST 250K, sun incidence 0°

(a) Average intensity vs time at range 4.0-4.5 μrad during the SCF-Test.
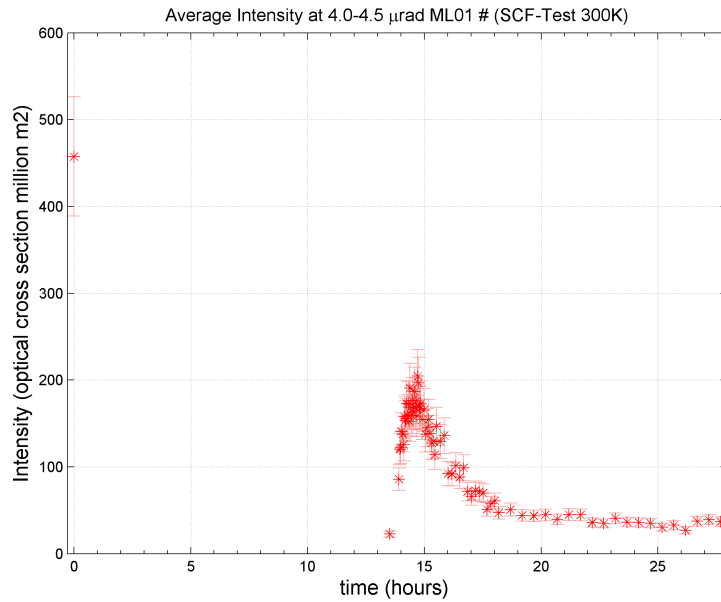

(b) *First FFDP, beginning of test.*

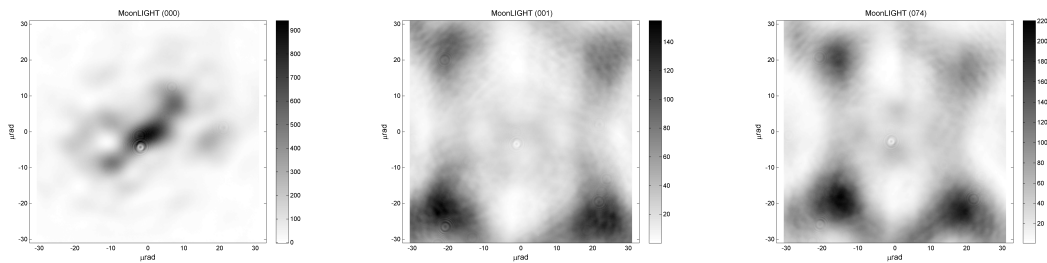**(c)** *Second FFDP, beginning of SUN OFF.*

(d) *Last FFDP, end of test.*

Figure 5.17: MoonLIGHT-2 SCF-Test at 250K, sun incidence 0°, Optical analysis result. Second test campaign.

SCF-TEST 300K, sun incidence 0°

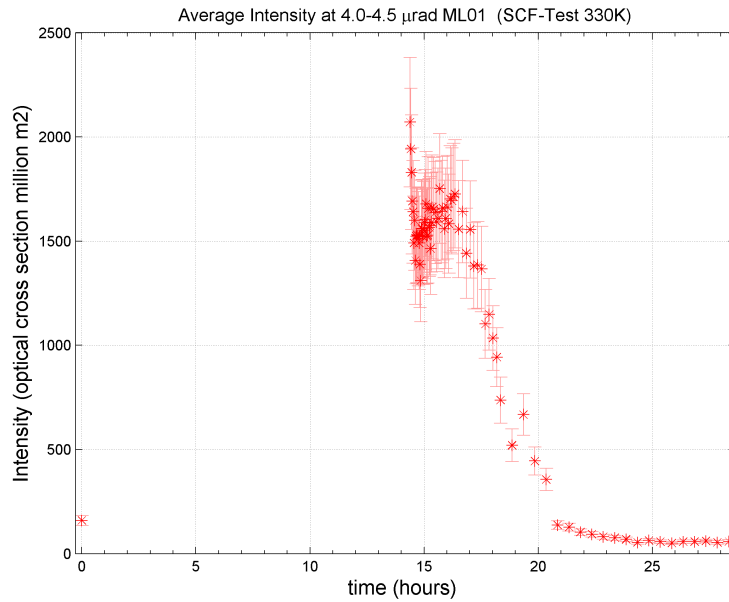**(a)** Average intensity vs time at range 4.0-4.5 μrad during the SCF-Test.

(b) *First FFDP, beginning of test.*
(c) *Second FFDP, beginning of SUN OFF.*
(d) *Last FFDP, end of test.*

Figure 5.18: MoonLIGHT-2 SCF-Test at 300K, sun incidence 0°, Optical analysis result. Second test campaign.

SCF-TEST 330K, sun incidence 0°

(a) Average intensity vs time at range 4.0-4.5 μrad during the SCF-Test.
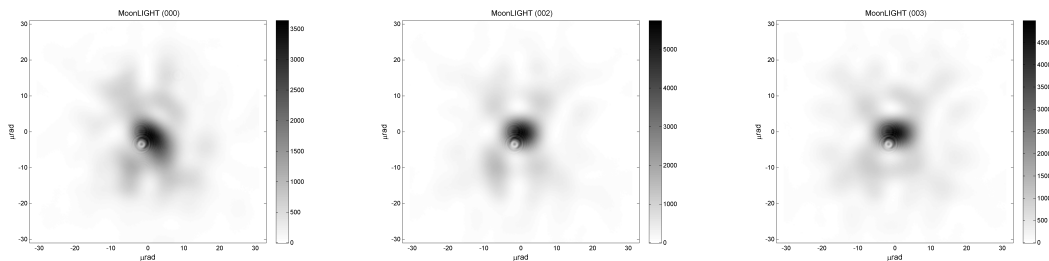

(b) *First FFDP, beginning of test.*

(c) *Second FFDP, beginning of SUN OFF.*

(d) *Last FFDP, end of test.*

Figure 5.19: MoonLIGHT-2 SCF-Test at 330K, sun incidence 0°, Optical analysis result. Second test campaign.

5.1.3 3rd SCF-Test campaign: Setup and Results

With respect to the previous campaign in this one we removed the conformal can in order to reduce the radiative load on the retroreflector and so reduce the thermal gradient on the retroreflector. We used a total of nine PT100 probes installed in this way:

- 2 probes on the internal Housing superface (the one facing the retroreflector);

- 3 probes on the external Housing superface (the one facing the shroud);

- 3 probes on the three CCR edge;
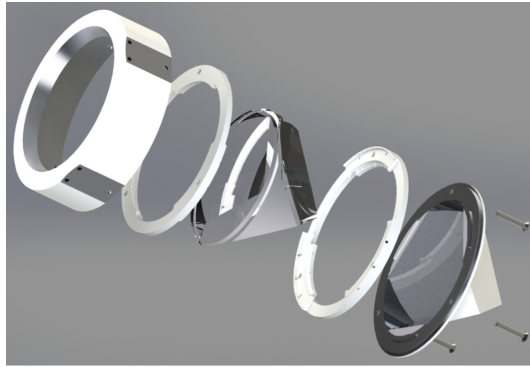
- 1 probe on the KEL-F ring;

Figure 5.20: MoonLIGHT-2 assembly for the third test campaign

With this configuration (reported in figure 5.20) we performed 2 different SCF-TESTs, all with t$_{ON}$=14 h = t$_{OFF}$=14 h.:
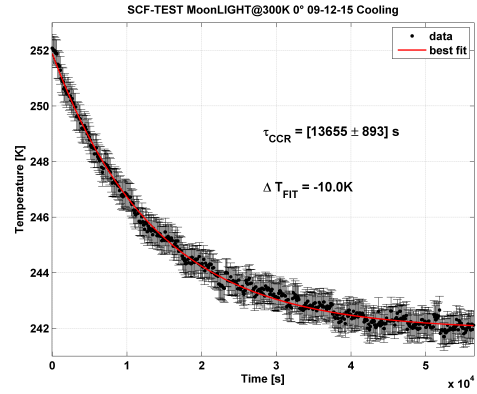
1. Housing temperature at 300K, sun incidence on front face CCR during SUN ON equal to 0°

2. Housing temperature at 300K, sun incidence on front face CCR during SUN ON equal to 30°

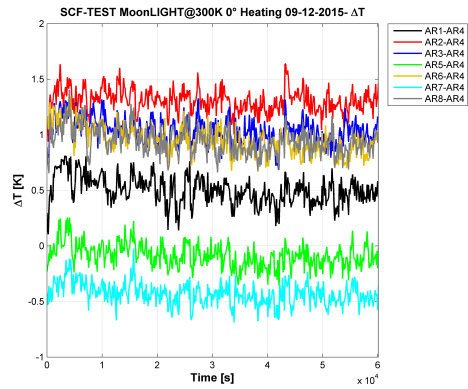**Thermal test results**

SCF-TEST 300K, sun incidence 0°
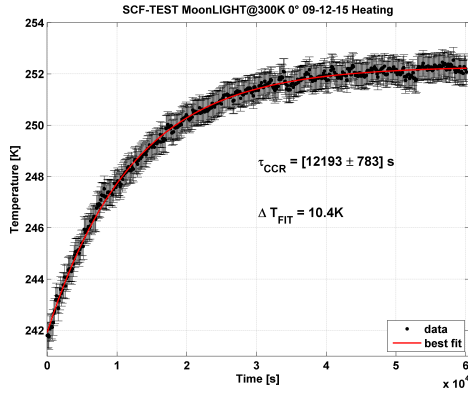
(a) τ_{CCR} *heating phase,* $\chi^2_{FIT} = 0.09$.

(b) τ_{CCR} *cooling phase,* $\chi^2_{FIT} = 0.12$.

(c) *Front face gradient heating phase.*
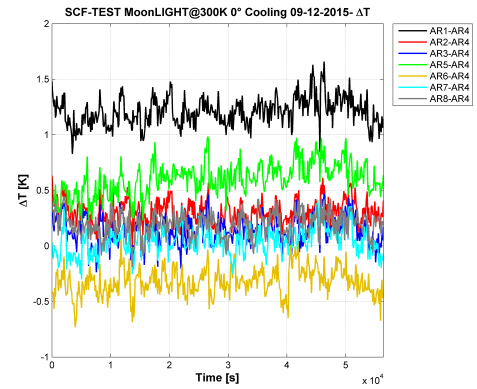
(d) *Front face gradient cooling phase.*

Figure 5.21: MoonLIGHT-2 SCF-Test at 300K, sun incidence 0°, IR analysis result. Third test campaign.

SCF-TEST 300K, sun incidence 30°

(a) τ_{CCR} *heating phase,*
$\chi^2_{FIT} = 0.08.$
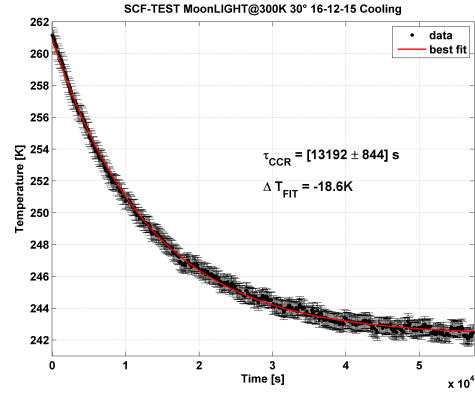
(b) τ_{CCR} *cooling phase,*
$\chi^2_{FIT} = 0.12.$

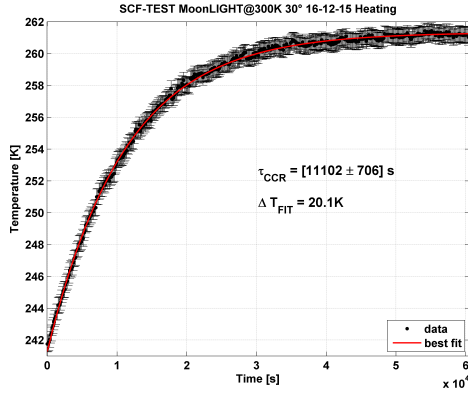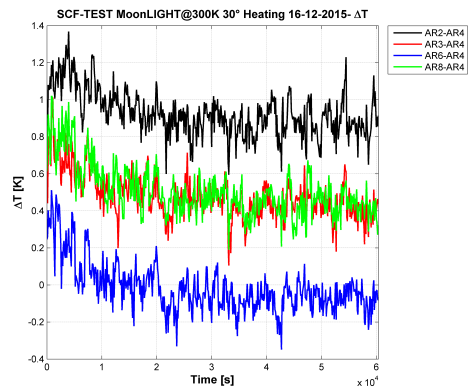**(c)** *Front face gradient heating phase.*
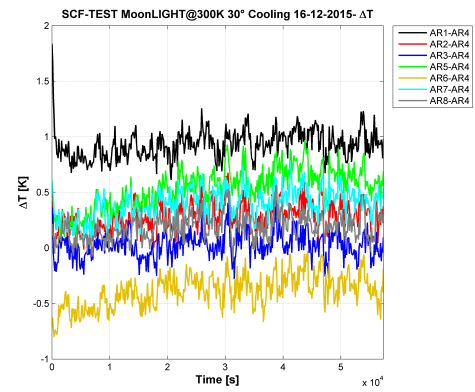
(d) *Front face gradient cooling phase.*

Figure 5.22: MoonLIGHT-2 SCF-Test at 300K, sun incidence 30°, IR analysis result. Third test campaign.

Optical test results
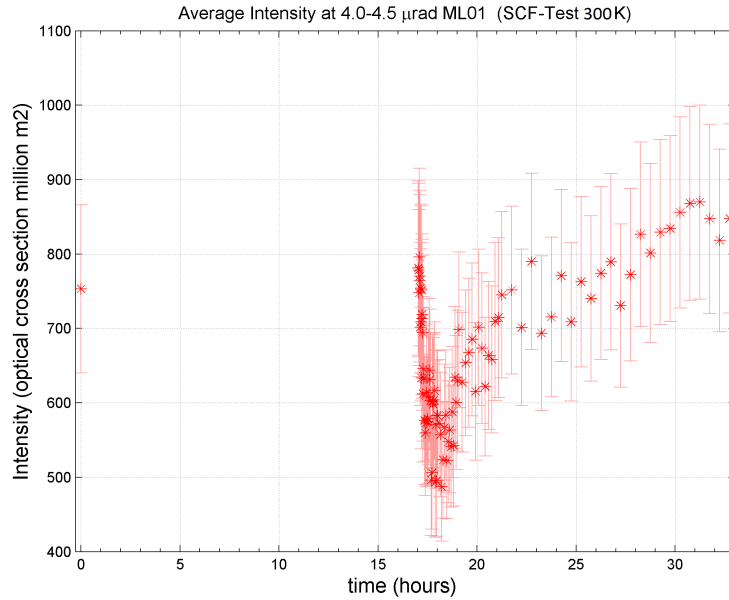
SCF-TEST 300K, sun incidence 0°

(a) Average intensity vs time at range 4.0-4.5 μrad during the SCF-Test.
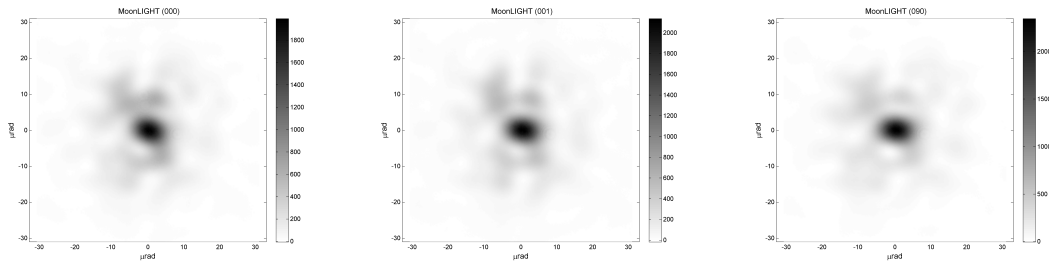
(b) *First FFDP, beginning of test.* **(c)** *Second FFDP, beginning of SUN OFF.* **(d)** *Last FFDP, end of test.*

Figure 5.23: MoonLIGHT-2 SCF-Test at 300K, sun incidence 0°, Optical analysis result. Third test campaign.

SCF-TEST 300K, sun incidence 30°

(a) Average intensity vs time at range 4.0-4.5 μrad during the SCF-Test.

(b) *First FFDP, beginning of test.* **(c)** *Second FFDP, beginning of SUN OFF.* **(d)** *Last FFDP, end of test.*

Figure 5.24: MoonLIGHT-2 SCF-Test at 300K, sun incidence 30°, Optical analysis result. Third test campaign.

5.1.4   SCF-Tests overall conclusions

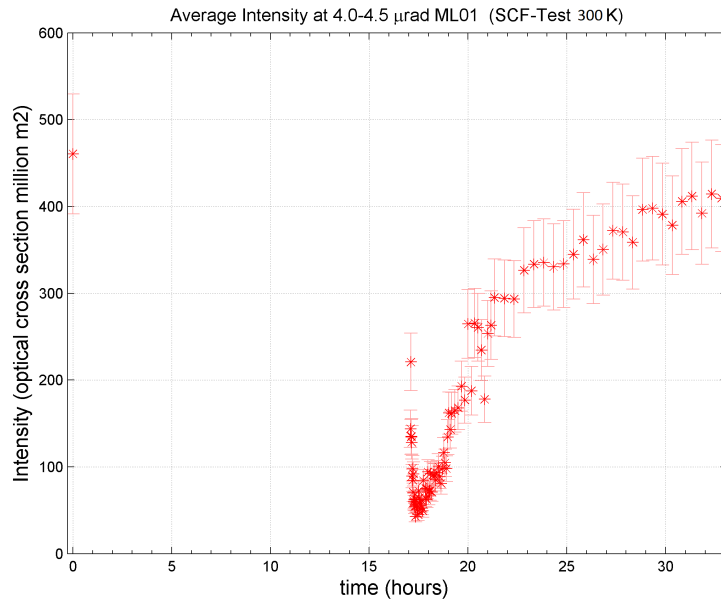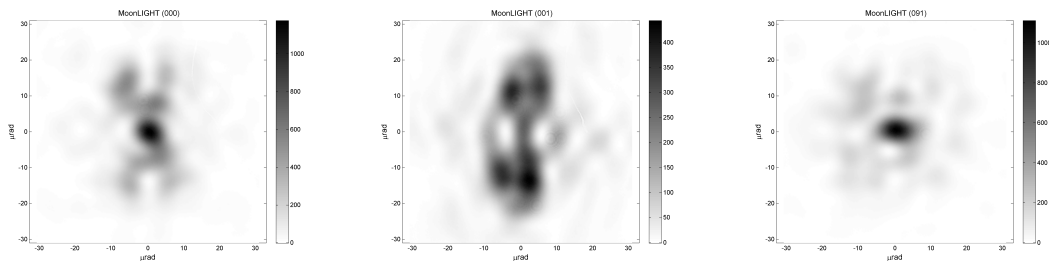All thermal tests results reported in the previous plots are summarized in table 5.1 (looking at the χ^2_{FIT} we have a maximum value of about 0.2, proving the reliability of the fitted data). The average τ_{CCR} between SUN ON and SUN OFF is computed using the average between the two single τ_{CCR} (heating and cooling) weighted with their errors while the error is the standard deviation of the single values.

The τ_{CCR} analysis shows some considerably long values (always around $13.5 \times 10^3 sec$), as expected and in agreement with the thermal simulations described in 3.1.1. Such a long thermal constant will ensure a good thermal isolation between the CCR and the lunar regolith providing a good stability during the 14 h night time. However looking at the first two campaigns the reduction of the housing temperature does not increase the time constant as from theory ($\tau_1/\tau_2 \propto T_2/T_1$, [Degnan 1993]), this result in addiction with the quite large front face temperature gradient (respect to the thermal simulations) suggests the presence of an excessive thermal conductivity between CCR and housing. The effect becomes visible looking at the thermal gradient analysis. These plots in fact show that, as reported in figure 5.3b, there are hot areas near the tab, where the screws hold the CCR to the structure.

For these reasons in order to reduce the thermal gradient (due to the conductivity between housing and retroreflector) after the first test campaign we added the copper tape. In this way the second tests campaign showed a reduced thermal gradient (as comparison between the two tests at 300 K) and a slightly long thermal constant. Finally in the last test campaign we removed the conformal can, removing another source of radiative radiation on the retroreflector. In fact this last tests campaign shows further reduced thermal gradient in good agreement with the simulations.

The optical analysis shows a similar behavior. During the test campaign there was an increase in the optical performances (figures 5.9a, 5.18a, 5.23a) probably due to the corresponding thermal gradient reduction. The tests with 30° inclination (figures 5.10a and figures 5.24a) when compared with the 0° inclination (figures 5.9a and figures 5.23a) show a decrease in the optical response due to the break-

Table 5.1: MoonLIGHT-2, SCF-Test all thermal analysis results. From left to right: test campaign, housing temperature, Sun inclination during the SUN ON phase, τCCR and maximum ΔT

Test Campaign	SCF Test		τCCR [10^3 sec]			Maximum ΔT [K]		
	Housing Temp [K]	SUN Angle [°]	Heating phase	Cooling phase	Average	Heating phase	Cooling phase	Average
1st	300	0	11.9 ± 0.8	13.3 ± 0.9	12.6 ± 1.0	3.6 ± 1.0	3.6 ± 1.0	3.6 ± 1.4
	300	30	11.5 ± 0.7	14.4 ± 0.9	13.2 ± 2.1	5.8 ± 1.0	5.4 ± 1.0	5.6 ± 1.4
2nd	300	0	15.1 ± 1.0	16.5 ± 1.1	15.8 ± 1.0	3.1 ± 1.0	2.9 ± 1.0	3.0 ± 1.4
	250	0	10.4 ± 0.7	10.7 ± 0.7	10.5 ± 0.2	4.7 ± 1.0	4.1 ± 1.0	4.4 ± 1.4
3rd	330	0	15.6 ± 1.1	16.1 ± 1.1	15.9 ± 1.5	3.1 ± 1.0	3.4 ± 1.0	3.3 ± 1.4
	300	0	12.2 ± 0.8	13.6 ± 0.9	13.0 ± 1.2	2.9 ± 1.0	2.8 ± 1.0	2.9 ± 1.4
	300	30	11.1 ± 0.7	13.2 ± 0.8	12.1 ± 1.1	3.3 ± 1.0	2.7 ± 1.0	3.0 ± 1.4

through conditions as expected. In the best configuration (third tests campaign) the CCR FFDP resembles what is expected from optics principles and simulations. The energy is mostly located at the centre of the pattern (5.23b), but it also extends towards the edges, fading out and until the end of the test. Likely due to the thermal stimulation operated during the Sun ON phase, energy has now been spread all over the pattern area (figure 5.23c and figure 5.23d). The spreading of energy due to thermal stimulation also affects the average intensity at operational range (4.0-4.5 μrad) as a function of time, during the SCF-Test and after an initial raise, intensity levels off to about 750 millions square meters.

Summarizing the results show the improvements in the MoonLIGHT-2 optical and thermal behavior during the various tests campaigns. The last one will provide good optical and thermal response during the lunar night in agreement with the simulations, as shown by the longer τ_{CCR} and the reduced thermal gradient. Looking at the simulations reported in 3.1.2 we can see that we can obtain good GR results improvement using the payload even during the lunar night alone. However further analysis and design improvements will be done in order to ensure the operatively phase not only during lunar night but also during lunar day time (without Sunshade), if possible, increasing the data collected using the payload once deployed on the Moon. For a complete discussion about GR simulations and the expected improvements using a realistic MoonLIGHT-2 configuration see Chapter 6)

5.2 INRRI flight qualification tests

As described in Chapter 3.2, the INRRI retroreflectors are glued to an aluminum chassis using a silicon rubber suitable for space applications, with a procedure inherited from CHAMP (CHAllenging Minisatellite Payload) [1] CCR bonding. However this bonding process was not qualified for an interplanetary Martian mission, but only Low Earth Orbit (LEO) operations. In addition INRRI has much smaller retroreflectors and a miniaturized geometry compared to CHAMP. For these reasons ESA required a full test campaign on the Proto Flight Model (PFM). The qualification campaign consisted of the tests sequence:

- quasi-static load: peel test on each CCR.

- TVT.

- vibration test: sine and random environment; pyroshock test.

All tests were performed in the SCF_Lab with the exception of the vibration tests, carried out at SERMS (with supervision of some SCF_Lab team members), which owns vibrating tables formally certified for space characterizations.

After successful completion of the space qualification tests (see sections 5.2.1 and 5.2.2 for descriptions and results), INRRI-EDM/2016 was integrated on board of ExoMars-EDM on 14th October 2015, then on 14th March 2016 from Baikonur, Kazakhstan at 09:31 GMT, after successful mission launch on a Proton-M rocket began its flight on Mars(figure 5.25). However on 19th October 2016 the ExoMars-EDM lander failed the landing on Mars surface, at present the status of all instruments (along with INRRI) is still to be defined.

5.2.1 Thermal-vacuum tests and peel test

The TVT was performed on the payload itself, for this reason ESA required the completion of 4 temperature cycles. As part of my PhD thesis I was in charge of

---

[1]for reference: http://op.gfz-potsdam.de/champ/
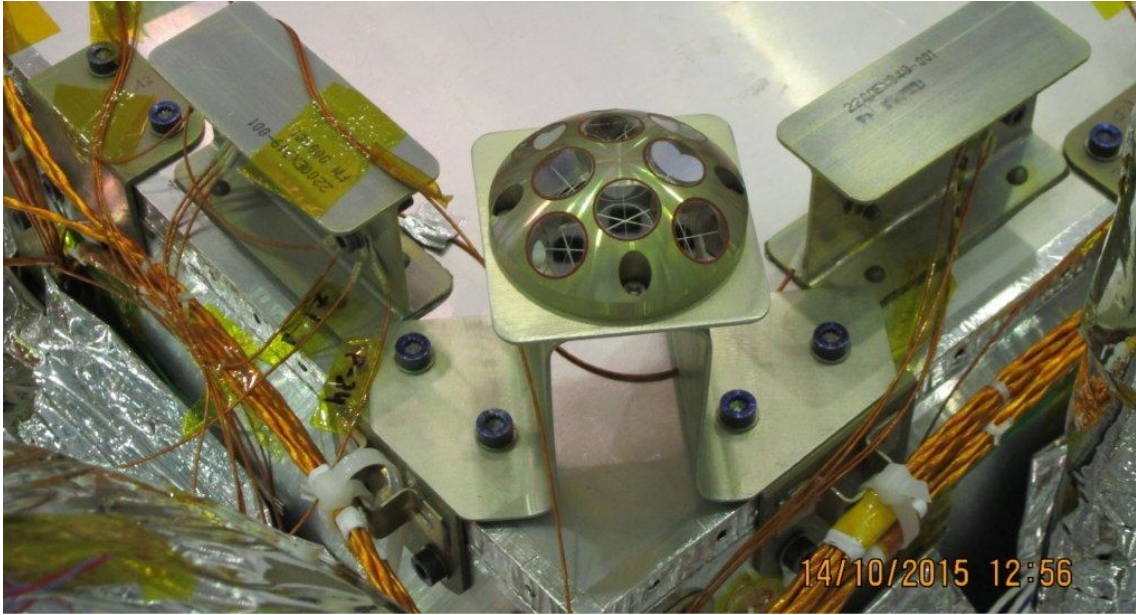
Figure 5.25: INRRI integrated on ExoMars-EDM.

the experimental test setup, ad-hoc software development and data analysis with the support of the SCF_Lab team.

Cycle characteristics were:

- minimum/maximum temperature = 158/328 K

- dwell time = 2 hrs (at 158/328 K)

- pressure less then $5 \times 10^{-6} mbar$ for the whole test.

The payload thermal control was obtained using a single one wire heater tape combined with a direct thermal contact between payload and cryostat inner shield (trough an ad-hoc interface plate), in order to ensure the INRRI cooling. As temperature feedback two cryogenics CP100 temperature probes were installed on INRRI aluminium frame. The probes accuracy in the test range has $\pm 0.2K$ as maximum

value [2] , and this is the value assumed in the plots (however for the sake of the plot clearness the error bar will not be shown). The probes positions were chosen in order to crosscheck for any eventual radiative bias originated by LN2 fluxing into the cryostat inner shield. For this reason one probe was shielded by a MLI cover in order to eventually quantify such a bias (figure 5.26). However, the temperature plot (figure 5.27) showed that the two payload probes read the same temperature, within $\pm 0.6K$ on average for the whole test, lasted about 33 hours. At the end of the test, after a visual inspection, no major damages were identified.

Also before and after the test a mass check was performed in order to verify possible variation during the thermal cycles, due to outgassing either from the silicon rubber bonding or the surface coating. However the as-built INRRI mass was 25.0 g and remained constant throughout the space qualification campaign demonstrating no degradation.

In addition, on the face of each retroreflector was put a mass in order to simulate excess of the EDM quasi-static load, in this way I can check if the silicon rubber can endure such a mechanical stress. A standard peel test (determining the ultimate load) cannot be performed on the payload, so the test aimed at determining variations in elastic properties of the bonding before and after TVT and dynamic tests. An optical level, properly targeted, was used to determine dips w.r.t. retroreflectors rest position as a result of progressive, increasing mass loads. All the temporary dips, due to the mass loads, were reversible and smaller than 100 μm (figure 5.28) with a total gravity acceleration on each retroreflector of $100G$.

---

[2]for reference:

CP100 probes: http://www.cryocon.com/PTsensors/CPGPXP100ds.pdf

RTD standards: http://http://gilsoneng.com/reference/rtdinfo.pdf
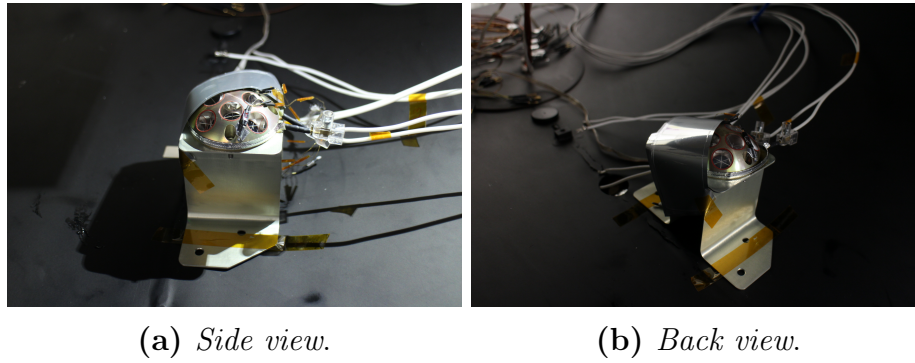
(a) *Side view.*   **(b)** *Back view.*

Figure 5.26: INRRI setup for the TVT test.
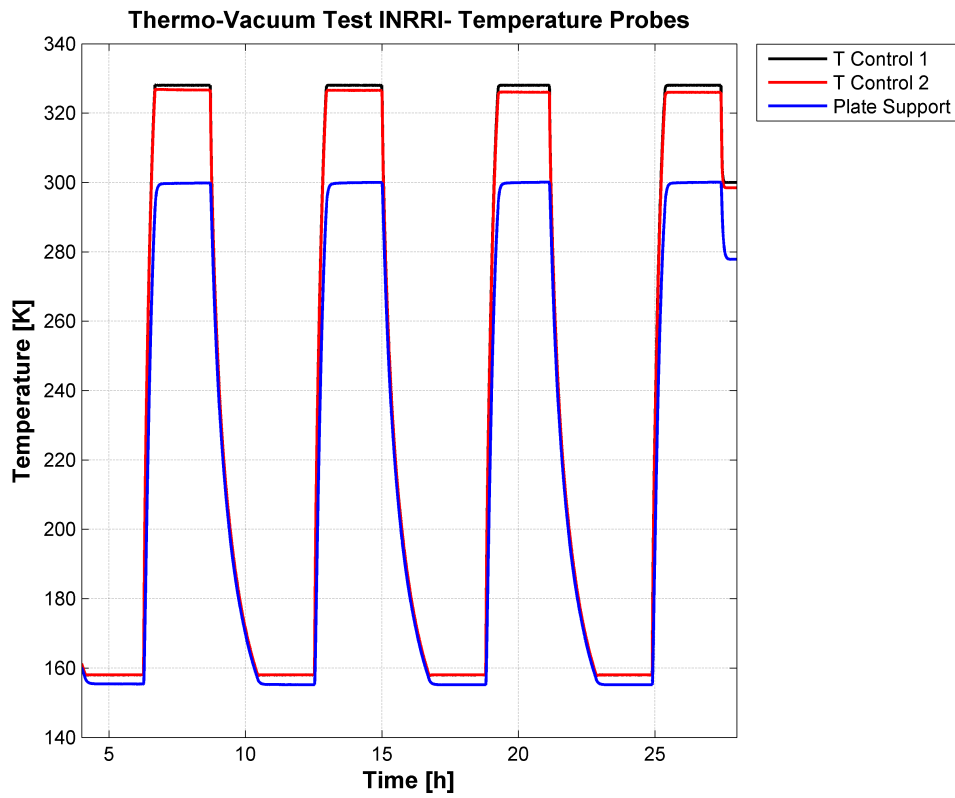
Figure 5.27: INRRI TVT test temperature probes results (temperature accuracy ± 0.2).
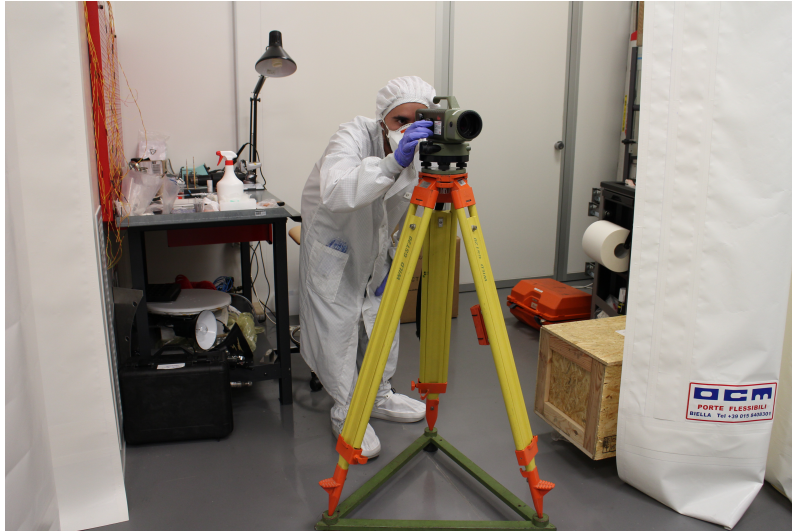
(a) Optical level used for determination of retroreflectors rest positions.

(b) Typical setup for quasi-static load and peel test.

Figure 5.28: INRRI peel test.

5.2.2 Vibration tests

The vibration test is composed by: dynamic load (random and sinusoidal vibrations) and pyroshock test. During the sine environment INRRI was shaken along the three axes according to sinusoidal vibrations. The shocking frequencies and amplitudes were defined by ESA requirements for the corresponding mission launcher. The test goal was to define the robustness of a material and/or a mounting system and the pass/fail criteria were determined by checking the resonance frequencies shifts of the sample after the sine vibration, w.r.t. the resonance frequencies before shaking. If resonances change, either the mass distribution or the characteristic dimensions have changed, test is failed. INRRI, on its flight mounting bracket, passed such a test.
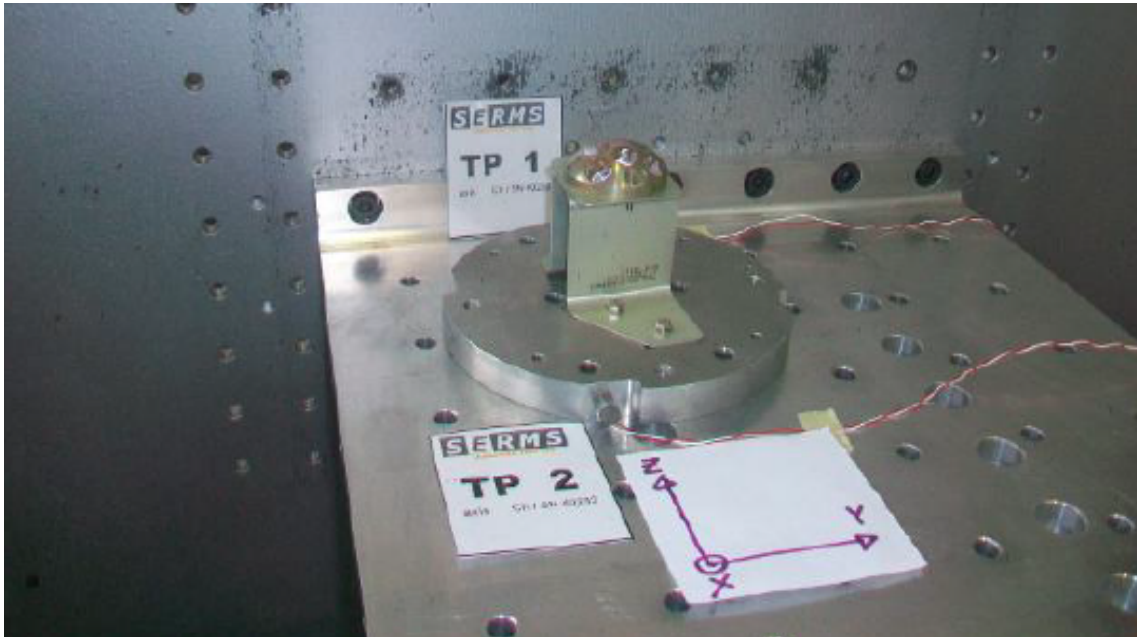

Figure 5.29: INRRI setup for vibration tests at SERMS.

For the random environment the payload was shaken along the three axes according to a random vibration pattern. Even this time the limit characteristic was defined by ESA requirements for the corresponding mission profile. The test repro-

duces the vibrations occurring on launchers, aircrafts, ships, trucks and the pass/fail criteria are the same as for the sine case. Even now, INRRI, on its flight mounting bracket, passed such a test.

Pyroshock test is meant to reproduce the sudden solicitations occurring on a payload during rocket stage separations ([Filippi 1999]). Power spectrum characteristics are still defined by ESA according to the corresponding mission profile. In this case the pass/fail criteria consist of the close inspection of the sample under test after each of the shocks (one per axis), in order to check for the presence of any physical damage either on the payload or the mounting system. INRRI on its flight mounting bracket passed such a test.

All the tests described in this section were not part of my PhD activity, however was reported here in order to provide a complete review of INRRI acceptance tests.

Chapter 6

LLR data analysis and GR
sensitivity studies

In this final Chapter I will describe the GR sensitivity studies carried out with PEP
to characterize the expected improvements with MoonLIGHT-2 and INRRI after
their deployment. First I will describe the PEP software in section 6.1 providing
some information on its computation in 6.2, then in section 6.3, I will describe the
MoonLIGHT-2 sensitivity studies and the conclusions in section 6.3.4. Similarly in
section 6.4 will be discussed the INRRI simulations and the conclusions in section
6.4.1.

6.1 The Planetary Ephemeris Program (PEP)

In order to analyze real or dummy LLR data, I have used the PEP software, devel-
oped at CfA, by I. Shapiro et al. starting from 1970s.
PEP was designed not only to generate ephemerides of the Planets and the Moon,
but also to compare the model with observations. PEP software has enabled con-
straints on departures from standard physics. For example, it has been used to place
limits on the PPN parameters β and γ, geodetic precession and the variation of the
gravitational constant, $\frac{\dot{G}}{G}$ ([Battat 2008], [Reasenberg 1979], [Chandler 1996]).

The first use of this software package was the measurement of the lunar geodetic precession ([Shapiro 1988]). PEP can handle a diverse set of observations, like LLR, radar and doppler ranging, and optical positional measurements, etc. Since the main topic of this work is focused on LLR observations, I will describe the components of a round-trip range prediction, though most of the steps along the way are common to other observable as well.

The capabilities used by PEP to compute the range observable at some epoch can be summarized as:

- determine the positions and velocities of the centers of mass of the Sun, planets, Pluto, and Earth-Moon barycenter by integrating their equations of motion;

- solve the equations of motion for the Moon, Moon rotation and Earth (but not Earth rotation);

- determine the asteroid positions from an elliptic approximation (rather than from integrated equations of motion);

- calculate the displacement of the lunar reflector with respect to the center of mass of the Moon;

- calculate the displacement of the ranging station with respect to the center of mass of the Earth;

- treat photon propagation effects;

- find a constant bias term for any specified span of data;

As already said above, since we are interested in LLR observations, the software is able to calculate the O-C residuals of the distances between observed (O's) and computed (C's) LLR data, derived from expectations of GR and of terrestrial and lunar Geodesy. I performed a very preliminary sensitivity study of LLR data using three stations: McDonald Observatory in Texas (USA), Grasse in France and APOLLO in New Mexico (USA). The APOLLO station provides the best LLR data since 2006. From 2010, the MLRO station in Italy, started to record data from

Apollo 15 array and nowadays is one of the few stations that are able to do LLR measurements.

In Figure 6.1 [1] it is possible to see photon-by-photon data, taken from APOLLO station on November 19, 2007, used to form a single "normal point" of the Apollo 15 array. A so called "normal point" contains a considerable amount of information like date of observation, atmospheric conditions, as well as time of flight, data quality and CCR arrays. The APOLLO instrumental accuracy (in terms of laser, detector, timing electronics, etc) shown by the fiducial returns in figure 6.1, is a root mean square contribution of 120 ps (18 mm). The differences between lunar and fiducial returns (shown in figure 6.1) is due to the tilt of the array on the lunar surface and it affects the accuracy of the ranging measurements.

Before describing the different phases of ephemeris calculation, it is important to define the frame of reference in which PEP calculations are carried out. PEP asserts that the solar system barycenter frame is an inertial frame. Thus far, there is no evidence to suggest otherwise. Although the forces are calculated in the solar system barycenter frame, PEP reports the positions and velocities of the solar system bodies with respect to the Sun's center of mass (Solar System Barycenter). The heliocentric coordinates of the solar system barycenter are also computed. Nevertheless, the physics is performed in the (inertial) solar system barycenter frame; the heliocentric coordinates are derived quantities.

6.2   PEP computation

PPN parameter β, γ and η

In PPN gravity, the parameter γ parametrizes the amount of spacetime curvature per unit mass, and the parameter β parametrizes the non-linearity of gravity. In GR, β and γ are exactly unity.

In the late 1960s, Kenneth Nortvedt showed that a violation of the Strong Equiva-

---

[1]reference to: http://www.physics.ucsd.edu/∼tmurphy/apollo/highlights.html
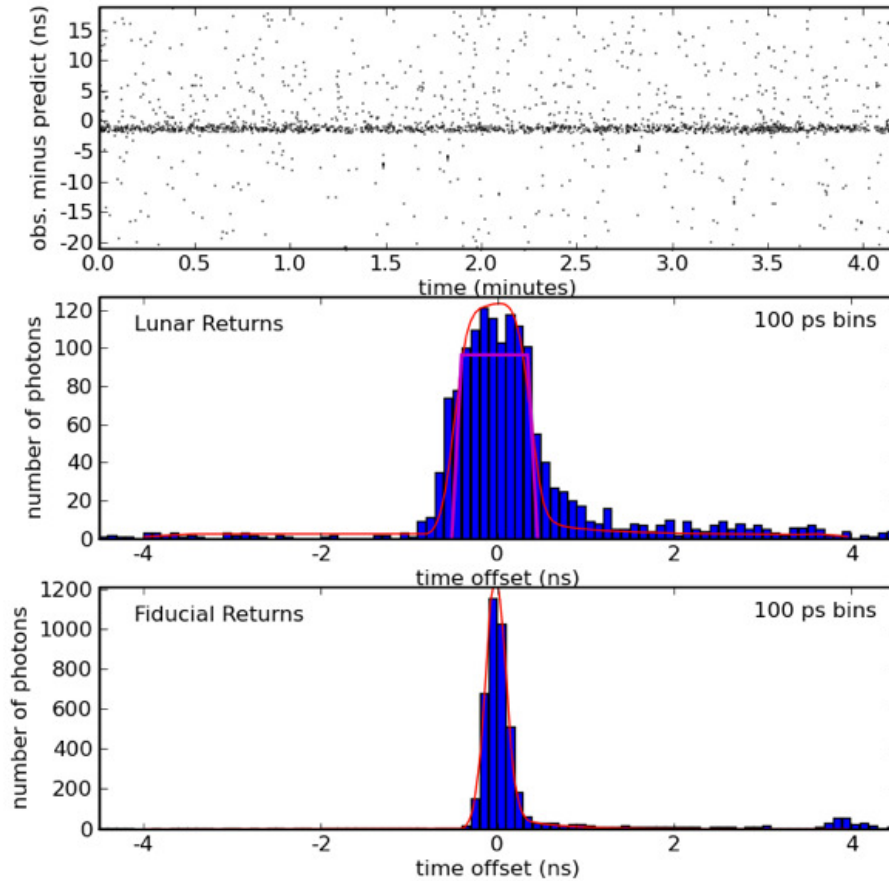
Figure 6.1: Example run of Apollo 15. In the plot, the top panel shows a 40 ns window of observed round trip time minus the predicted range. Background noise and detector dark current appear as scattered dots, while the lunar return is in the middle. The middle panel shows a histogram of the lunar returns, while the bottom panel shows the local "fiducial" CCR return, fitted by the red Gaussian. The Lunar return is additionally spread by the tilted reflector array modeled by the superimposed magenta trapezoidal shape[1]

lence Principle (SEP) could be parametrized by the parameter η, where:

$$\eta = 4 \times \beta - \gamma - 3 \tag{6.1}$$

In GR $\eta = 0$.

PEP can be used to derive constraints on the PPN parameters β and γ, as well as on η. As a matter of fact in PEP, there are two sets of β and γ parameters: to simplify the explanation we will call them (beta, gamma) and (beta', gamma'). The reason why we have two sets of PPN parameters derive from the historical development of the software. Originally, (beta, gamma) were included in the equations of motion, but the SEP was not implemented. Later, however, the Nordtvedt effect was added to PEP. In order to maintain backwards compatibility, the new set of parameters was added. The original (beta, gamma) pair does not control the SEP violation, and (beta', gamma') appear only in the SEP terms. However, the partial derivatives of (beta', gamma') are calculated as if they did both tasks (even though they do not).

In PEP, the Nordtvedt eta parameter appears in the following way:

$$\eta \times \Delta = (4 \times \beta' - \gamma' - 3) \times \Delta + (\eta \times \Delta)' \tag{6.2}$$

It turns out that PEP does not estimate η alone; it estimates the $(\eta \times \Delta)'$ product (in addition to estimating β' and γ'). Δ is the ratio of the gravitational self-energy (U) to the total mass-energy (Mc^2) of the body in question:

$$\Delta = \frac{U}{Mc^2} \tag{6.3}$$

There is an $\eta \times \Delta$ term for each body because Δ is body-dependent.

Geodetic precession

One of the consequences of GR is that the orbital plane of a planetary satellite precesses about the plane of the planet's orbit. This effect, known as geodetic precession, was pointed out by De Sitter in 1916. Regarding the Moon, this rate is about 2 arcseconds per century. There is also an advance of perigee analogous to

Mercury's perihelion advance (section 2.1), but this is orders of magnitude smaller, in fact it depends on Earth's mass rather than the Sun's one.

The equations of motion inside the software are cast in terms of Newtonian accelerations plus relativistic terms with coefficients composed by β and γ. In addition to that, there is a scale factor λ multiplying all the relativistic terms, and all of these parameters are programmed in variational equations so that any of them can be estimated by least-squares analysis of observation residuals. Thus, for PEP, any departure of β or γ from unity is equal to a violation of GR. On the other hand, any departure of λ from unity means a breakdown of PPN formalism.

In the same way, it is possible to add an ad hoc term to the equations of motion with an adjustable scale factor (called h) nominally zero, such as an extra precession of the Moon's node. The latter parameter is the key element of our study since it measures the agreement between the observed motion of the Moon and the De Sitter precession.

The equation of motions inside the code are defined in a coordinate system rotating in the instantaneous ecliptic at a (variable) rate $h\Delta\Omega$, where $\Delta\Omega$ is the de Sitter precession rate. Any departure in the lunar motion from the de Sitter rate is characterized by the numerical factor h, where $h = 0$ would be consistent with the prediction from GR and $h = 1$ would imply a 100% error in this prediction [Chandler 1985], [Ash 1972], [Tausner 1966], [Slade 1971].

6.3 LLR State of art and MoonLIGHT-2 sensitivity study

In the following subsection I will describe the sensitivity studies carried out during my PhD thesis for MoonLIGHT-2. In the first one I will describe the sensitivity study with 4 different MoonLIGHT-2 on the Moon (section 6.3.1) while in the second section the sensitivity study with 10 MoonLIGHT-2 is shown (section 6.3.2). Then in section 6.3.3 I repeat the first study only for the Moon Geodetic precession changing PEP conditions: first computing every parameter separately (to verify how

PEP can improve the sensitivity accuracy of the GR) and then simplifying the frame of reference using only the Earth-Moon system.

6.3.1   4 MoonLIGHT-2 Scenario

I have performed different numerical simulations in order to study the MoonLIGHT-2 CCR impact in GR tests in time for their deployment on the lunar surface[2].

For these simulations I have firstly used every LLR data available up to 2015. I have taken the data coming from the first LLR from 1960s until the data taken by the APOLLO station at the end of 2015. In figure 6.2a is reported the O-C residuals from all the data acquired using the three Apollo and the two Lunokhod arrays, then in figures 6.2b, 6.2c and 6.2d respectively the O-C of Apollo 11, Apollo 15 and Lunokhod 1. I chose to report only these O-C results because Apollo 11 and 14 have similar performances as well as for the Lunokhod 1 and 2. The plot in figure 6.2a (with the detail of some single array in figures 6.2b; 6.2c; 6.2d), represents the actual accuracy coming from the real arrays and shows that we have the best performances from the Apollo 15 in terms of accuracy and number of measurements.

---

[2]The first mission will be in 2018 with the Moon Express mission, for the other three Moon Express missions MoonLIGHT-2 was already proposed.
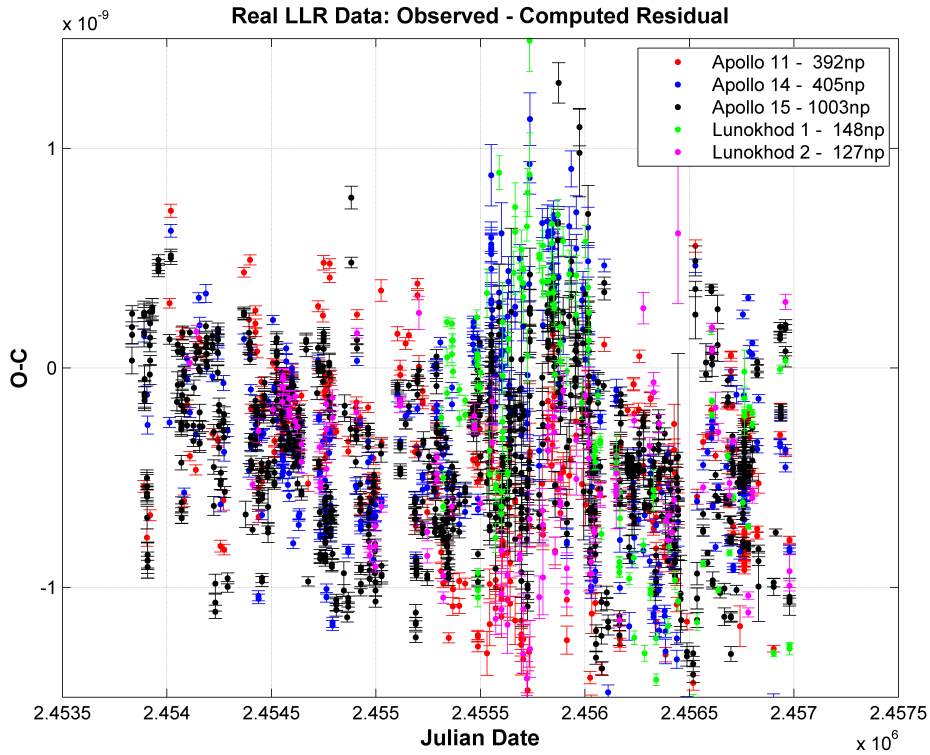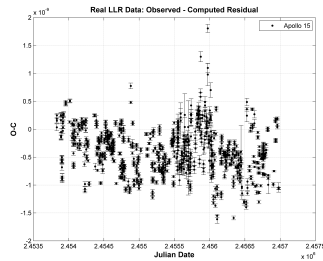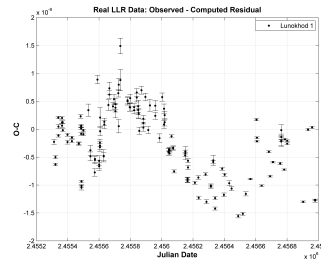
(a) O-C of Apollo 11, 14 and 15 with Lunokhod 1 and 2.
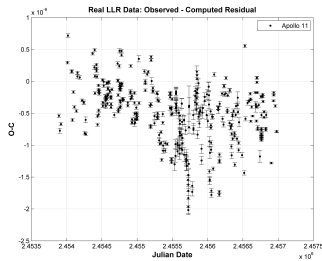
(b) O-C of Apollo 11. **(c)** O-C of Apollo 15. **(d)** O-C of Lunokhod 1.

Figure 6.2: O-C of LLR real data until 2015 with the normal points (np) for each array.

In addition to the real data I added a bunch of dummy observations using future MoonLIGHT-2 CCR. All the dummy observations were computed by PEP after defining CCRs positions on the lunar surface (figure 6.3) and the accuracy of the

CCR Array	Stations	Position	Cadence [g]	Central value accuracy [ps]		
				STD	Double STD	Half STD
OLD array	APOLLO	AP 11-14-15; Lun1-2	30	16	32	8
	CERGA		14			
	MLRS		20	33	66	16.5
	MLRO		8			
MoonLIGHT-2	APOLLO	80N, 80S, 80E, 80W	30	3	6	1,5
	CERGA		14			
	MLRS		20	7	14	3.5
	MLRO		8			

Table 6.1: Sensitivity studies parameter (4 MoonLIGHT-2 scenario)s and relative accuracy used for dummy data

ranging data (table 6.1). For the accuracy I have defined the values reported in table 6.1 as central value, then using a "Montecarlo" I obtain a gaussian distribution around the central value. Finally I chose a random value within 3σ of the central value. In this way it is possible to take into account the laser ground station systematic errors, reproducing more realistic measurements.

As shown in Table 6.1, I have used three different sets of parameters for the dummy observations.

For the simulated observations, the round-trip timing uncertainties are:

- STD: 16 ps for APOLLO and 33 ps for other sites on existing reflectors, and 3 ps for APOLLO and 7 ps for other sites on the proposed reflectors;

- Double STD: 32 ps for APOLLO and 66 ps for other sites on existing reflectors, and 6 ps for APOLLO and 14 ps for other sites on the proposed reflectors;

- Half STD: 8 ps for APOLLO and 16.5 ps for other sites on existing reflectors, and 1.5 ps for APOLLO and 3.5 ps for other sites on the proposed reflectors;

The assumed accumulation of future data is calculated with a cadence of 30 days for APOLLO, 20 days for MLRS, 14 days for CERGA, and 8 days for MLRO.
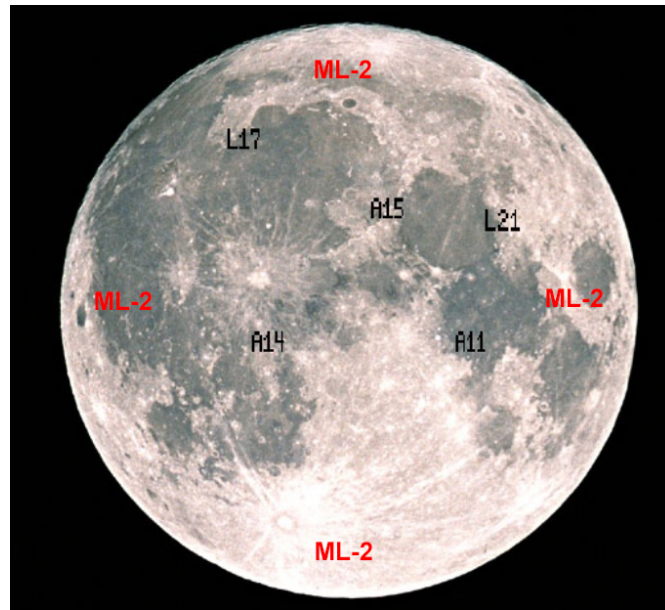
Figure 6.3: CCRs position on the lunar surface

The results obtained with this studies are shown in table 6.2 reporting the values for state of art, 2024 (chosen as medium point) and the ending point of simulations. The figures 6.4, 6.5, 6.6, 6.7 and 6.8 report the trend of the slope coming from all the simulations data results.

Table 6.2: Results of expected uncertainty improvements using 4 MoonLIGHT-2 payloads on the Moon for different accuracy sets

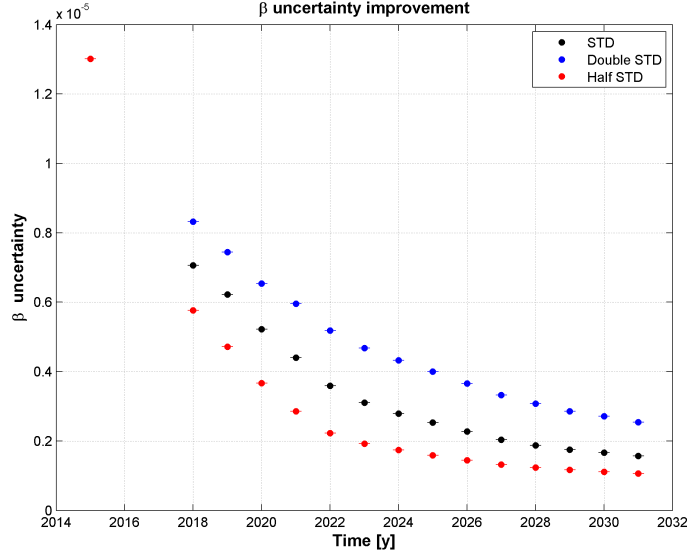| GR test	State of art	2024			2031		
		HALF	STD	DOUBLE	HALF	STD	DOUBLE
β	1.3×10^{-5}	1.7×10^{-6}	2.8×10^{-6}	4.3×10^{-6}	1.1×10^{-6}	1.6×10^{-6}	2.5×10^{-6}
γ	5.2×10^{-5}	7.1×10^{-6}	1.1×10^{-5}	1.7×10^{-5}	4.3×10^{-6}	6.4×10^{-6}	1.0×10^{-5}
$\dot{G}/G$	2.2×10^{-14}	3.3×10^{-15}	5.9×10^{-15}	9.4×10^{-15}	1.3×10^{-15}	2.5×10^{-15}	4.6×10^{-15}
h	1.4×10^{-4}	1.5×10^{-5}	2.8×10^{-5}	5.0×10^{-5}	8.2×10^{-6}	1.6×10^{-5}	3.0×10^{-5}

Figure 6.4: β uncertainty improvement, 4 MoonLIGHT-2 scenario

The accuracy (or σ) reported in the results is the purely statistical uncertainty in the estimation of parameters, assuming no systematic errors in the data or imperfections in the model. It is better to talk about the PEP solution values as "estimates", rather than "measurements", and therefore it is better to talk about of the "uncertainty" of the values, rather than their "accuracy". However, the main point to stress is that the sigma put out by PEP is a formal uncertainty and not always a realistic uncertainty.

Nonetheless at present it is possible to achieve millimeter level using old reflector array ([Murphy 2012]); the use of second generation retroreflector will provide the same (or better) accuracy with less integration time and so more good quality laser ranging measurements.

At this point, in order to validate the simulations results (as well the studies described in the following pages) it is also important to cite the paper [Reasenberg 2016]. In this work the authors assert that at present day the PEP models can not process residuals with an accuracy better than few centimeters. However the residual accuracy is independent from the accuracy estimates, that are the main focus of
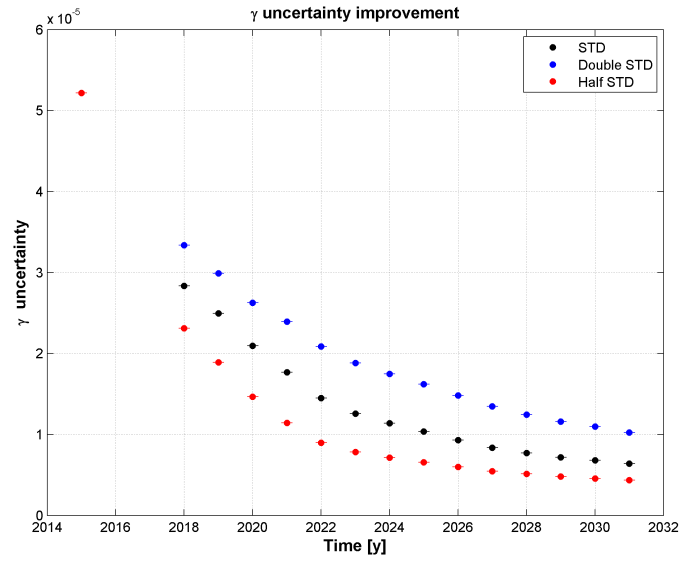
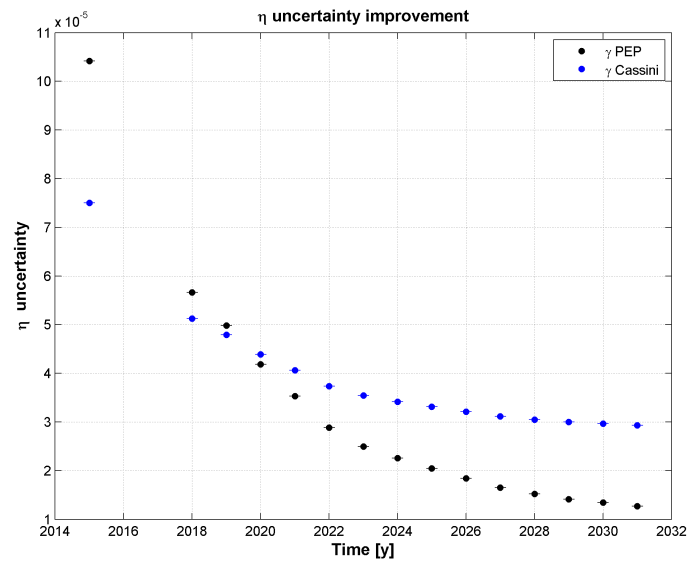**Figure 6.5:** γ uncertainty improvement, with 4 MoonLIGHT-2 scenario

Figure 6.6: η uncertainty improvement, with 4 MoonLIGHT-2 scenario
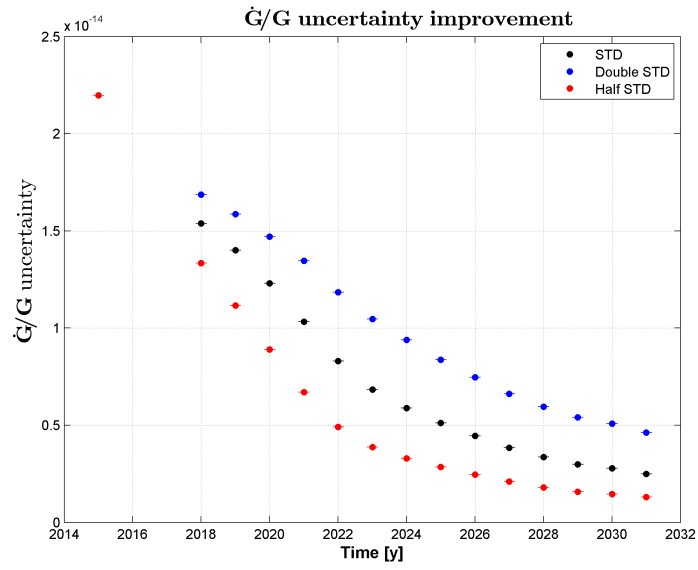
117

Figure 6.7: $\frac{\dot{G}}{G}$ uncertainty improvement, with 4 MoonLIGHT-2 scenario
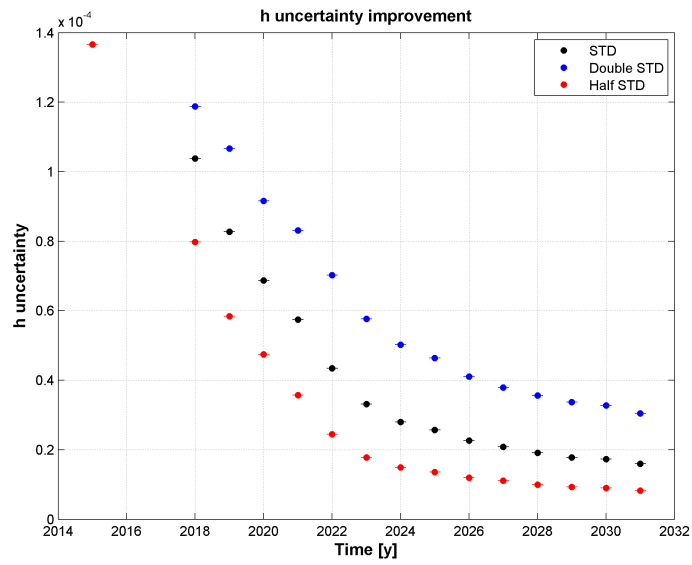

Figure 6.8: h uncertainty improvement, with 4 MoonLIGHT-2 scenario

118

this sensitivity study work. To put in a few words using the current version of the software we can process millimeter level data only as estimates but not as real measurements, and in order to process millimeter ranging data (or better) coming from (not only) future reflectors it must be necessary to update the models inside the software package.

Looking at the obtained results, no parameter here attains the best-case improvement of table 3.1. The main reason is that in the simulations I have used only the current ground laser station without any future (and already planned) upgrades for the next 15 years. The quality of the simulations are independent from the software update, as long as we are looking at accuracies and PEP will search only the more realistic simulation without choosing between better or worst case. It is the user that changes the scenario modifying the parameter data set. For these reasons I carried out the study described in 6.3.2.

6.3.2   10 MoonLIGHT-2 Scenario

In order to analyze also the best possible scenario, I repeat the sensitivity studies using more MoonLIGHT-2 CCRs. I add six more retroflectors (w.r.t. the previous simulation) on various lunar missions already scheduled or in study: Chang'e 4-5-6, Luna27 and two on the Moon Village. The starting year for data accumulation are respectively: 2018, 2021, 2022, 2020 and 2025.

The accuracy set (with the Montecarlo described before), cadency and ground stations are the same defined above for the previous simulation. In figures 6.9, 6.10, 6.11, and 6.13 are shown the simulation results while in table 6.3 we have the confrontation between the state of the art value, the 2024 and the ending point of simulation.

In this study all GR tests benefits of major improvements in accuracy, more than one order of magnitude for β and γ, while the parameter h benefit of the most significant improvements with almost two order of magnitude. All the tests here reach the values of best-case improvement of table 3.1. I should underline that this case represents, from the payload distribution point of view, the most optimistic case with a MoonLIGHT-2 successfully installed on all the lunar missions (already approved or only planned like the Moon Village) over the next years. On the other hand, from the laser ground station point of view, I have the same limits of the previous simulations (I do not consider any update/upgrade in the stations over the next 15 years).

Table 6.3: Results of expected uncertainty improvements using 10 MoonLIGHT-2 payloads on the Moon for different accuracy sets

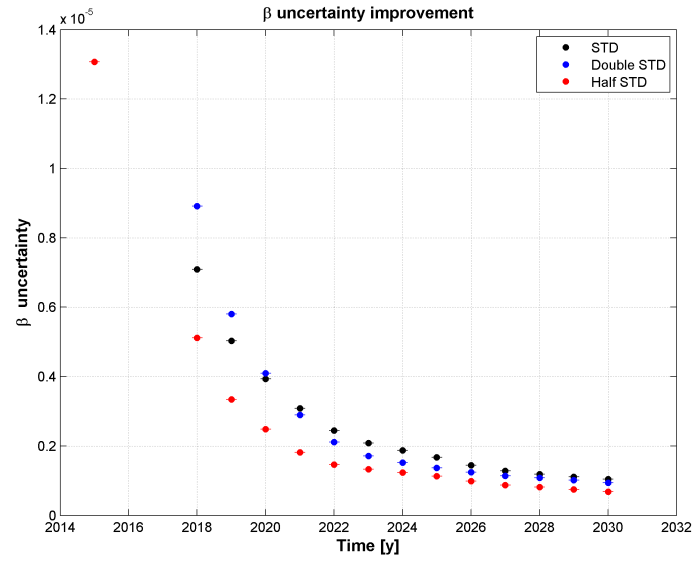| GR test	State of art	2024			2031		
		HALF	STD	DOUBLE	HALF	STD	DOUBLE
β	1.3×10^{-5}	1.2×10^{-6}	1.8×10^{-6}	1.5×10^{-6}	6.6×10^{-7}	1.0×10^{-6}	9.2×10^{-7}
γ	5.2×10^{-5}	4.9×10^{-6}	7.5×10^{-6}	6.1×10^{-6}	2.7×10^{-6}	4.2×10^{-6}	3.7×10^{-6}
$\dot{G}/G$	2.2×10^{-14}	1.8×10^{-15}	3.4×10^{-15}	2.6×10^{-15}	6.7×10^{-16}	1.3×10^{-15}	1.1×10^{-15}
h	1.4×10^{-4}	7.7×10^{-6}	1.5×10^{-5}	1.3×10^{-5}	4.3×10^{-6}	8.1×10^{-6}	6.7×10^{-6}

Figure 6.9: β uncertainty improvement, 10 MoonLIGHT-2 scenario
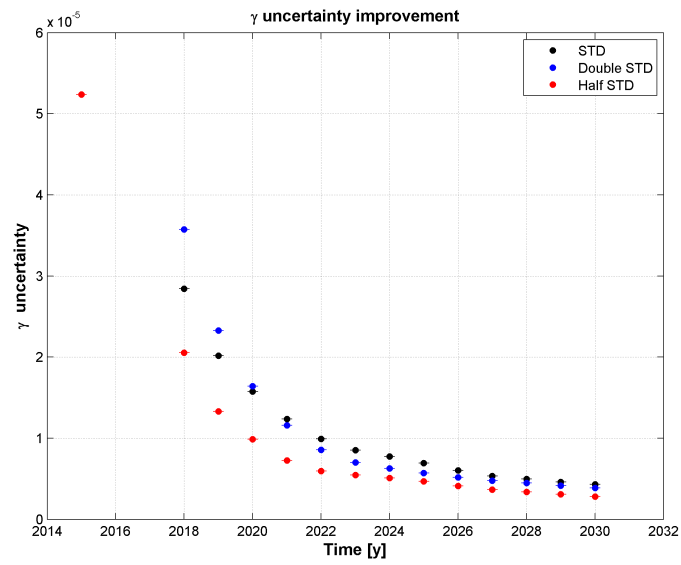

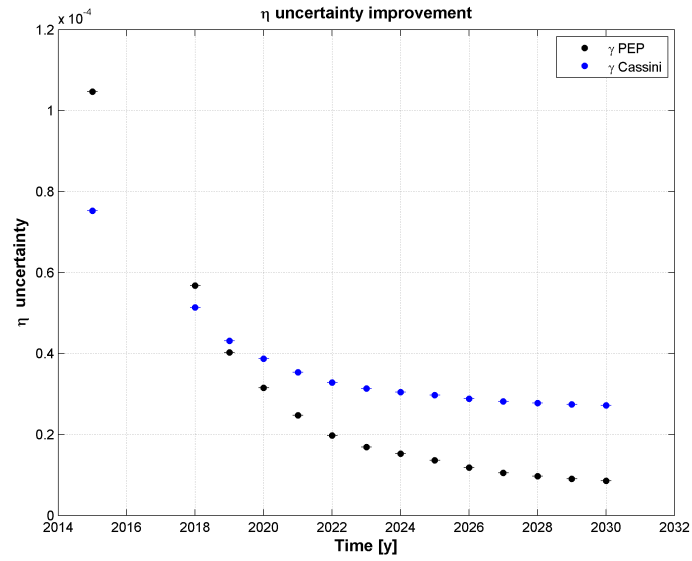**Figure 6.10:** γ uncertainty improvement, 10 MoonLIGHT-2 scenario

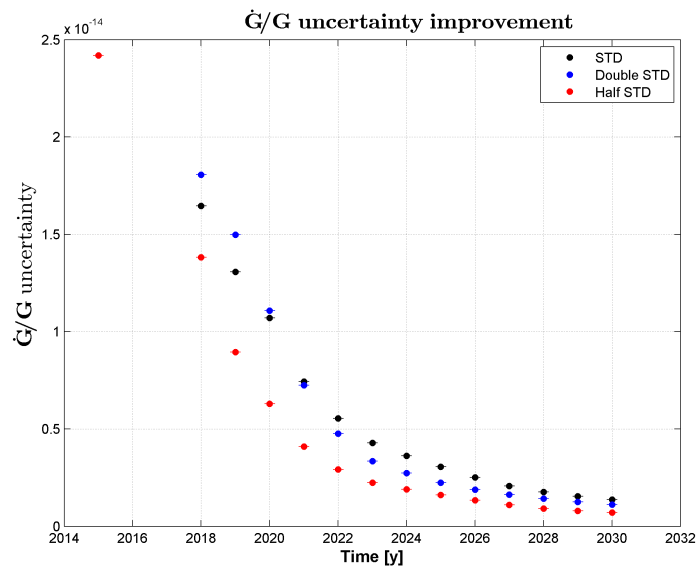**Figure 6.11:** η uncertainty improvement, 10 MoonLIGHT-2 scenario

Figure 6.12: $\frac{\dot{G}}{G}$ uncertainty improvement, 10 MoonLIGHT-2 scenario
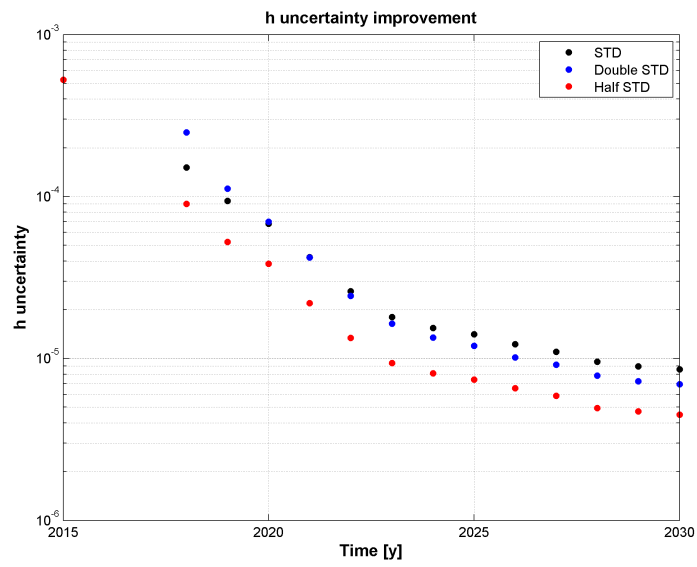
Figure 6.13: h uncertainty improvement, 10 MoonLIGHT-2 scenario

6.3.3 KGP parameter study

In this section I want to study only the Geodetic Precession parameter h fixing any other extra-Moon parameter. I proceed in two ways: first I fix other parameter to their GR value computing only h, then I remove any other solar system body gravitational contribute with the exception of the Earth-Moon system.

In figure 6.14 I plot the h central value, computed in the first way, with its accuracy using the data coming from the first scenario simulations (section 6.3.1) condition with STD accuracy set. I can see that right after the simulated deployment of the first MoonLIGHT-2 in 2018 and the analysis of mm data I reach an asymptote. This effect suggests again that the models inside the code need improvements in order to process future high quality data like the ones on the first sensitivity study. However speaking about accuracies I do not have any variation w.r.t. the value in table 6.2, because the parameter sensitivity is independent from how many parameters you consider. Hence the results described above are consistent with our considerations and are in agreement with the studies for the 4 and 10 MoonLIGHT-2 scenarios.

I can compare now the state of the art value obtained computing only h (now tagged as *Solo*) with the one computed with all the other parameters (as in the simulation before and now tagged as *All*):

$$\textbf{Solo} : h = (-7.4 \pm 0.2) \times 10^{-3}$$
$$\textbf{All} : h = (-7.9 \pm 0.2) \times 10^{-3}$$

This shows a slightly improvement in the parameter, about 6%.

Now I remove all the Solar System body (results will be tagged as *Solo&3body*) to study other possible variation from the central value obtaining:

$$\textbf{Solo \& 3body} : h = (-5.6 \pm 0.2) \times 10^{-3}$$

This produces a greater improvement in the h central value, around 30%; also the sensitivity benefits of any improvements respect to the case in section 6.3.2 and comparing figure 6.15 (3body solution) with figure 6.8 (all Solar System body solution)
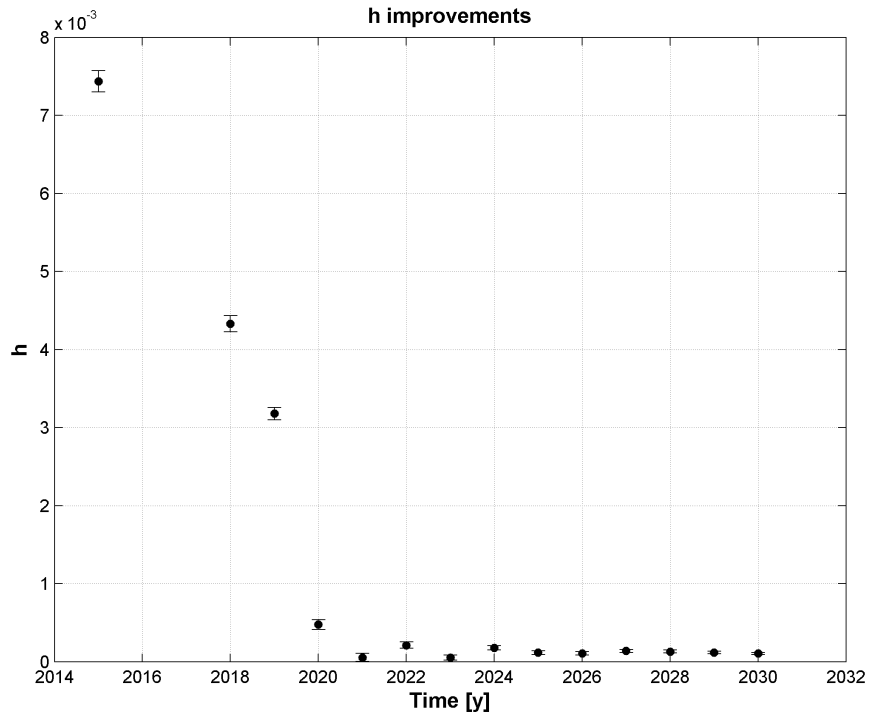
Figure 6.14: Geodetic precession central value, computed removing the other relativistic parameter, with its uncertainty improvement during a long time simulation using 4 MoonLIGHT-2 CCRs

we can see improvements about a factor 3-4 by the end of simulation:

$$\textbf{Solo \& 3body} : \sigma_h = 1.6 \times 10^{-5}$$

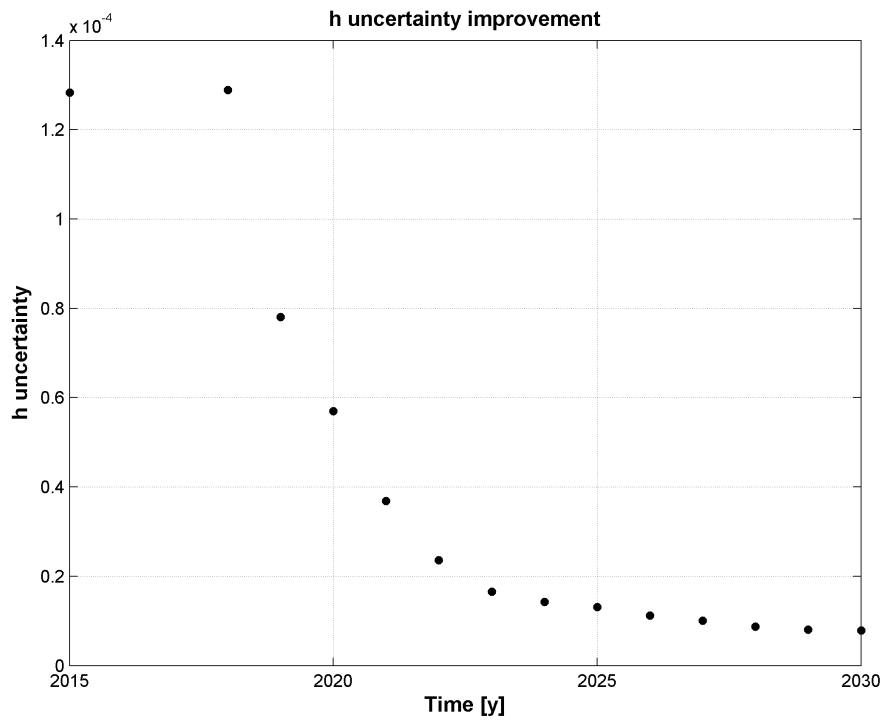$$\textbf{All} : \sigma_h = 7.7 \times 10^{-6}$$

Figure 6.15: Geodetic precession uncertainty improvement with a 3 body simulation during a long time simulation using 4 MoonLIGHT-2 CCRs

6.3.4 State of art and Sensitivity study Conclusions

The sensitivity studies carried out with PEP show that we have a possible improvement in GR tests using MoonLIGHT-2 with a configuration with 4 payload on the Moon of about one order of magnitude for β, γ, $\frac{\dot{G}}{G}$ and h, depending on the accuracy of the laser ranging data. Regarding η, assuming in this study no possible and future improvements from the Cassini and other interplanetary mission, I can conclude that using only LLR technique I need at least 4 years of good quality data in order to achieve Cassini result. The improvements in these simulations tell that there is a strong dependence on ranging measurement accuracy. The best case, HALF STD, improves the STD results by a factor $4 - 5$ for all tests.

The second sensitivity study, the scenario with 10 payload on the Moon, provides most significative improvements respect to the previous study, and it has a similar slope. This suggests us that the improvement in GR tests will directly depend obviously on how many new retroreflectors will be deployed on the Moon but the quality of the laser ranging data is the most significative condition.
It is important to underline that by the end of the simulation time span (after 2028) I can not distinguish between the three accuracy sets. The reason is that I reach an asymptote and I need further improvement on the PEP code in order to evaluate major order contributes as shown also in figure 6.14.

Looking at the results in section 6.3.3 I can conclude that future studies will be dependent on which parameter I consider inside the computation. MoonLIGHT-2 is designed mainly for lunar GR tests like h parameter, hence the best results will come removing any other parameter from the computation and any other gravitational influence different from the Earth-Moon system.

6.4   INRRI Sensitivity study

In this section I will describe the sensitivity study with PEP in order to quantify the expected improvements with an INRRI network on Mars. The GR parameter studied are β, γ, η (calculated with the same procedure as described above for MoonLIGHT-2) and $\frac{\dot{G}}{G}$; I do not consider the Geodetic Precession, h parameter, since it is a pure lunar parameter and I can not obtain any improvements using Mars. I simulate 5 arrays at the landing site of: Phoenix lander, Viking 1 & 2 lander, Curiosity and Opportunity Rovers (figure 6.16).
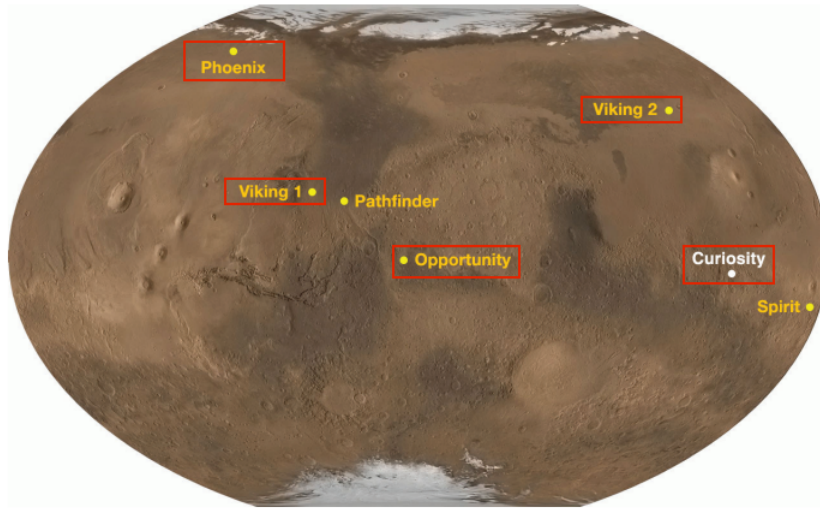

Figure 6.16: INRRI deployment configuration for the sensitivity study

I firstly use as state of the art the values given in the MoonLIGHT-2 simulations, then I add one new INRRI arrays every two years starting from 2018, until I have all the 5 array on Mars surface in 2026. The cadency is one measurement every 10 days for each payload. The round trip accuracy is given by the combination between the laser ranging from payload to orbiter and the laser communication from orbiter to Earth ([Dell'Agnello 2017]). For this reason I use two scenario with 3 accuracy set configurations in order to analyze a great range of possible Mars-Earth distance accuracy values:

- Scenario A: 1000m - 100m - 10m

- Scenario B: 10m - 1m - 0.1m

At present I do not have any kind of CCRs array on Mars so I are still in a concept phase of the study. In other words I will also need laser orbiter around Mars to complete the ranging measurements from above. However the technology (also from the laser communication side) is still under investigation/improvements so I want to see various range span also taking into account any possible evolution coming from not only the space segment but also from the technology part, from now to the future years. The two chosen scenarios provide us a wide range of possible improvements.

In table 6.4 I summarize the results obtained as described before, while in figures 6.17, 6.18, 6.19 and 6.20 I report the direct comparison between the two scenarios for each GR test.

Table 6.4: Results of expected uncertainty improvements using 5 INRRI payloads on Mars for different accuracy sets

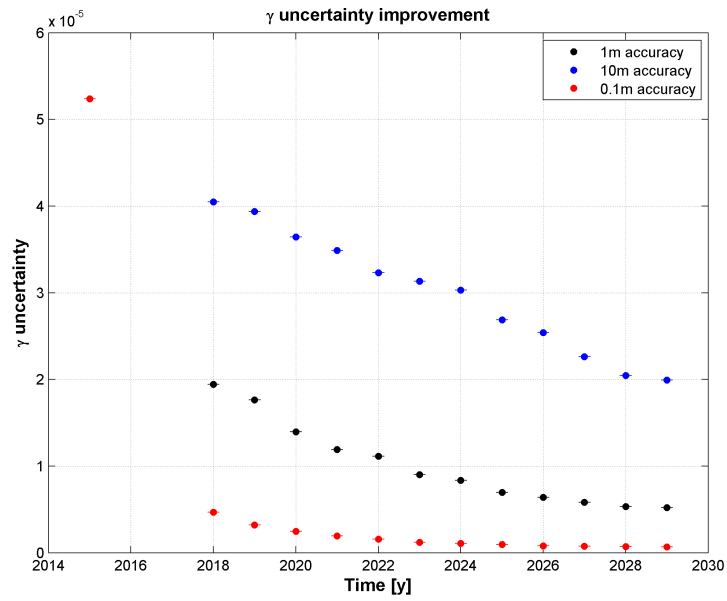| GR test	State of art	2022			2030		
		100m	1m	0.1m	100m	1m	0.1m
β	1.3×10^{-5}	1.1×10^{-5}	2.8×10^{-6}	3.9×10^{-7}	1.0×10^{-5}	1.3×10^{-6}	1.7×10^{-7}
γ	5.2×10^{-5}	4.6×10^{-5}	1.1×10^{-5}	1.5×10^{-6}	4.3×10^{-5}	5.2×10^{-6}	6.6×10^{-7}
$\dot{G}/G$	2.4×10^{-14}	1.8×10^{-14}	3.6×10^{-15}	1.4×10^{-15}	1.2×10^{-14}	7.2×10^{-16}	1.4×10^{-16}
h	5.2×10^{-4}	5.2×10^{-4}	5.2×10^{-4}	5.2×10^{-4}	5.2×10^{-4}	5.2×10^{-4}	5.2×10^{-4}
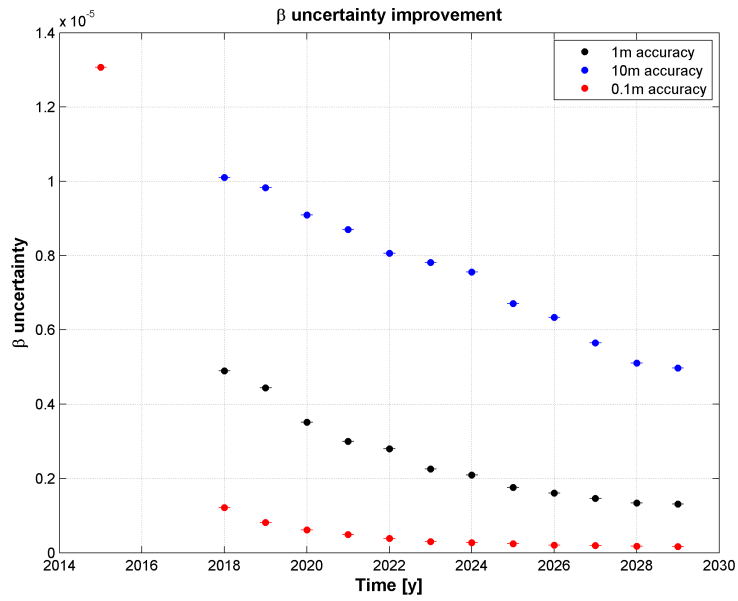
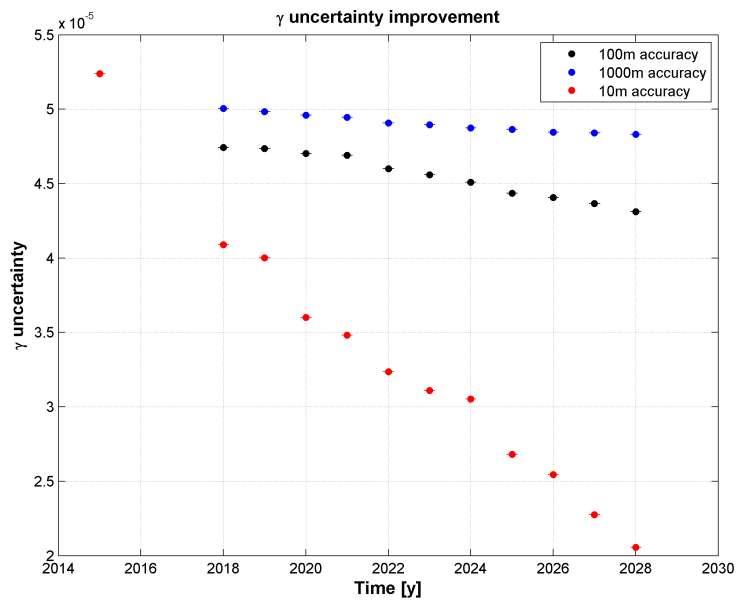**(a)** 10-1-0.1 meters accuracy set
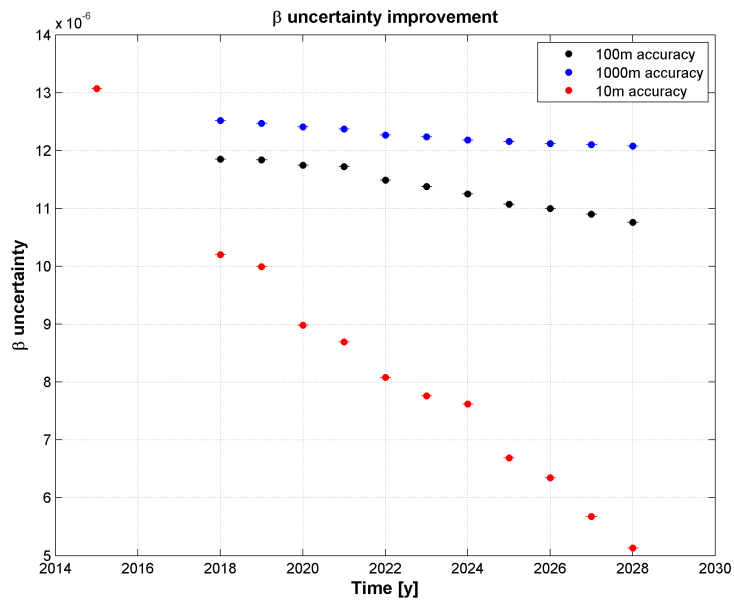
(b) 1000-100-10 meters accuracy set

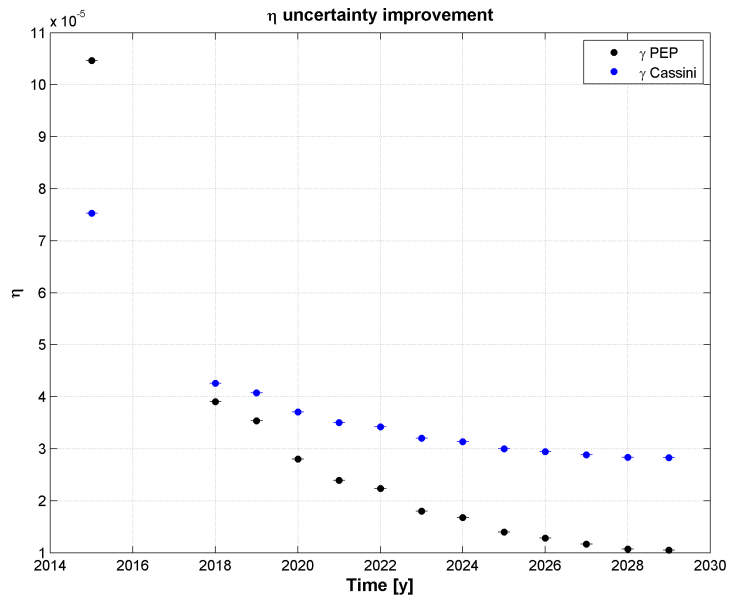**Figure 6.17:** β uncertainty improvement, using INRRI on Mars

(a) 10-1-0.1 meters accuracy set

(b) 1000-100-10 meters accuracy set

Figure 6.18: γ uncertainty improvement, using INRRI on Mars
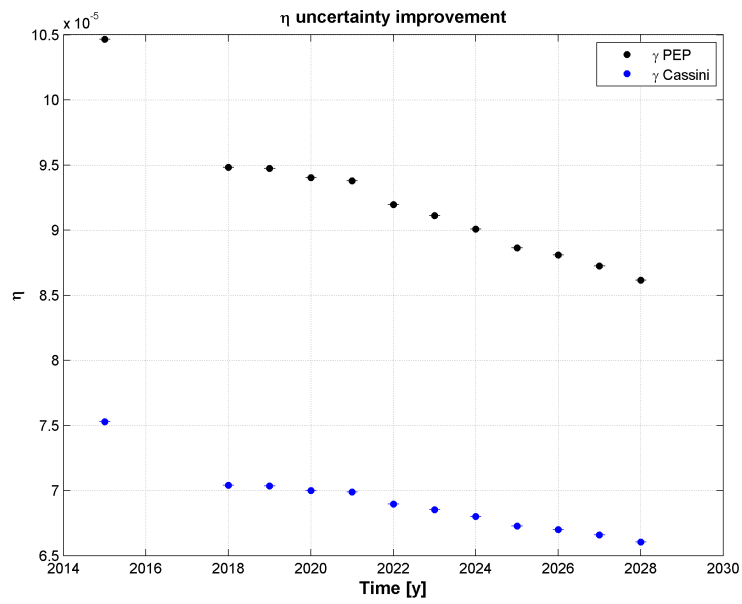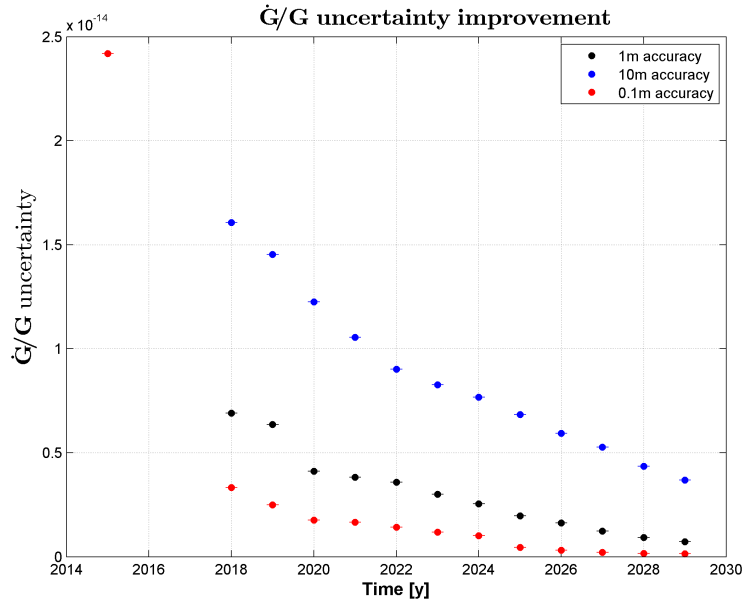
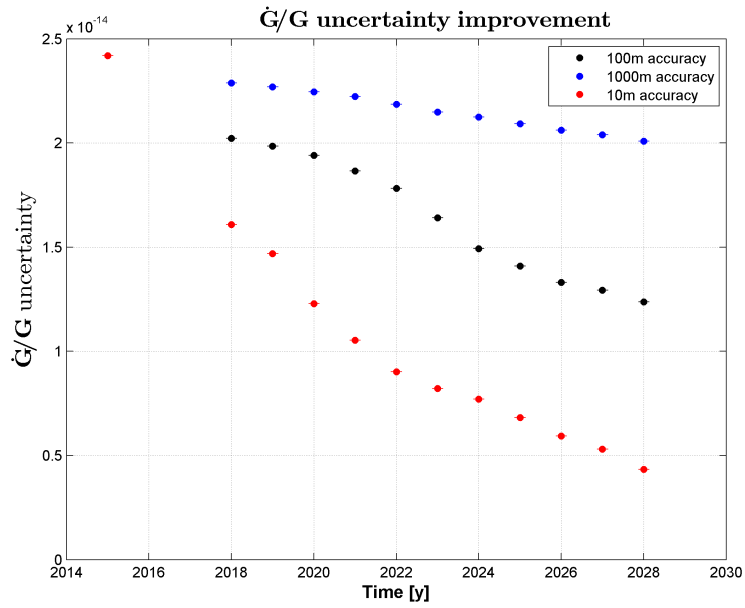**(a)** 1m accuracy for ranging data

(b) 100m accuracy for ranging data

Figure 6.19: η uncertainty improvement, using INRRI on Mars

(a) 10-1-0.1 meters accuracy set

(b) 1000-100-10 meters accuracy set

Figure 6.20: $\frac{\dot{G}}{G}$ uncertainty improvement, using INRRI on Mars

6.4.1 Sensitivity study conclusions

The results show a clear change of slope below the accuracy of 10 meters for every tests, where I obtain an improvement around half order of magnitude for β and γ and one order for $\frac{\dot{G}}{G}$. In the Scenario B provides better improvements (as expected) for each test, reaching more than one order of magnitude. Regarding η we can see that in the Scenario A (with accuracy data of 100m) I can not reach the Cassini level, I need the Scenario B (1m) to go beyond the Cassini level right after the first INRRI deployment and acquisition.

However the GR tests with Mars are strongly dependent on the Mars orbit accuracy, and this one is by itself dependent on the asteroid belt mass estimation. At the present the knowledge of the asteroid belt led us to an Mars Ephemeris accuracy of about 50m ([Folkner 2014] and [Dell'Agnello 2017]) and I will need major PEP model updates in order to analyze the real data. By the way the results presented are only estimates of sensitivity and are independent from the PEP update, as long as we are looking at accuracies.

Conclusions & Future prospects

The LLR key elements are a LRA on the Moon and a Laser Ground station on the Earth: the station sends a laser beam to the CCR that retroreflects the beam back to Earth, then by a time of flight measurement we obtain the Earth-Moon distance. This technique was used since 1969 to perform various GR tests, like the PPN parameters or the strong and weak equivalence principle tests. Currently on the Moon there are 5 different LRA: 3 from Apollo missions (Apollo 11-14-15) and 2 from Lunokhod missions (Lunokhod 1-2). With this equipment we are able to measure the Earth-Moon distance with an accuracy of few cm (mm level with long acquisition time and post process analysis). These old LRAs will continue to operate and provide new data, however their geometry combined with the lunar libration is now limiting the precision of the single photoelectron returns and hence the sensitivity of the scientific results in slow motion and weak field regime.

The SCF_Lab, at INFN-LNF is proposing two next generation CCR payloads in order to provide data useful to constraints GR theories ([March 2013]):

- MoonLIGHT-2 for the Moon. It is composed by a single large CCR with 100mm diameter, unaffected by the lunar libration and will support improvements in ranging precision, by one order of magnitude, depending on the method of deployment.

- INRRI for landing and rovering on rocky solar system body. It is a small retroreflector array (7 cm diameter for 3 cm height, mass = 25 g) composed by 8 CCRs with 13 mm diameter glued to an aluminum chassis. With INRRI it is possible to use planets like Mars (or rocky satellites) as new test body

like today is the Moon.

My PhD thesis regards MoonLIGHT-2 and INRRI experimental tests, and sensitivity studies carried out in order to study the expected improvements in GR after their deployment.

Experimental Activity: Characterization tests

The goal of the experimental activities are the thermal and optical characterization of MoonLIGHT-2 and the INRRI test validation for the launch with Exomars 2016.

MoonLIGHT-2 has been optically and thermally characterized at the SCF_Lab, a laboratory designed to qualify space optics in a simulated space environment, with the so called "SCF-Test". During the test we take IR pictures in order to study the CCR front face temperature distribution and evolution (trough the thermal constant τ_{ccr}), and FFDP to study the optical behavior. My thesis activities were to manage the test campaigns, develop all the SW for the test control and the IR thermal analysis. We carried out three different test campaigns with different MoonLIGHT-2 configurations. The results always shows long τ_{ccr} in agreement with the simulations, however in the first test campaign I found an important thermal gradient on the CCR front face that produce a sizeable decrease in the optical performances. We were thus able to reduce this degradations in the following tests (changing the mechanical payload structure) and obtained a good optical performance in agreement with the simulations.

The INRRI characterization tests was carried out in order to qualify the payload for the flight with ESA Exomars 2016 mission. The test carried out was a TVT reproducing the thermal conditions during the launch; a peel test on each CCR before and after the TVT in order to check the glue performance; a vibration test (sine and random environment) along with a pyroshock test always to reproduce the launch stress conditions. My activities were to manage the TVT and peel tests, the experimental setup and SW development for test control and finally the data analysis. INRRI successfully completed all the tests and finally was accepted for ESA-ExoMars 2016, launched to Mars from Baikonur, on 14th March 2016. The

payload reached the red planet on 21st October 2016 but after the failed landing the payload conditions (as well as the lander itself with other instrumentations) are still under investigation.

Sensitivity studies: expected improvements in GR tests

The studies were performed in collaboration with the CfA using the software package PEP. The GR tests taken into account were the PPN parameters β and γ, $\frac{\dot{G}}{G}$ and the Moon Geodetic precession (only for MoonLIGHT-2).

Regarding MoonLIGHT-2 I did different studies in order to define if the payload needs or not a Sunshade and then to study the improvements in GR tests accuracy in different configurations (varying the payload configuration on the Moon and the LLR data accuracy). I first discovered that the payload performances are poorly affected by the presence of a Sunshade, so we decided to remove it to minimize weight and volume for the launch. The sensitivity studies tell us that the GR test are strongly dependent from the accuracy, less from the number of payloads on the Moon. With 4 MoonLIGHT-2 I obtained around one order of magnitude in the sensitivity for all the test, this improvements become slightly less than two order of magnitude using 10 MoonLIGHT-2.

For INRRI I studied the impact in GR test sensitivity of a first-ever network of INRRI on Mars. The fist operational INRRI will reach Mars with the InSight 2018 [3] Lander mission of NASA ; then two more payloads will be deployed with the ExoMars 2020 Rover [4] (probably also on this Rover landing platform) and the Mars 2020 Rover [5]. I simulated various accuracy sets in the Mars-Earth distance measurement assuming either radio or laser ranging to a Mars orbiter that will observe the INRRI network on the surface of Mars. The results tell us that there will be a clear increase in the improvements with accuracy in Mars-Earth distance below than 10 m (feasible with radio ranging, and easily improvable with laser ranging), leading to an increase in the sensitivity from half order to more than one

---

[3]reference to: http://insight.jpl.nasa.gov/home.cfm

[4]reference to: http://exploration.esa.int/mars/48088-mission-overview/

[5]reference to: http://mars.nasa.gov/mars2020/mission/overview/

order of magnitude for all the tests.

For the near future we are moving forward to the following major points:

- Final improvements of the MoonLIGHT-2 payload configuration, then final launch validation tests.

- Deploy INRRI for the already approved missions: InSight Lander 2018 and ExoMars 2020 Rover . Here we must realize the flight validation tests with a similar procedure already realized (and described in this thesis work) for Exomars 2016. With the InSight Lander 2018 we will have the first retroreflector array on Mars.

- Propose INRRI for the SpaceX Lander 2018 [6] , Mars Rover 2020 and Landing Platform 2020

- Work on the improving the PEP software in collaboration with the CfA. Presently PEP can not process residuals with an accuracy better than centimeter level. Therefore in order to take full advantage of millimeter accurate ranging data (or better) coming from MoonLIGHT-2 it will be necessary to update models inside the PEP software package.

- After the MoonLIGHT-2 deployment on the lunar surface, acquire the second generation of LLR measurements and then analyze these data in order to obtain improved GR tests.

---

[6]reference to: http://www.spacex.com/

Appendix A

MoonLIGHT-2 Optical Simulations

The retroreflected beam from the CCR to the ground station on Earth is a diffracted beam, and its intensity distribution on a screen in the far field is function of: optical properties of the retroreflector, material, dimensions and dihedral angle offsets. In addition other environmental effects affect the CCR optical response at the ground station, most of all the relative motion with respect to the ground station (also named as Velocity Aberration (VA)), orientation of the laser beam on retroreflector front face and the characteristics of the laser beam, its wavelength and polarization. The SCF_Lab team, using the optical commercial software CodeV, carried out different optical simulation in order to study the main physical and optical characteristics of the MoonLIGHT-2 retroreflector.

MoonLIGHT-2 retroreflector inherits its basic characteristics from Apollo retroreflectors: an uncoated prism of Suprasil 311 with a circular front face aperture of $100\,mm$ and an apex length of $72.4\,mm$. The retroreflector dimensions instead were considered as a fixed characteristic due to technological/budget restrictions: the increasing cost in the realization of a big prism of fused silica with proper optical quality and the increase of wavefront distortions due to space environment as increasing dimensions of retroreflectors. For the simulations a green laser beam at

Table A.1: Latitude and VA for LLR Stations

LLR Station	Latitude [°]	VA Moon [μrad]
Operational		
APOLLO	32.78N	4.18
Matera	40.65N	4.44
Grasse	43.75N	4.55
McDonald	30.68N	4.12
Future or non operational		
Wetzell	49.14N	4.76
Mount Stromlo	35.32S	4.26
Hartebeesthoek	25.89S	4.00

$532\,nm$ wavelength is used, since the majority of existing laser ranging systems uses this wavelength.

Last but not least there is to consider the relative motion between the satellite (or Moon) and the ground station during the laser beam travel. This motion produces a shift in FFDP domain, that affect the angular position where to evaluate the optical response of the retroreflector in the FFDP image domain. For a retroreflector on the the Moon the VA in not evenly distributed in the FFDP plane and is off-centered to the right in this plane (as will be shown later). The value of this shift depends on the latitude of the ground station. Nowadays there are few active LLR stations concentrated in the northern hemisphere, for more information about the station and their VA see table A.1. Based on these data the SCF‗Lab team decided to evaluate the optical response in the range $4.0 \div 4.5\,\mu rad$ on an horizontal segment on the right of the FFDP domain.

Using the conditions described above as basic assumption made for the simulations, and using the condition of a physical edge vertical and an horizontal polarized beam with this kind of CCR, the obtained FFDP is like the one in figure A.1 In order to optimize the optical response, the optical design we must maximize the inten-
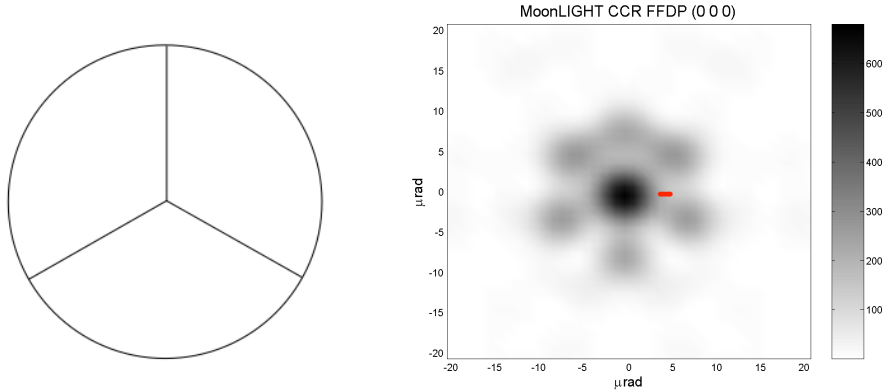
Figure A.1: on left: Reference 0° orientation for simulated CCR.FFDP of a perfect uncoated retroreflector with physical edge vertical and horizontal polarization. **on right:** Red segment indicates VA range where optical response is calculated.

sity of the returning signal in chosen VA range introducing an angle offset in the retroreflector faces, the DAO. In a retroreflector three DAOs can be set, but since the optical response must be evaluated in the specific range shown in figure A.1, the simulation do not considerate the case with three different DAOs and take in account only two equal DAOs or only one DAOs, in the range $[-1; 1]$ arcsec with 0.1 arcsec step.

Another key element is the orientation of the retroreflector with respect to the polarization. Assuming as 0 reference orientation is as in figure A.1, with a physical edge vertical the simulation change the orientation in the range $[-120°; 120°]$ with 30° step.

Finally since the LLR stations use linear polarized beams, but they cannot control its direction and considering that uncoated retroreflectors FFDPs are influenced by the polarization of the laser beam, the simulations span the direction of the linear polarization from horizontal (90) to vertical (0). During this phase only linear polarization is take in account.

The following plots show the results of such simulations done for a single DAO case and a double DAO case. In the single DAO case the offset was assigned to the vertical edge in figure A.1. In the two DAO case the offsets were assigned to the
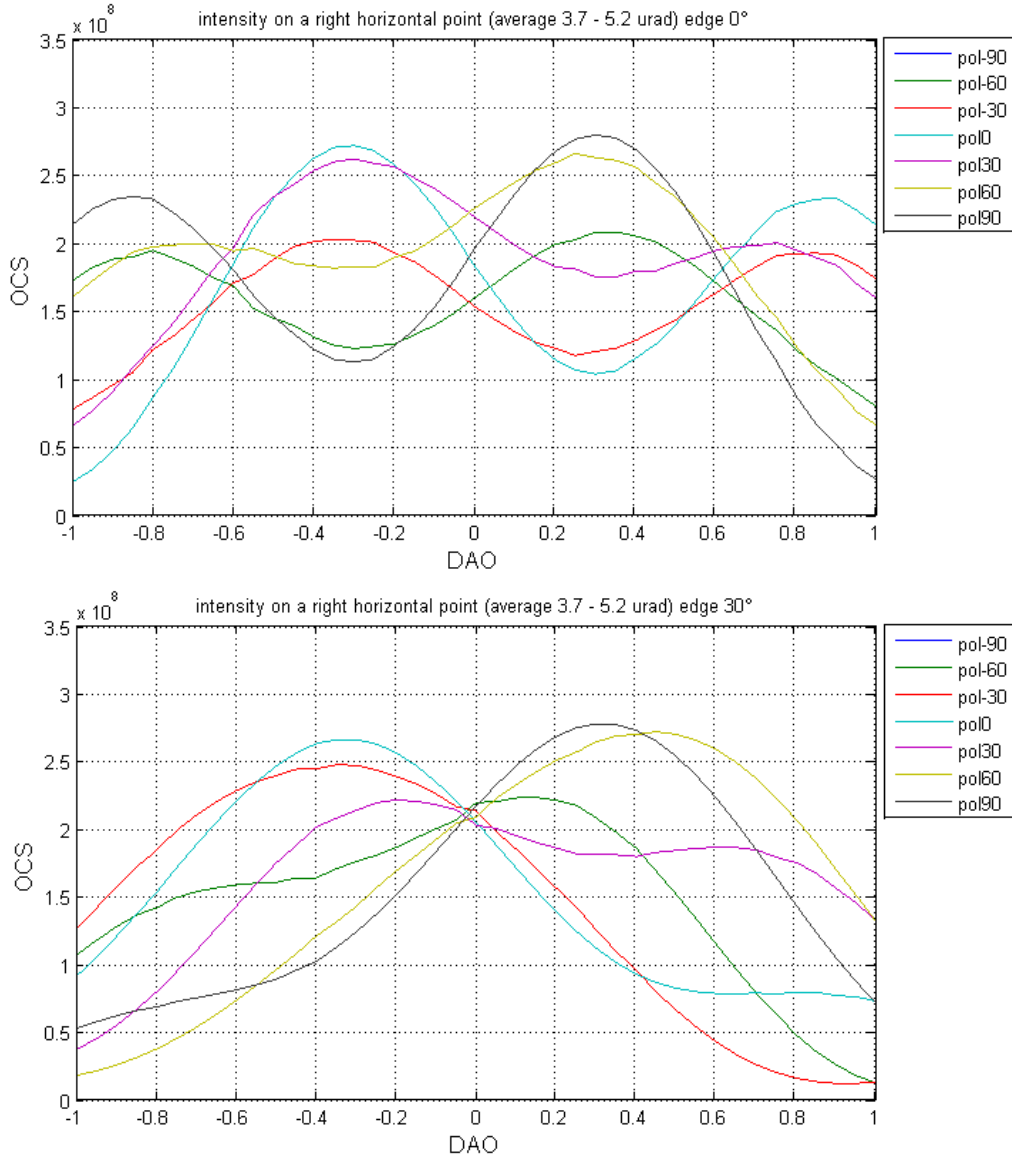
two bottom edges of figureA.1.

Figure A.2: Single DAO simulations. CCR orientation 0° and 30° (negative cases are just symmetric).

Since it is not known in advance the polarization of the laser beam hitting the retroreflector, in order to determine the optimum solution a single point on the
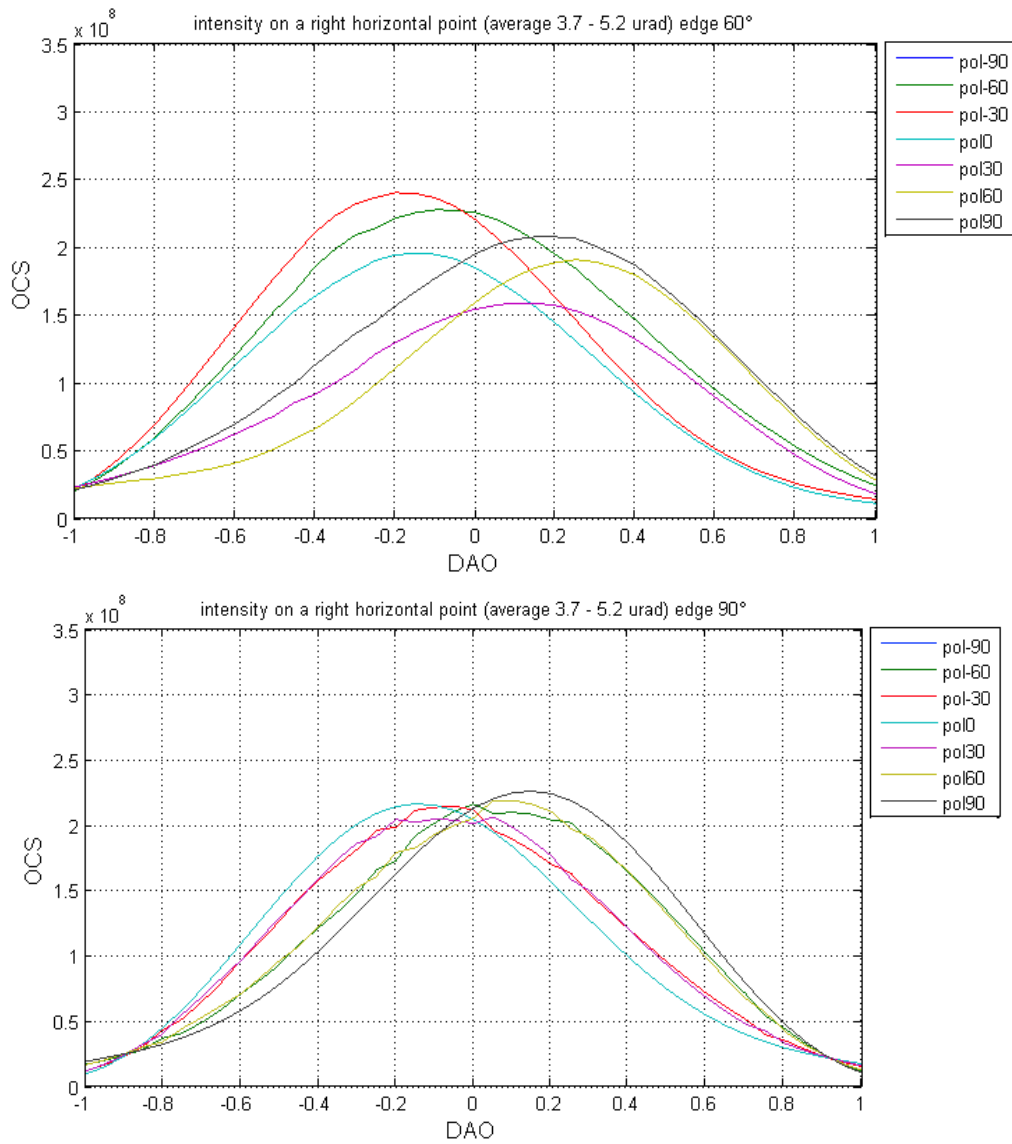
144

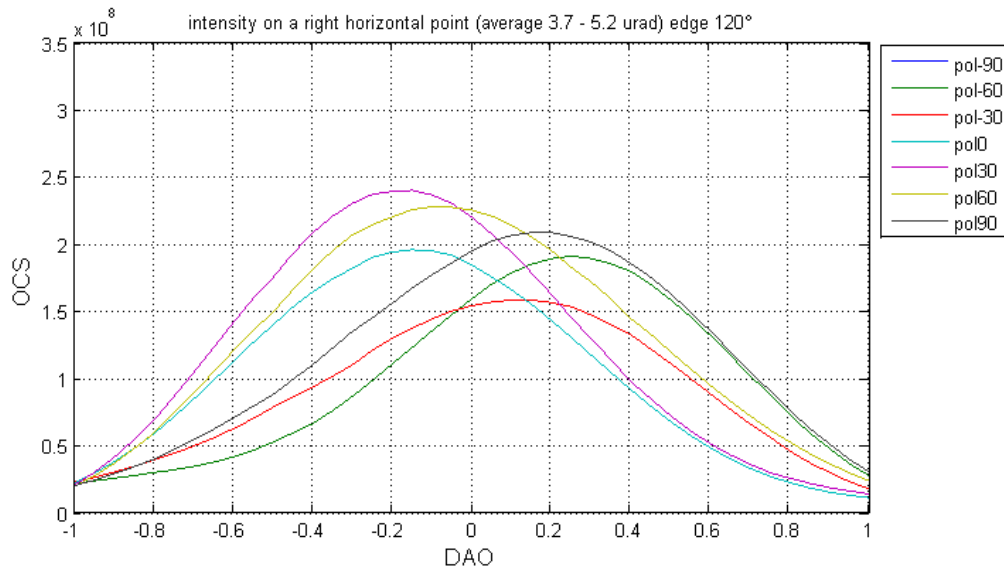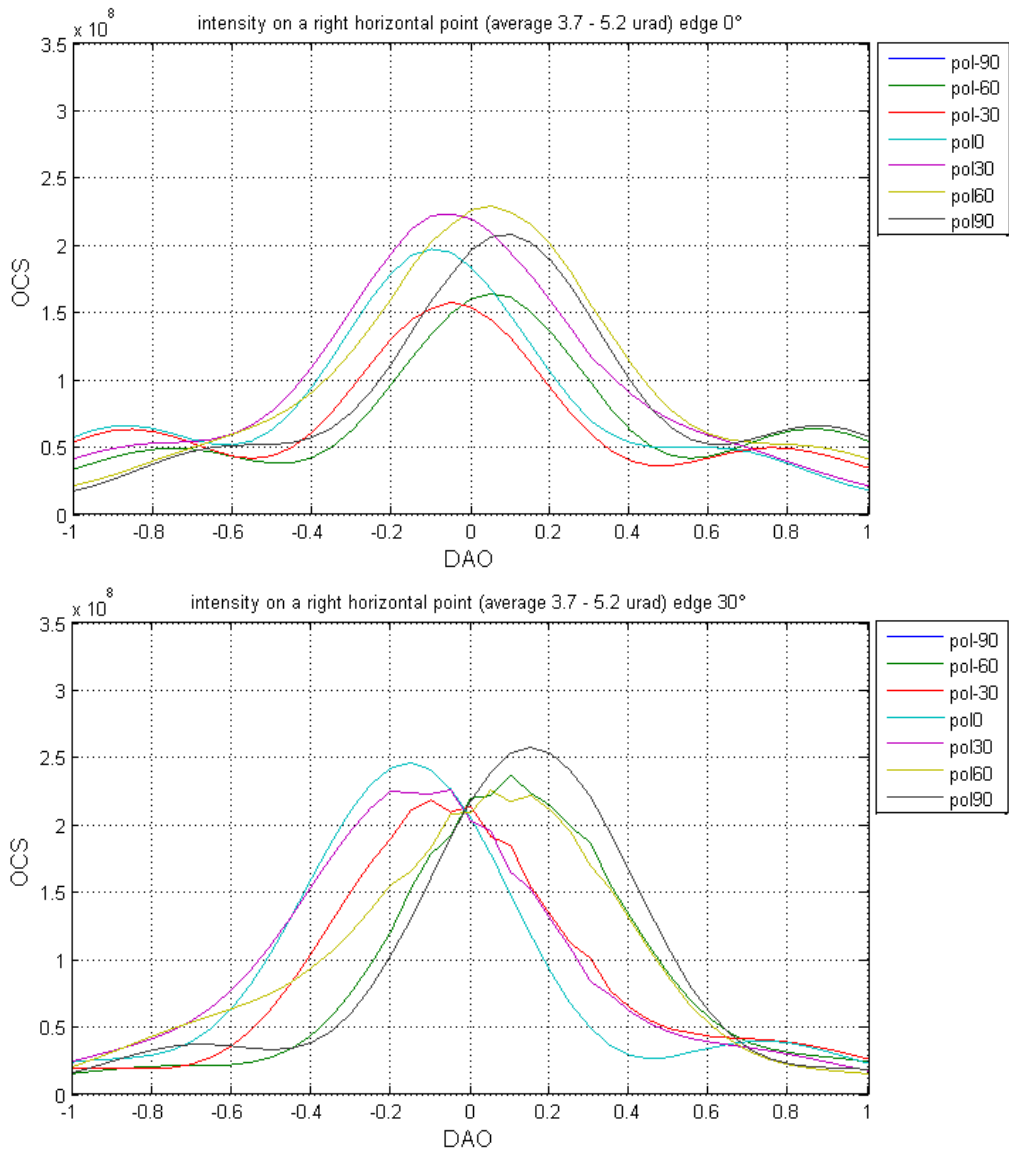**Figure A.3:** Single DAO simulations. CCR orientation 60° to 90° (negative cases are just symmetric).

Figure A.4: Single DAO simulations. CCR orientation 120° (negative cases are just symmetric).

previous plots which did not have a big variation in intensity with respect its average value is chosen. Looking at the plots there are two optimum configurations:

- DAO (0,0,0) arcsec, orientation 90°

- DAO (0.6,0,0) arcsec, orientation 0°

The retroreflector used during the test has a DAO of: 0,0,0 arcsec.

Figure A.5: Double DAO simulations. CCR orientation 0° and 30° (negative cases are just symmetric).
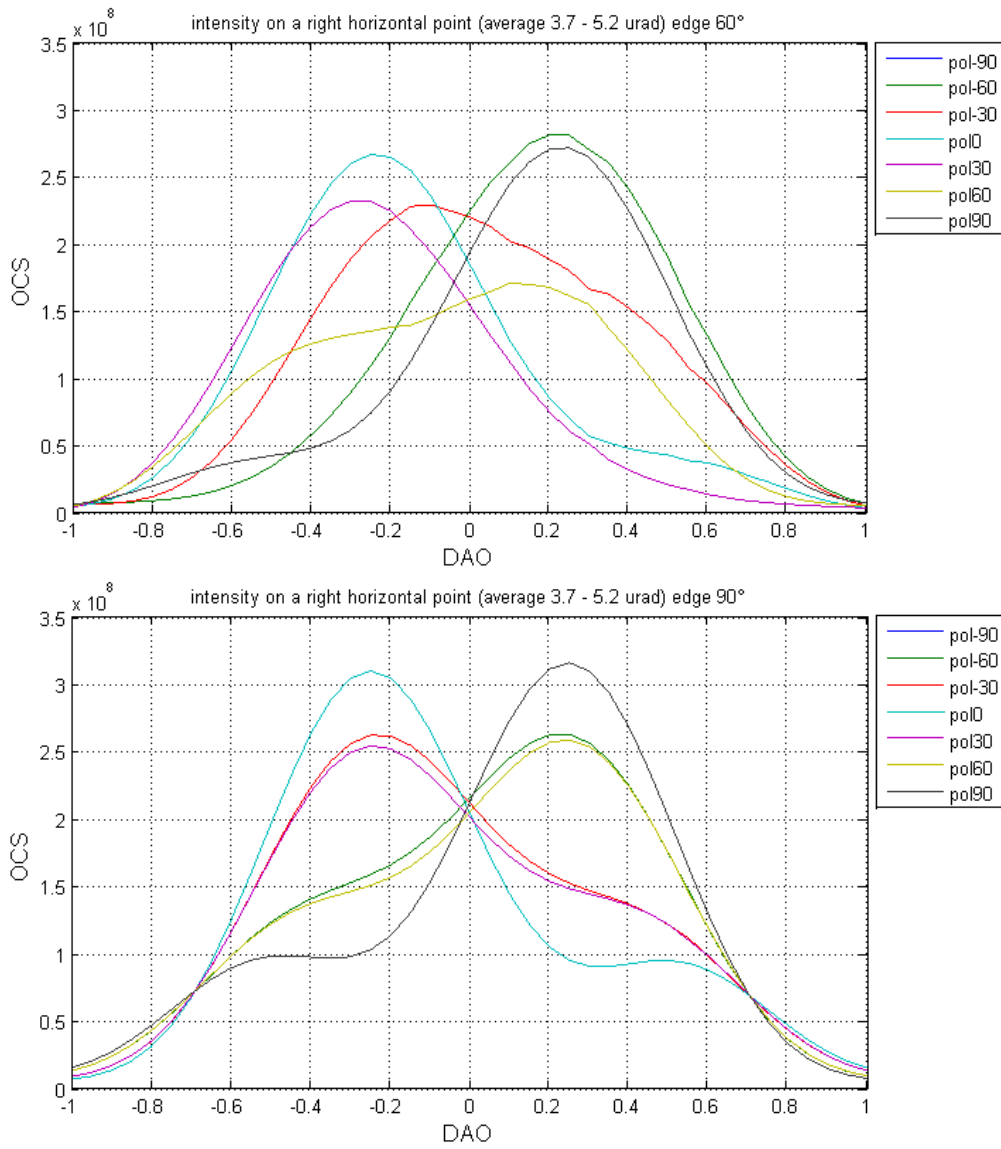
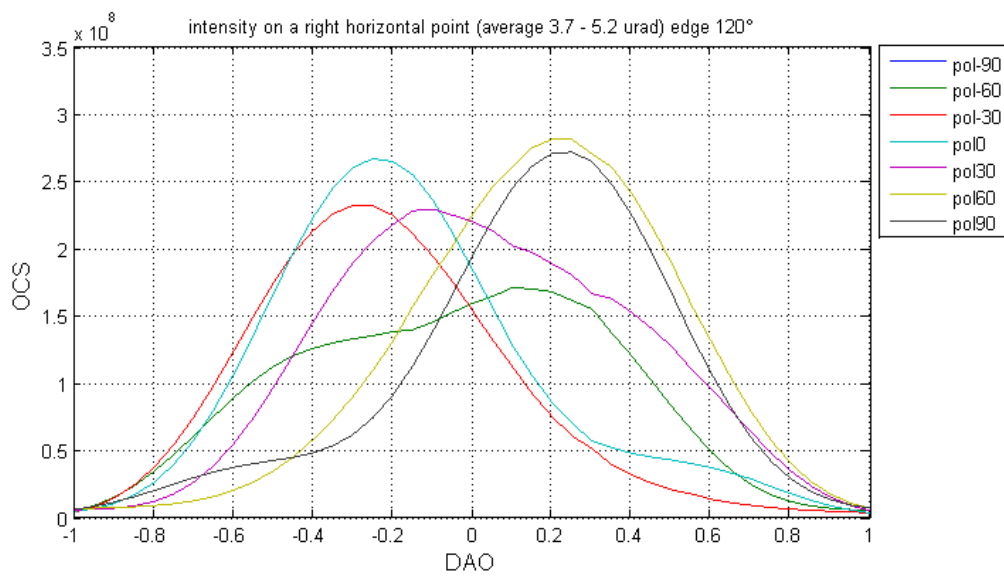**Figure A.6:** Double DAO simulations. CCR orientation 60° to 90° (negative cases are just symmetric).

Figure A.7: Double DAO simulations. CCR orientation 120° (negative cases are just symmetric).

Appendix B

INRRI Optical Simulations

INRRI CCRs consist in a half inch diameter corner cube made out of Suprasil 1 with DAOs of 0.0 ± 0.5 arcsec. The FFDPs, acquired and analyzed using a green laser confirm that CCRs had the requested DAOs. The SCF_Lab team also decided to use CCRs with metallic coating on the back surfaces in order to increase the geometric field of view of the whole array. In far field conditions, the angular aperture Θ of the first minimum in the Airy FFDP of a round flat mirror (or zero-DAO CCR), is:

$$\Theta = 1.22 \times \frac{\lambda}{D} \tag{B.1}$$

Where λ is the wavelength, and D is the mirror diameter. So in our case $\Theta \sim 50 \mu$rad. In order to choose INRRI optical specifications, some general optics results must be taken into account :

- The longer the wavelength the smaller the dimensions, the wider the angular FFDP spread;

- The FFDP resembles that of a flat mirror;

- Zero DAO was chosen because such a small scatterer gives an Airy peak wide enough to support laser ranging from a wide range of orbiter altitudes.

After testing and analysis the SCF_Lab team notice that the measurements agree with the optical simulations made with the CodeV software by the SCF_Lab. In

particular in this Appendix I report the good agreement with the measured and simulated OCS in the plane of the FFDP angular distribution (figure B.1) and the difference between the measured and simulated OCS intensity averaged over the azimuth in the FFDP plane vs VA (figure B.2).
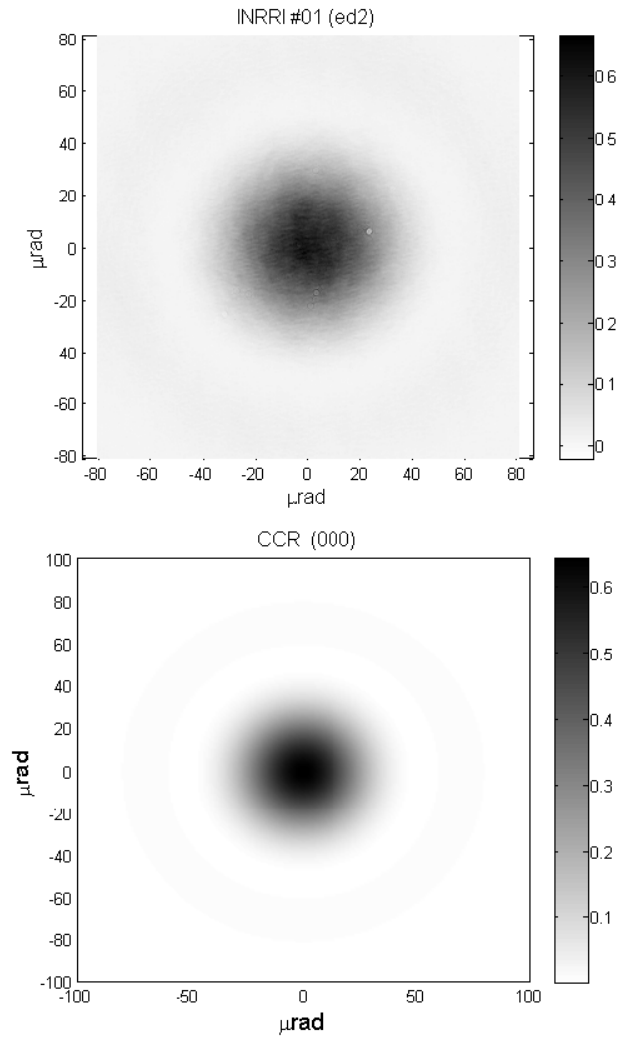

Figure B.1: Top: Measured OCS of an INRRI CCR in the plane of the FFDP angular distribution. Bottom: Simulated OCS of an INRRI CCR in the plane of the FFDP angular distribution. Greyscale is in million square meters.
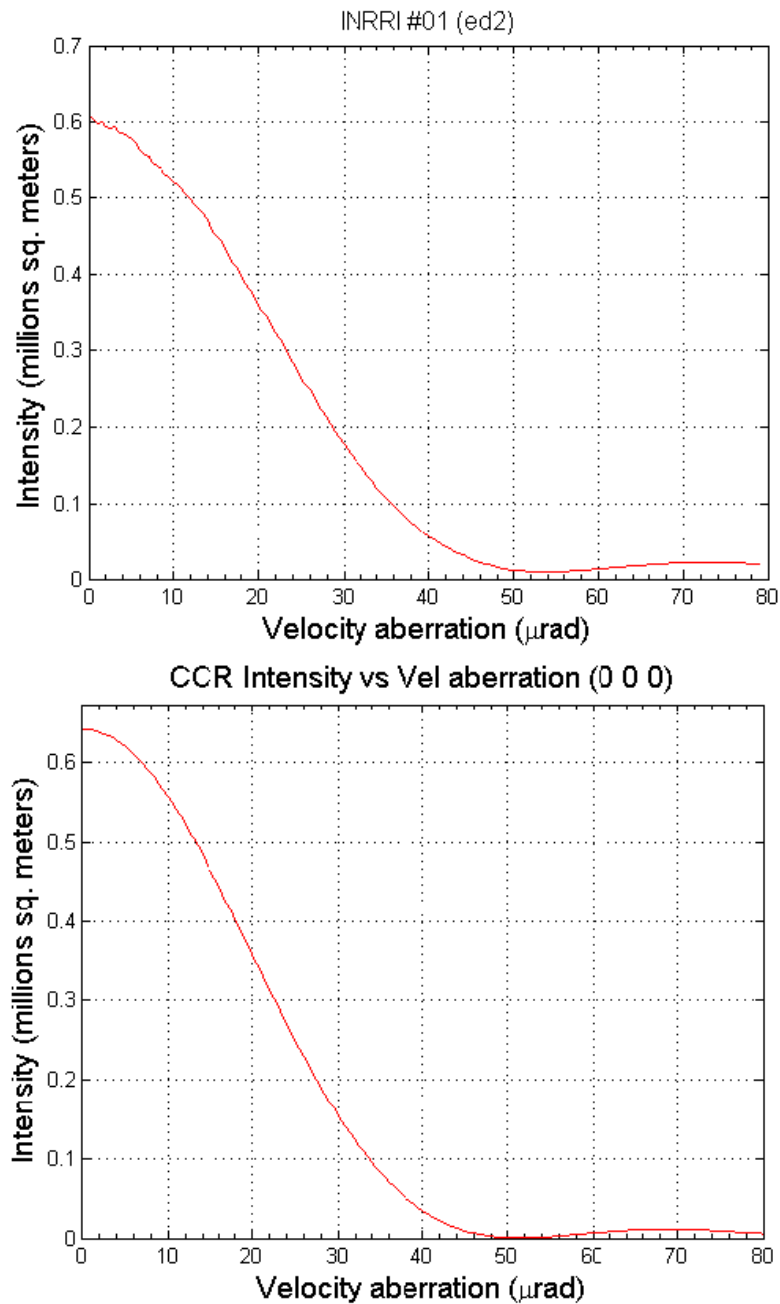
Figure B.2: Top: Measured OCS intensity (averaged over the azimuth in the FFDP plane) vs. VA (radius in the FFDP plane) of an INRRI CCR. Bottom: Simulated OCS intensity (averaged over the azimuth in the FFDP plane) vs. VA (radius in the FFDP plane) of an INRRI CCR.

Appendix C

MoonLIGHT-2 SCF-Tests: Payload PT100 plots

In this appendix section I report the PT-100 temperature probes data that I analyzed for all MoonLIGHT-2 SCF-Tests tests carried out during the three test campaigns (as described in sections 5.1.1, 5.1.2 and 5.1.3). The key elements for the MoonLIGHT-2 are the τ_{CCR} and FFDP analysis, however the probes plots provide additional information in order to better understand the payload structural properties and hence the thermal relationship between CCR and housing. For these reasons, the following plots must be considered as integration to the analysis in Chapter 5.
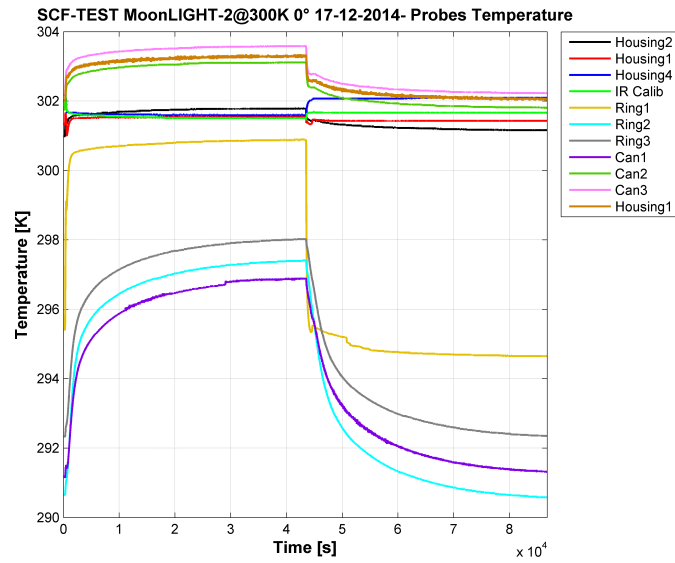
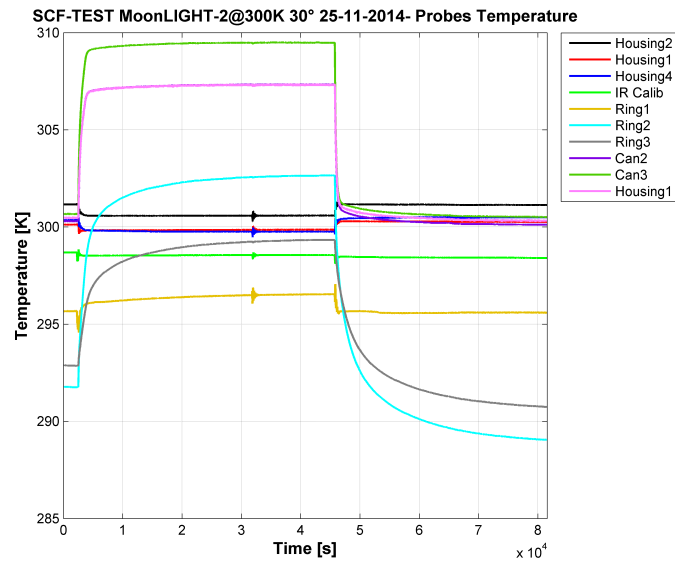**Figure C.1:** MoonLIGHT-2 SCF-Test at 300K, sun incidence 0°, probes temperature result. First test campaign.

Figure C.2: MoonLIGHT-2 SCF-Test at 300K, sun incidence 30°, probes temperature result. First test campaign.
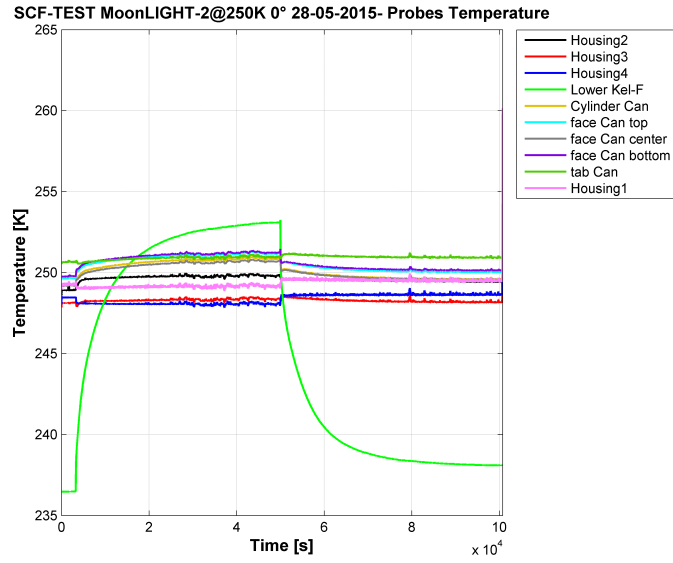
Figure C.3: MoonLIGHT-2 SCF-Test at 250K, sun incidence 0°, probes temperature result. Second test campaign.
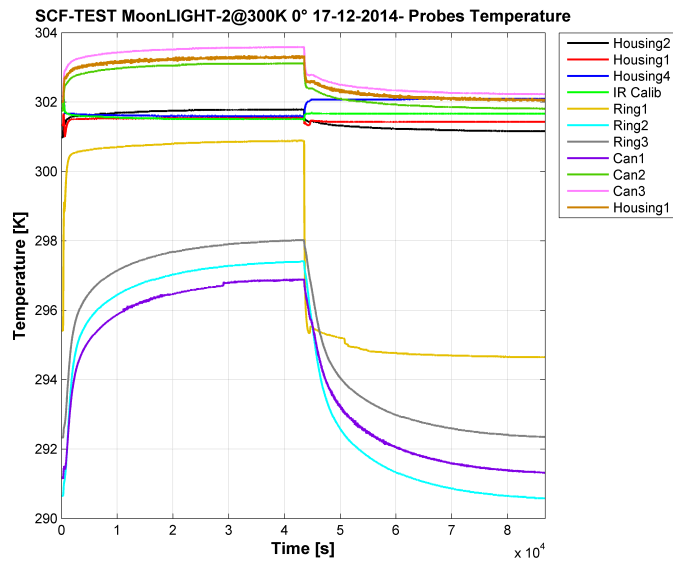

Figure C.4: MoonLIGHT-2 SCF-Test at 300K, sun incidence 0°, probes temperature result. Second test campaign.
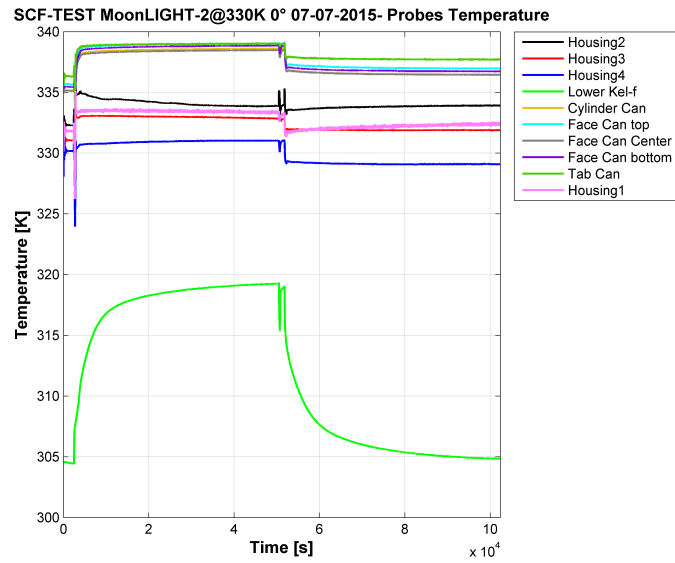
Figure C.5: MoonLIGHT-2 SCF-Test at 330K, sun incidence 0°, probes temperature result. Second test campaign.
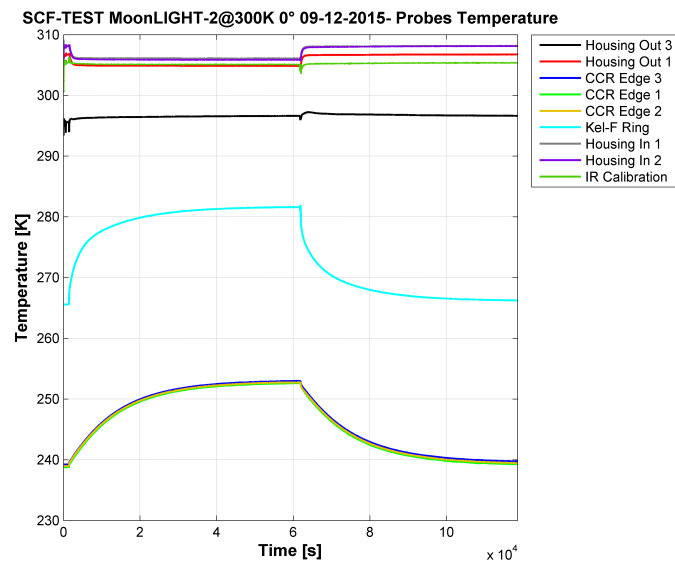

Figure C.6: MoonLIGHT-2 SCF-Test at 300K, sun incidence 0°, probes temperature result. Third test campaign.
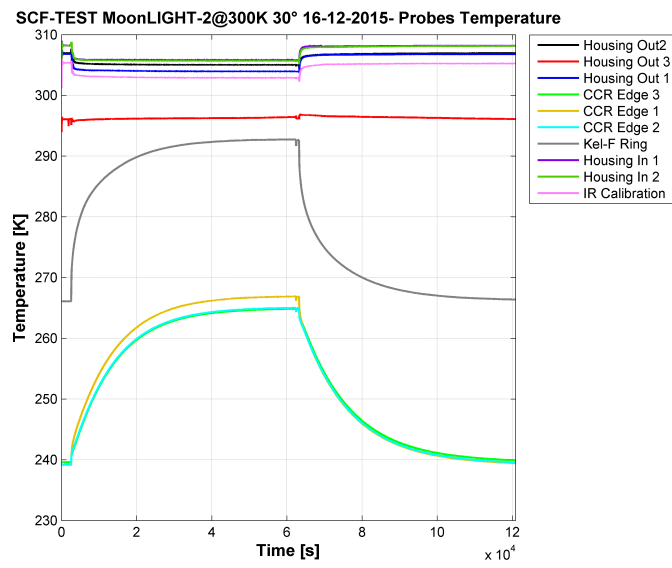
Figure C.7: MoonLIGHT-2 SCF-Test at 300K, sun incidence 30°, probes temperature result. Third test campaign.

Acknowledgement

Vorrei ringraziare:

La mia famiglia, sopratutto mia madre per il supporto e l'ascolto paziente che mi ha sempre dato.

Serena, per l'importanza che ha avuto nella stesura e correzione della tesi e non solo.

I miei amici, e su tutti Stefania e Manuele che mi hanno aiutato a superare i momenti duri di questi anni a lavoro.

Infine vorrei ricordare chi ci ha lasciato.
Mio padre, la cui assenza é stata per me importante negli ultimi sei anni: sono sicuro avrebbe gioito più di tutti di questo risultato.
Giodano, un ragazzo tanto buono quanto sfortunato a cui questo lavoro é dedicato.

Bibliography

[Ash 1965] M.E. Ash, *Generation of Planetary Ephemeris on an electronic computer*, MIT libraries Technical Report 63-391, 2 June 1965.

[Ash 1972] M.E. Ash, *Determination of Earth Satellite Orbits*, MIT libraries Techical Note 1972-5, 19 April 1972.

[Battat 2008] Battat J. B. R., Stubbs C. W., Chandler J. F., *Solar system constraints on the Dvali-Gabadadze-Porrati braneworld theory of gravity*, Phys. Rev. D, 78, 022003, 2008.

[Bender 1973] P.L. Bender *et al.*, *The Lunar Laser Ranging Experiment*, Science, Volume 182, Issue 4109, pp 229-238, 1973

[Boni 2011] Dell'Agnello S., Boni A. *et al.*, *ETRUSCO-2: an ASI-INFN Project of Development and SCF-Test of GNSS Retroreflector Arrays (GRA) for Galileo and the GPS-3* 17th International Workshop on Laser Ranging, Bad Koetzting, Germany, (May 16-20, 2011)

[Cantone 2011] Dell'Agnello S., Cantone C. *et al.*, *SCF-Test of the NASA-GSFC "LAGEOS Sector" and of a Hollow Retroreflector* 17th International Workshop on Laser Ranging, Bad Koetzting, Germany, (May 16-20, 2011)

[Chandler 1985] J.F. Chandler, *A test of General Relativity through the Geodetic Precession of the Moon's orbit*, MIT libraries Technical Report 85-05, 20 december 1985.

[Chandler 1988] J.F. Chandler, *Correcting the predicted chi square for a priori constraints*, MIT libraries Technical Report 88-06, 30 december 1988.

[Chandler 1996] Chandler J. F., Reasenberg R. D., Shapiro I. I., *Proceedings of the 7th Marcel Grossman Meeting on recent developments in theoretical and experimental general relativity, gravitation, and relativistic field theories* edited by Jantzen R. T., Mac Keiser G., Ruffini R. (1996), p. 1501.

[Degnan 1993] J. Degnan *et al.*, *Millimeter Accuracy Satellite Laser Ranging: A Review* Contribution of Space Geodesy to Geodynamics: Technology Geodynamics Series, **25** (1993)

[Dell'Agnello 2010] Dell'Agnello *et al.*, *Next Generation Lunar Laser Ranging and its GNSS Applications*, IEEE Aerospace Conference, Big Sky (MT), USA, March 2010 - Conference Proceeding

[Dell'Agnello 2011] Dell'Agnello S. *et al.*, *Creation of the new industry-standard space test of laser retroreflectors for the GNSS and LAGEOS* Adv. in Space Research, Vol.47, 822-842 (2011)

[Dell'Agnello 2017] S. Dell'Agnello *et al.*, *INRRI-EDM/2016: the first laser retroreflector on the surface of Mars*, Advance in Space Research, Vol.59, 645-655 (2017)

[Efron 1982] B. Efron, *The Jackknife, the Bootstrap, and Other Resampling Plans*, Society of Industrial and Applied Mathematics CBMS-NSF Monographs 38, 1982.

[Filippi 1999] Filippi E. *et al.*, *Pyroshock Simulation using the Alcatel ETCA Test Facility* European Conference on Launch Vehicle Vibrations 1999

[Folkner 2014] W. M. Folkner *et al.*, *The Planetary and Lunar Ephemerides DE430 and DE431*, IPN Progress Report 42-196, February 15, 2014.

[Johnson 2001] R. W. Johnson, *An Introduction to the Bootstrap*, Teaching Statistics. Volume 23, Number 2, Summer 2001.

[Lops 2011] *Probing Gravitational Physics with Lunar Laser Ranging* Chapter in the book Nova publisher ISBN: 978-3-319-20223-5, pp. 495-538 (2011)

[March 2011] March R. *et al.*, *Constraining spacetime torsion with the Moon and Mercury*, Phys. Rev. Letter D83, 104008, 2011

[March 2013] Bertolami O., March R., Páramos J., *Solar System constraints to non-minimally coupled gravity*, Phys. Rev. D, 88, 064019, 2013.

[Martini 2012] Martini M. *et al.*, *MoonLIGHT: A USA-Italy lunar laser ranging retroreflector array for the 21st century* Planetary and Space Science 74 (2012) 276-282

[Martini 2016] *Probing Gravity with Next Generation Lunar Laser Ranging* Chapter in the book Gravity: Where Do We Stand, ISBN: 978-3-319-20224-2, 195-210 (2016)

[Merkowitz 2009] Merkowitz S. *et al.*, *The Moon as a Test Body for General Relativity* A white paper to the planetary science decadal survey, 2009

[Murphy 2003] Murphy T. *et al.*, *Testing Gravity via Next Generation Lunar Laser-Ranging* Nuclear Physics B Proceedings Supplements, 134, 155.

[Murphy 2010] T. Murphy *et al.*, *Long-term degradation of optical devices on the Moon* Icarus, **208**, 31-35 (2010)

[Murphy 2012] , *APOLLO: millimeter lunar laser ranging* Classical Quantum Gravity, **29** (2012)

[Nordtvedt 1995] Nordtvedt K., *The Relativistic Orbit Observables in Lunar Laser Ranging* Icarus, **114**, 51-62 (1995)

[Nordtvedt 2003] Nordtvedt K., *Testing the Equivalence Principle with laser ranging to the Moon* Advances in Space Research, Vol. 32, 1311 (2003).

[Rambaux 2008] Rambaux N., Williams J.G., Boggs D.H., *A dinamically Active Moon-Lunar Free Librations and Excitation Mechanism*, 39th Lunar and Planetary Science Conference, March 10-14, 2008.

[Reasenberg 1975] R.D. Reasenberg, *The PEP A Priori facility*, MIT libraries Technical Report 54-612, 28 July 1975.

[Reasenberg 1979] Reasenberg R. D. *et al.*, *Viking Relativity Experiment: Verification of signal retardation by solar gravity*, Astrophysical. Journal Letters 234, L219 (1979).

[Reasenberg 1980] R.D. Reasenberg, *The RMS predicted residual calculated in the analyze link of PEP*, MIT libraries Technical Report 80-01, 18 Januaryl 1980.

[Reasenberg 1987] R.D. Reasenberg, *De Sitter Precession of Earth-Moon Gyroscope*, MIT libraries Technical Report 87-03, 09 April 1987.

[Reasenberg 2016] R.D. Reasenberg, *et al.*, *Modelling and Analysis of the APOLLO Lunar Laser Ranging dat*a arXiv: 1608.04758v1(2016)

[Shapiro 1964] I. Shapiro, *Fourth Test of General Relativity* Phys. Rev. Lett. 13, 789 (1964)

[Shapiro 1988] Shapiro I., Reasenberg R. D., Chandler J. F., *Measurement of the de Sitter Precession of the Moon: A Relativistic Three-Body Effect*, Phys. Rev. Lett. 61, 2643-2646 (1988).

[Slade 1971] M.A. Slade, *The Orbit of the Moon*, Partial fulfillment of the requirements for the degree of Doctor of Philosophy, September 1971.

[Tausner 1966] M.J. Tausner, *General Relativity and its effect on planetary orbits and interplanetary observation*, MIT libraries Techical Report 425, 07 October 1966.

[Williams 2004] Williams J.G., Turyshev S.G., Boggs D.H., *Progress in Lunar Laser Ranging Tests of Relativistic Gravity*, Phys. Rev. Lett. 93, 261101 (2004).

[Williams 2008] Williams J.G., Boggs D.H., Ratcliff J.T. *Lunar Tides, Fluid Core and Core/Mantle Boundary* 39th Lunar and Planetary Science Conference, March 10-14, 2008.

[Williams 2009a] Williams J.G., Boggs D.H., Ratcliff J.T., *A larger Lunar Core?* 2009a, 40th Lunar and Planetary Science Conference, March 23-27, 2009.

[Williams 2009b] Williams J.G., Turyshev S.G., Boggs D.H., *Lunar Laser Ranging Test of the Equivalence Principle with the Earth and Moon*, Int. J. Mod. Phys. D, Volume 18, 1129-1175, 2009b.